國立臺灣大學工學院暨醫學院醫學工程研究所

博士論文

Institute of Biomedical Engineering
College of Engineering and College of Medicine
National Taiwan University

Doctoral Dissertation

用於癌症治療與診斷的多功能奈米粒子

Multifunctional Nanoparticles for Cancer Theranostics

梁博欽

Po-Chin Liang

指導教授：林文澧 博士

Advisor: Win-Li Lin, Ph.D.

中華民國 108 年 7 月

July 2019

doi:10.6342/NTU201902917

國立臺灣大學（碩）博士學位論文
口試委員會審定書

論文中文題目:用於癌症治療與診斷的多功能奈米粒子
論文英文題目: Multifunctional Nanoparticles for Cancer Theranostics

本論文係梁博欽君（學號 D00583003）在國立臺灣大學工學院暨醫學院醫學工程研究所、所完成之博士學位論文，於民國 108 年 7 月 23 日承下列考試委員審查通過及口試及格，特此證明

口試委員：

（指導教授）林 [illegible]（簽名）

[illegible]

王 [illegible] 謝銘鈞

李 [illegible] [illegible]

系主任、所長 黃義侑（簽名）

doi:10.6342/NTU201902917

摘要

癌症是台灣最常見的死因，根據台灣衛生福利部公布的資料，2017 年癌症奪走 4 萬 8037 條人命，再創歷史新高，蟬聯 36 年十大死因之首。化學治療是治療癌症的主要方法之一，然而傳統的化療藥物在體內非特定地分佈，它們同時影響癌症和健康細胞，導致劑量相關的副作用和到達腫瘤的藥物濃度不足。多功能奈米粒子能靶向和控制向腫瘤細胞釋放化療藥劑，從而減少藥物誘發的全身性副作用，並提高局部腫瘤治療效果。

在我們的第一項研究中，我們開發了多功能磁性奈米顆粒 SPIO-PEG-D，它是由超順磁性氧化鐵 (SPIO) 磁性核心和親水性聚乙烯乙二醇 (PEG) 外殼組成，之後再鍵結 Doxorubicin (Dox) 而形成 SPIO-PEG-D，它同時具有腫瘤磁振成像(MRI)和腫瘤化學治療的功用。SPIO 奈米粒子的大小大約 10nm，可以由穿透式電子顯微鏡觀察。而由振動樣品磁力計生成的遲滯曲線，可以發現 SPIO-PEG-D 仍具有超順磁性，其磁性與 SPIO-PEG 沒有顯著差別，表示不會因為鍵結 Doxorubicin 而影響其磁性。SPIO-PEG-D 的橫向鬆弛度 (r2) 明顯高於縱向鬆弛度 (r1) (r2/r1 = 9)，因此我們可以由磁振 T2 加權影像來觀察 SPIO-PEG-D 的分佈。經由將 Doxorubicin 結合在 SPIO-PEG 的表面，因為 PEG 的隱藏效應，可以減少 Doxorubicin 的降解，因此延長了 Doxorubicin 在血液循環中的半衰期。在體外實驗中發現，SPIO-PEG-D 可導致 HT-29 癌細胞 DNA 交聯更嚴重，使其 DNA 表現降低，細胞凋亡升高。在普魯士藍染色研究中發現,在外加磁場中用 SPIO-PEG-D 治療的腫瘤，其腫瘤內鐵密度遠遠高於單獨使用 SPIO-PEG-D 治療的腫瘤。在體內 MRI 研究中發現，有外加磁場用 SPIO-PEG-D 治療的腫瘤，其 T2 加權信號比沒有外加磁場單獨使用 SPIO-PEG-D 治療的腫瘤更強，顯示外加磁場可以吸引更多 SPIO-PEG-D 累積在腫瘤組織中。在 SPIO-PEG-D 的抗癌效率研究中顯示，有外加磁場組比沒有外加磁場組的腫瘤明顯縮小。在體內實驗中還發現，SPIO-PEG-D 這種藥物輸送系統結合局部外加磁場可以減少心毒性和肝毒性的副作用。我們的第一項研究結果顯示,我們研製的多功能磁性奈米顆粒 SPIO-PEG-D，在 MRI 監測及外加磁場增強腫瘤化療效果具有相當大的潛力。

在我們的第二項研究中，我們開發了多功能磁性奈米凝膠顆粒 iMNP-D ，它是由 iRGD 鍵結溫度/pH 雙敏感的磁性奈米凝膠顆粒(MNP-D)，而此凝膠顆粒中裝

doi:10.6342/NTU201902917

有超順磁性氧化鐵奈米顆粒和 Doxorubicin。溫度/pH 雙敏感聚合物(丙烯酸-共聚(乙二醇)二丙烯醯胺-共聚-N-異丙烯醯胺(Poly(AA-CO-PEGDA-CO-NIPAM))奈米凝膠，是通過自由基聚合而成。正電荷的 Doxorubicin ，在 pH7.4 的環境下，經由靜電相互作用，而引入帶負電荷的奈米凝膠中。SPION 和 Doxorubicin 均封裝在奈米凝膠中，以合成溫度/pH 雙敏感磁性奈米凝膠顆粒 (MNP-D)，然後將 iRGD 結合在 MNP-D 表面形成 iMNP-D，iMNP-D 因為與 iRGD 結合，因而提高其腫瘤靶向和穿透效率。因為 iRGD 可以與腫瘤的 intergrin 與 neuropilin-1 的受體結合，而被內化進入腫瘤細胞。另外由於 iMNP-D 具有溫度/pH 雙敏感特性，所以可以利用周圍環境溫度/pH 值的變化，來改變其大小和親水/疏水性，從而控制藥物釋放。Doxorubicin 在酸性及高溫的環境下容易從 iMNP-D 中釋放出來。而腫瘤的酸性環境正好有利於 Doxorubicin 的釋放。另外，我們可以利用短時間的局部高溫，來啟動 Doxorubicin 從 iMNP-D 中釋放出來。我們對 iMNP-D 進行了增強 HT-29 結腸癌化療和 MR 成像的評估。體外和體內研究證明 iRGD 的存在提高了 Doxorubicin 對結腸癌細胞/腫瘤的細胞毒性效率,並顯示 iMNP-D 可以專門將 Doxorubicin 輸送到結腸癌。此外經由短時間局部高熱來控制藥物釋放因而促進抗腫瘤療效。

總體實驗結果顯示，這種高腫瘤穿透性，高癌細胞靶向的 iMNP-D，是結腸癌的高潛力診斷與治療兼具的多功能磁性奈米凝膠載體。

關鍵詞: 癌症，化療，阿黴素，內化精胺酸-甘胺酸-天門冬胺酸, 磁體增強，磁振造影成像，磁振造影監測，奈米凝膠，聚乙烯乙二醇，超順磁性氧化鐵，溫度/酸鹼 敏感，腫瘤

doi:10.6342/NTU201902917

Abstract

Cancer is the most common cause of death in Taiwan, with 48,037 people killed in 2017, a record high and the top 10 causes of death in 36 years, according to data released by Taiwan's Ministry of Health and Welfare. Chemotherapy is one of the main ways to treat cancer, while conventional cancer chemotherapeutic drugs are distributed nonspecifically in the body and hence they affect both cancerous and healthy cells, resulting in dose-related side effects and inadequate drug concentrations reaching the tumor. Multifunctional nanoparticles can target and control releasing chemotherapy agent to tumor cells, thus it can reduce drug induced systemic side effects and improve local tumor treatment results.

In the first study, we developed multifunctional magnetic nanoparticle superparamagnetic iron oxide – polyethylene glycol- Doxorubicin (SPIO-PEG-D), consisting of a superparamagnetic iron oxide (SPIO) magnetic core and a shell of aqueous stable polyethylene glycol (PEG) conjugated with doxorubicin (Dox), for tumor magnetic resonance imaging (MRI) and chemotherapy. The size of SPIO nanoparticles was ~10 nm, which was visualized by transmission electron microscope (TEM). The hysteresis curve, generated with vibrating-sample magnetometer, showed that SPIO-PEG-D was superparamagnetic with an insignificant difference as compared to superparamagnetic iron oxide – polyethylene glycol (SPIO-PEG). The transverse relaxivity (r_2) for SPIO-PEG-D was significantly higher than the longitudinal relaxivity (r_1) ($r_2/r_1 = 9$), so we can observe the distribution of SPIO-PEG-D by MRI T2WI. The half-life of Dox in blood circulation was prolonged by conjugating Dox on the surface of SPIO with PEG to reduce its degradation, by stealth shielding effect of PEG. The in vitro experiment showed that SPIO-PEG-D could cause DNA crosslink more serious,

doi:10.6342/NTU201902917

resulting in a lower DNA expression and a higher cell apoptosis for HT-29 cancer cells. The Prussian blue staining study showed that the tumors treated with SPIO-PEG-D under a magnetic field had a much higher intratumoral iron density than the tumors treated with SPIO-PEG-D alone. The in vivo MRI study showed that the T_2-weighted signal was stronger for the group under a magnetic field, indicating that it had a better accumulation of SPIO-PEG-D in tumor tissues. In the anticancer efficiency study for SPIO-PEG-D, the results showed that there was a significantly smaller tumor size for the group with a magnetic field than the group without. The in vivo experiments also showed that this drug delivery system SPIO-PEG-D combined with a local magnetic field could reduce the side effects of cardiotoxicity and hepatotoxicity. The results showed that our developed multifunctional magnetic nanoparticle SPIO-PEG-D owns a great potential for MRI-monitoring and magnet-enhancing tumor chemotherapy.

In the second study, we developed multifunctional magnetic nanogel particle iMNP-D (iRGD-conjugated magnetic nanogel particles – Doxorubicin) , which was made of iRGD (internalized Arginine–glycine–aspartic acid) conjugated temperature/pH dually sensitive magnetic nanogel particles (MNP-D), which was loaded with superparamagnetic iron oxide nanoparticles and doxorubicin. Temperature/pH dually sensitive poly(acrylic aicd-co-poly (ethylene glycol) di-acrylamide-co-N-isopropylacrylamide (poly(AA-co-PEGDA-co-NIPAM)) nanogels were synthesized by free radical polymerization. Positively charged Dox was introduced into the negatively charged nanogels by electrostatic interaction at pH 7.4. Both Superparamagnetic iron oxide nanoparticles (SPIONs) and Dox were encapsulated in nanogels to develop temperature/pH dually sensitive magnetic nanogel particles (MNP-D), followed by conjugating the peptide iRGD on the MNP-D surface to form iMNP-D, and iMNP-D could enhance its tumor targeting and penetrating efficiency by

doi:10.6342/NTU201902917

the conjugation of iRGD. Because iRGD could be internalized into tumor cells by intergrin and neuropilin-1 receptor. Besides, the iMNP-D maintains temperature/pH dually sensitive properties and it can change its size and hydrophilic/hydrophobic properties by changing environment temperature/pH, thus achieving controlled drug release. Dox could be released from iMNP-D at a low pH and/or a high temperature. And the acid environment of tumor could trigger the release of Dox from iMNP-D. In addition, we can apply short-time local hyperthermia to trigger Dox releasing from iMNP-D. We evaluated iMNP-D for both enhancing HT-29 colon cancer chemotherapy and MR imaging. In-vitro and in-vivo studies proved that the presence of iRGD enhanced the cytotoxic efficiency of Dox to colon cancer cells/tumors and indicated that iMNP-D can deliver Dox specifically to colon cancer and can control drug release with a short-time local hyperthermia to promote anti-tumor efficacy.

The overall experimental results indicate that this high tumor-penetrating, high cancer cell-targeting iMNP-D is a highly potential theranostic multifunctional magnetic nanogel carrier for the monitoring and treatment of colon cancer.

Keywords: cancer, chemotherapy, Doxorubicin(Dox), iRGD, magnet enhancing, MR imaging, MRI monitoring, nanogel, polyethylene glycol, superparamagnetic iron oxide, temperature/pH sensitive, tumor

doi:10.6342/NTU201902917

Abbreviation and Acronyms

Abbreviation	Full Form
AA	Acrylic acid
Dh	hydrodynamic diameter
DLS	Dynamic light scattering
Dox	Doxorubicin
EE	encapsulation efficiencies
EPR	enhanced permeability and retention
FD	Free Doxorubicin
FITC	Fluorescein isothiocyanate
FT-IR	Fourier-transform infrared spectroscopy
HPLC	high performance liquid chromatography
IC50	half maximal inhibitory concentration
ICP-MS	Inductively coupled plasma mass spectrometer
iMNP	iRGD magnetic nanogel particles
iMNP-D	iRGD magnetic nanogel particles Doxorubicin
IO	Iron oxide
iRGD	internalized Arginine–glycine–aspartic acid
LCST	lower critical solution temperature
MF	Magnetic field
MNP	magnetic nanogel particles
MNP-D	magnetic nanogel particles-Doxorubicin
MRI	Magnetic resonance imaging
MRS	Magnetic resonance spectrography
MTT assay	(3-(4,5-Dimethylthiazol-2-yl)-2,5-diphenyltetrazolium bromide) assay
NIPAM	N-Isopropyl acrylamide
NIR	Near Infrared
NMR	Nuclear Magnetic Resonance
NPs	Nanoparticles
OA	Oleic acid
PBS	Phosphate-buffered saline
PEG	Polyethylene glycol
PEGDA	Polyethylene glycol Di-Acrylamide
RES	reticuloendothelial system
RFA	Radiofrequency ablation
RGD	Arginine–glycine–aspartic acid
RME	receptor-mediated endocytosis
SPIO	Superparamagnetic iron oxide
SPIO NPs	Superparamagnetic iron oxide nanoparticles
SPIONs	Superparamagnetic iron nanoparticles
SPIO-PEG	Superparamagnetic iron oxide-Polyethylene glycol
SPIO-PEG-D	Superparamagnetic iron oxide-Polyethylene glycol-Doxorubicin
TEM	Transmission electron microscope
TGA	thermogravimetric analysis
TUNEL assay	Terminal deoxynucleotidyl transferase transferase dUTP nick end labeling assay
VSM	vibrating sample magnetometer
XRD	X-ray diffraction

doi:10.6342/NTU201902917

Contents

中文摘要 vii

Abstract.....vii

Abbreviation and Acronyms ……..vi

Contents.....viii

List of Figures.....viii

List of Tables xviii

Chapter 1. Background & Objectives.....1

1.1. Unmet need of cancer chemotherapy.....1

1.2. Cancer nanomedicine 1

1.3. Targeting drug delivery systems of nanomedicine 1

1.3.1. Passive targeting drug delivery system.....2

1.3.2. Active targeting drug delivery system 2

1.4. Magnetic-targeted nanoparticles.....3

1.5. Control releasing (pH/temperature dually responsive systems) 4

1.6. Multifunctional nanoparticles for targeted imaging and therapy.....5

1.7. Objectives 5

Chapter 2. (My study Part I) Doxorubicin-eluting magnetic nanoparticles as a drug delivery system for magnetic resonance imaging-monitoring magnet-enhancing tumor chemotherapy 9

2.1. Introduction 9

2.2. Methods and materials.....12

2.2.1. Materials.....12

doi:10.6342/NTU201902917

2.2.2. Synthesis of HOOC-PEG-triethoxysilane (HOOC-PEG silane) 12
2.2.3. Synthesis of magnetite nanoparticles with IO 13
2.2.4. Synthesis of SPIO-PEG 13
2.2.5. Synthesis of SPIO-PEG-D 14
2.2.6. Analysis of particle properties 14
2.2.7. MRI analysis of nanoparticles in cancer cells 15
2.2.8. Qualitative and quantitative studies of cellular uptake 16
2.2.9. Degradation test for free Dox and SPIO-PEG-D 17
2.2.10. DNA interstrand crosslink 17
2.2.11. Cell MTT cytotoxicity 17
2.2.12. In vivo MR image and detection of iron 18
2.2.13. In vivo antitumor activity 19
2.2.14. Apoptosis detection for tumor cells 20
2.3. Results and discussion 20
2.3.1. Synthesis of HOOC-PEG-triethoxysilane (HOOC-PEG silane) and thermal properties of nanoparticles 20
2.3.2. Characterization of nanoparticles 20
2.3.3. Qualification and quantification of SPIO-PEG-D 21
2.3.4. Structural analysis and magnetic properties of SPIO-PEG and SPIO-PEG-D 22
2.3.5. Relaxivity 22
2.3.6. In vitro qualitative and quantitative studies of cellular uptake 23
2.3.7. In vitro degradation and anticancer cell efficiency test 24
2.3.8. In vivo MR imaging and detection of iron 25
2.3.9. In vivo antitumor study 26

doi:10.6342/NTU201902917

2.4. Conclusion 28

Chapter 3. (My study Part II) Temperature/pH sensitive magnetic nanogel particles loaded with doxorubicin and conjugated with iRGD for enhancing colon cancer tumor chemotherapy and MR imaging 43

3.1. Introduction 43

3.2. Methods and materials 45

3.2.1. Materials 45

3.2.2. Preparation of poly (ethylene glycol) di-acrylamide (PEGDA) 46

3.2.3. Synthesis of magnetite nanoparticles with oleic acid (IO-OA) 46

3.2.4. Synthesis of magnetite nanoparticles with citric acid (IO-CA) 47

3.2.5. Synthesis of magnetic nanogel particles (MNP) and iRGD-conjugated MNP (iMNP), and loaded with doxorubicin (MNP-D or iMNP-D) ... 47

3.2.6. Characterizations of MNP-D and iMNP-D 48

3.2.7. In vitro drug release 49

3.2.8. MRI analysis of cellular internalization of MNP-D, iMNP-D, and i+iMNP-D 49

3.2.9. Qualitative and quantitative studies of cellular uptake 50

3.2.10. Cell MTT cytotoxicity 51

3.2.11. In vivo MR image and detection of iron 51

3.2.12. In vivo antitumor activity 52

3.2.13. In vivo Dox accumulation 53

3.2.14. Apoptosis detection for tumor cells 54

3.3. Results and discussion 54

3.3.1. Characterization of poly(ethylene glycol) di-acrylamide and conjugation ratio of iRGD 54

doi:10.6342/NTU201902917

3.3.2. Characterization of MNP-D and iMNP-D 54

3.3.3. In vitro Dox release 56

3.3.4. In vitro qualitative and quantitative studies of cellular uptake 57

3.3.5. In vitro cytotoxicity of MNP-D and iMNP-D against HT-29 cancer cells 58

3.3.6. In vivo MR imaging and detection of iron 59

3.3.7. In vivo antitumor activity 60

3.3.8. Dox accumulation analysis for tumors 61

3.3.9. Apoptosis detection for tumor cells 62

3.4. Conclusion 62

Chapter 4. Summary and future work 78

Acknowledgement 82

References 83

doi:10.6342/NTU201902917

List of Figures

Figure 1-1. Passive targeting drug delivery system was achieved by tumor vascular endothelial gap and impaired lymphatic drainage of tumor tissue, thus enhanced permeability of nanoparticle from endothelial gap into tumor tissue, and enhanced retention in tumor tissue, so called enhanced permeability and retention (EPR) effect. Active targeting drug delivery system with targeting ligand on the nanoparticle surface, to bind a tumor-associated receptor and facilitate the delivery of nanoparticles to the intracellular site by receptor-mediated endocytosis (RME), enabling a greater antitumor efficacy……..6

Figure 1-2. Magnetic-Targeted drug delivery systems are magnetic nanoparticles that carry anticancer drug to the target tumor tissue by using an external magnet, which can keep larger amount of anticancer drug at tumor site for longer time, and prevent normal tissue from side effects of chemotherapy…… …….7

Figure 1-3. Multifunctional nanoparticles surface modifications with tumor-associated targeting ligand may increases the binding affinity toward tumor cells by receptor-mediated endocytosis. Multifunctional nanoparticles with pH/thermosensitive moieties, can control releasing anticancer drug in tumor cells, thus improving local tumor treatment effect and reducing drug induced systemic side effects. Multifunctional nanoparticles with SPIO as imaging probe, may use MRI as a diagnostic tool, and make theranostics possible…….8

Figure 2-1. SPIO nanoparticles conjugated with PEG and then doxorubicin under a magnetic field during tumor treatment. Abbreviation: SPIO,

doi:10.6342/NTU201902917

superparamagnetic iron oxide; PEG, polyethylene glycol; SPIO-PEG-D, SPIO with PEG conjugated with doxorubicin. 30

Figure 2-2. Synthetic route for HOOC-PEG silane. Abbreviation: PEG, polyethylene glycol. 31

Figure 2-3. Synthetic route for SPIO-PEG-D. Abbreviation: PEG, polyethylene glycol; IO, oleic acid; PEG-SPION, PEG containing superparamagnetic iron oxide nanoparticle; SPIO-PEG-D, SPIO with PEG conjugated with doxorubicin; NHS, N-hydroxysulfosuccinimide; EDC, 1-ethyl-3-(3-(dimethylamino)-propyl) carbodiimide; Dox, doxorubicin. 32

Figure 2-4. (A) 1H NMR spectra for HOOC-PEG silane. (B) TGA curves of the SPIO-PEG were tested twice. Abbreviation: PEG, polyethylene glycol; TGA, thermogravimetric analysis; SPIO-PEG, superparamagnetic iron oxide with PEG. 33

Figure 2-5. Particle size distribution and TEM images for (A and C) SPIO-PEG and (B and D) SPIO-PEG-D. (E) Stability curves of SPIO-PEG-D over 12 months (mean ± SD) (n=3). Abbreviation: TEM, transmission electron microscope; SPIO-PEG, superparamagnetic iron oxide with polyethylene glycol; SPIO-PEG-D, SPIO with PEG conjugated with doxorubicin; SD, standard deviation. 34

Figure 2-6. (A) FT-IR spectra for SPIO-PEG-D, Dox, and SPIO-PEG. (B) Quantity of Dox conjugate with SPIO-PEG. Abbreviation: FT-IR, Fourier transform infrared; SPIO-PEG-D, superparamagnetic iron oxide with polyethylene glycol conjugated with doxorubicin; Dox, doxorubicin; SPIO-PEG, SPIO with PEG; FD, free doxorubicin. 35

Figure 2-7. (A) X-ray powder diffraction pattern for SPIO-PEG-D, (B) variation of

doi:10.6342/NTU201902917

magnetization for SPIO-PEG, and (C) for SPIO-PEG-D as a function of applied magnetic field. Abbreviation: SPIO-PEG-D, superparamagnetic iron oxide with polyethylene glycol conjugated with doxorubicin; SPIO-PEG, SPIO with PEG. 36

Figure 2-8. Relaxation response for (A and C) SPIO-PEG-D and (B and D) SPIO-PEG. Abbreviation: SPIO-PEG-D, superparamagnetic iron oxide with polyethylene glycol conjugated with doxorubicin; SPIO-PEG, SPIO with PEG. 37

Figure 2-9. Cellular uptake of SPIO-PEG-D with or without magnetic field. Note: (A) T2-weighted MR phantom images of HT-29 cells after incubation with SPIO-PEG-D or SPIO-PEG-D/MF for 3, 6, or 24 hours and (B) Prussian blue staining images of HT-29 cells after 24-hour treatment with SPIO-PEG-D and SPIO-PEG/MF. (C) The iron uptake in HT-29 cells treated with 100 μg Fe/mL of SPION-PEG-D after treatment with SPIO-PEG-D and SPIO-PEG/MF at different incubation time (mean ± SD) (n=5). **P<0.01. Abbreviation: MR, magnetic resonance; SPIO-PEG-D, superparamagnetic iron oxide with polyethylene glycol conjugated with doxorubicin; SPIO-PEG-D/MF, SPIO-PEG-D under magnetic field; SPIO-PEG/MF, SPIO-PEG under magnetic field; SPION-PEG-D, SPIO nanoparticle with PEG conjugated with doxorubicin; SD, standard deviation; SPION-PEG-D/MF, SPION-PEG-D under magnetic field.....38

Figure 2-10. (A) Degradation curves of FD and SPIO-PEG-D over 114 hours. (B) DNA interstrand crosslinking in HT-29 cells after treatment with FD or SPIO-PEG-D for 24 hours. (C) Viability of HT-29 cells after incubation with FD, SPIO-PEG-D, or SPIO-PEG-D/MF (mean ± SD) (n=5). Abbreviation: FD, free doxorubicin; SPIO-PEG-D, superparamagnetic iron oxide with

doi:10.6342/NTU201902917

polyethylene glycol conjugated with doxorubicin; SPIO-PEG-D/MF, SPIO-PEG-D under magnetic field; SD, standard deviation. 39

Figure 2-11. In vivo MR imaging and detection of SPIO-PEG-D. Note: (A) T2-weighted MR images before and after treatment with SPIO-PEG-D (green arrows) or SPIO-PEG-D/MF (red arrows) and (B) MR signal intensity in mouse tumors (mean ± SD) (n=8). (C) Confocal laser scanning microscopic images of Dox in tumor tissues and microscope images of Prussian blue dye-stained tumor tissues after treatment with SPIO-PEG-D and SPIO-PEG-D/MF at 24 hours. Circled regions show the deposition of SPIO-PEG-D. (D) TEM image of tumor tissues after treatment with SPIO-PEG-D/MF. Black arrow indicates SPIO-PEG-D deposition. Abbreviation: MR, magnetic resonance; SPIO-PEG-D, superparamagnetic iron oxide with polyethylene glycol conjugated with doxorubicin; SPIO-PEG-D/MF, SPIO-PEG-D under magnetic field; SD, standard deviation; Dox, doxorubicin; TEM, transmission electron microscope. 40

Figure 2-12 Tumor growth inhibition test of sc HT-29 xenografts in BALB/c nude mice. Note: (A) Mice were IV injected with SPIO-PEG-D at a dose of 2.5 mg/kg Dox. The administration was carried out seven times with a 3-day interval (arrows: treatment days). (B) Body weight changes of the tumor-bearing mice. (C) TUNEL analysis of different tissue sections from the tumor-bearing mice treated with different therapeutics at a dose of 2.5 mg/kg Dox on day 40 after HT-29 cell implantation. The administration was carried out seven times with a 3-day interval. Green: apoptotic cells show green fluorescence (mean ± SD [n=4]. *P<0.05 and **P<0.01). Abbreviation: sc, subcutaneous; IV, intravenous; SPIO-PEG-D, superparamagnetic iron oxide with polyethylene

doi:10.6342/NTU201902917

glycol conjugated with doxorubicin; Dox, doxorubicin; TUNEL, terminal deoxynucleotidyl transferase dUTP nick-end labeling; SD, standard deviation; FD, free doxorubicin; SPIO-PEG-D/MF, SPIO-PEG-D under magnetic field. 41

Figure 3-1. Schematic illustration of hyperthermia-induced DOX release from iMNP-D. 64

Figure 3-2. Preparation of poly(AA-co-PEGDA-co-NIPAM) nanogels. 65

Figure 3-3. (1) 1H NMR spectra of poly (ethylene glycol) di-acrylamide and (2) HPLC chromatogram for (a) added iRGD and (b) unconjugated iRGD. 66

Figure 3-4. TEM images and DLS graphs for iMNP-D (1 and 2), MNP-D (3 and 4)...67

Figure 3-5. (1) Variation of magnetization for iMNP-D and (2) for MNP-D as a function of applied magnetic field. (3) TGA curves of the iMNP-D and (4) MNP-D. (5) X-ray powder diffraction pattern for iMNP-D. 68

Figure 3-6. (1) Relaxation response (r1) for iMNP-D and MNP-D, and (2) relaxation response (r2) for iMNP-D and MNP-D. 69

Figure 3-7. (1) In-vitro Dox release profiles for two nanogels, MNP-D and iMNP-D at neutral (pH 7.4) and acidic (pH 5.0) conditions at 37℃. (2) In-vitro Dox release profiles for two nanogels, MNP-D and iMNP-D at 37℃ and 42℃ at acidic (pH 5.0) conditions. (Mean±SD (n=5).....70

Figure 3-8. (1) T2-weighted MR phantom images of HT-29 cells after incubation with MNP-D, iMNP-D, or i+iMNP-D for 3 hr, 6 hr, or 24 hr, and (2) The iron uptake in HT-29 cells treated with 100 μg Fe/mL of MNP-D, iMNP-D, or i+iMNP-D at different incubation times. (3) Prussian blue staining images of HT-29 cells after 24 h treatment with MNP-D, iMNP-D, or i+iMNP-D.

doi:10.6342/NTU201902917

(Mean±SD (n=5). 71

Figure 3-9. (1) Viability of HT-29 cells after incubation with MNP and iMNP at 37℃ or 42℃. (2) Viability of HT-29 cells after incubation with MNP-D and iMNP-D at 37℃ or 42℃. (Mean±SD (n=5), *: P＜0.05; **: P＜0.01)..... 72

Figure 3-10. (1) T2-weighted MR images before and after treatment with MNP-D or iMNP-D, and (2) MR signal intensity in mouse tumors. (Mean±SD (n=5) , *: P＜0.05; **: P＜0.01). (3) Microscope images of Prussian blue dye stained tumor tissues after treatment with MNP-D or iMNP-D. 73

Figure 3-11. Tumor growth inhibition test of s.c. HT-29 xenografts in BALB/c nude mice. Mice were i.v. injected with MNP-D or iMNP-D at 37℃ or 42℃. The administration was carried out 5 times with a 3-day interval (green arrows: treatment days) (Mean±SD (n=10), *: P＜0.05; **: P＜0.01). (2) Body weight changes of the tumor-bearing mice. (Mean±SD (n=8). 74

Figure 3-12. (1) Dox concentrations in tumor tissues for the tumor-bearing mice treated with FD, MNP-D (37℃), iMNP-D (37℃), MNP-D (42℃),and iMNP-D (42 ℃). (Mean±SD (n=4), *: P＜0.05; **: P＜0.01). (2) Confocal laser scanning microscopic images of tumor tissues at 4 h after the injection. 75

Figure 3-13. TUNEL analysis of tumor sections obtained from s.c. HT-29 xenografts in BALB/c nude mice. Mice were treated with FD, MNP-D or iMNP-D at 37℃ or 42℃ on day 45 after HT-29 cell implantation. The administration was carried out 5 times with a 3-day interval. Green: apoptosis cells marked by FITC. 76

Fig 4-1. Through the esophageal cancer or cholangiocarcinoma, the NG tube or drainage tube with magnetic segment corresponding to the tumor location, can attract

doi:10.6342/NTU201902917

magnetic nanoparticles SPIO-PEG-D toward tumor, not only for feeding or drainage, but also for aggressive treatment of tumor 80
Fig 4-2. We can completely ablate the tumor by RFA alone at lethal temperature zone, but we should combine heat-triggered drug release in sublethal temperature zone to complete treat the tumor, because sublethal temperature is not high enough to kill the tumor 81

doi:10.6342/NTU201902917

List of Tables

Table 2-1 Characterization of SPIO-PEG and SPIO-PEG-D (n=3) 42

Table 3-1. Characterization of MNP-D and iMNP-D (n=3)..... 77

doi:10.6342/NTU201902917

Chapter 1. Background & Objectives

1.1. Unmet need of cancer chemotherapy

Cancer is the most common cause of death in Taiwan, with 48,037 people killed in 2017, a record high and the top 10 causes of death in 36 years, according to data released by Taiwan's Ministry of Health and Welfare. Therefore cancer therapy is currently a major focus of study. However, conventional chemotherapeutic drugs are distributed nonspecifically in the body where they affect both cancerous and healthy cells, resulting in dose-related side effects and inadequate drug concentrations reaching the tumor. In addition, the occurrence of resistance phenomena reduces the efficacy of cancer treatment.

1.2. Cancer nanomedicine

Recent progress in cancer nanomedicine raises exciting opportunities for specific drug delivery to overcome the lack of specificity of conventional chemotherapeutic drugs [1,2,3,4]. Nanoparticles can increase the intracellular concentration of drugs in cancer cells while minimizing toxicity in normal cells; thereby enhancing anticancer effects and reducing systemic toxicity simultaneously. Furthermore, nanoparticles offer the potential to overcome drug resistance by passing the P-glycoprotein efflux pump, one of the main drug resistance mechanisms, leading to greater intracellular drug accumulation.

1.3. Targeting drug delivery systems of nanomedicine

There are two types of targeting drug delivery systems as shown in figure 1-1,

doi:10.6342/NTU201902917

including passive targeting drug delivery system and active targeting drug delivery system.

1.3.1. Passive targeting drug delivery system

In passive targeting drug delivery system, nanomedicine accumulates preferentially in the neoplastic tissues as a result of the enhanced permeability and retention (EPR) effect [3,5,6,7]. The EPR effect is based on the nanometer size range of nanomedicines and two fundamental characteristics of neoplastic tissues such as the leaky vasculature and impaired lymphatic drainage. Normal tissue vasculatures are lined by tight endothelial cells, thereby preventing nanomedicines from escaping, however limitations of passive-targeting drug delivery system still remain.

The EPR effect helps the extravasated nanodrugs accumulated in the tumor interstitium, but it also induces the drug outflow from the cells as a result of a higher osmotic pressure in the interstitium, which eventually leads to nanodrug redistribution in some portions of the cancer tissue [8]. In addition, accumulation of the nanodrugs in the tumor microenvironment may not always correlate with therapeutic efficacy since internalization into the tumor cells is required for most anticancer drugs to exert their biological functions.

1.3.2. Active targeting drug delivery system

Active targeting drug delivery systems usually incorporate a targeting moiety on the nanoparticle surface to overcome the limitations of passive targeting drug delivery systems. The targeting moiety is expected to bind a tumor-associated antibody or receptor and facilitate the delivery of nanoparticles to the intracellular site of drug action, enabling a greater therapeutic effect. Active targeting nanoparticles show greater

doi:10.6342/NTU201902917

intracellular drug delivery to cancer cells than passive targeting nanoparticles, resulting in dramatically increased antitumor efficacy [9,10,11]. These findings suggest that the primary role of the targeting moiety is to enhance cellular uptake into cancer cells and to minimize cellular uptake for normal cells.

1.4. Magnetic nanoparticles

Magnetic nanoparticles are actively being developed due to their unique properties responsive to magnetic fields, including magnetic hyperthermia and MRI contrast agents [12,13,14,15]. The use of magnetic nanoparticles combined with therapeutic agents has increased exponentially over the past decade [16,17]. Their intrinsic magnetic properties enable these particles to be used in numerous medical applications, such as:

(1) Hyperthermia agents, where the magnetic particles are heated selectively by application of a high frequency external magnetic field [18,19];

(2) Magnetic carriers that can be directed by a magnetic field gradient towards a certain location [20,21];

(3) Tissue engineering [22,23,24];

(4) Magnetic contrast agents in magnetic resonance imaging (MRI) [25].

Magnetic-targeted drug delivery systems are magnetic nanoparticles that carry an anticancer drug to the target site by using an external magnetic field or internal magnetic field gradient.

A magnet applied from outside the body can direct the magnetic nanodrug to the target site as shown in Figure 1-2. This can keep a larger amount of the anticancer drug at the tumor site for a longer period of time and prevent normal tissues from the side effects of chemotherapy [16].

The main requirements which the magnetic-targeted carrier should possess are the

doi:10.6342/NTU201902917

following:

(1) Biocompatibility to prevent toxicity, enhance cell survival and reduce inflammatory responses;

(2) Biodegradability to improve clearance from the body;

(3) Capability to act as a drug carrier and exhibit controlled drug release;

(4) Structural stability to allow delivery of anticancer drugs after reaching target site;

(5) Stealth surface characteristics to prolong the circulation time, improve colloidal stability, prevent agglomerations and reduce toxicity; and

(6) Reproducible sizes and shapes for clinical applications.

1.5. Control releasing (pH/temperature dually responsive systems)

The switching of release kinetics in nanocarriers of anticancer drugs, from a slow rate during circulation to a fast rate at tumor sites, has been hypothesized to benefit cancer chemotherapy [26]. It is believed that a slow release prior to the reaching of the target tumor site reduces drug induced side effects, while a fast release in the tumor site tends to improve tumor treatment [27,28,29]. Control releasing drug delivery systems are responsive to a specific tumor signal, which is commonly a temperature- or pH-sensitive release due to a higher temperature and/or a lower pH observed in cancer tumor microenvironments.

A variety of approaches have been attempted, including the construction of thermos-responsive polymeric micelle systems that respond to hyperthermic conditions (42 °C) [30], and pH-sensitive systems that respond to endosomal pH via the cleavage of pH labile chemical bonds [31]. Dually responsive systems are promising for multifunctional systems. Particularly in therapeutic applications, they can act as drug

doi:10.6342/NTU201902917

carriers for intracellular delivery [32].

1.6. Multifunctional nanoparticles for targeted imaging and therapy

Multifunctional nanoparticles convey unique advantages for cancer-specific targeted delivery of imaging and therapeutic agents [25]. Multifunctional nanoparticles for combining SPIONs and anticancer drug can make cancer theranostics possible using MRI as a diagnostic tool and directing the magnetic carrier to a tumor by magnetic gradient or external applied magnet with treating the tumor by magnetic hyperthermia [33,34,35,36,37].

Figure 1-3 shows Surface modifications for multifunctional nanoparticles with tumor-associated antibody or receptor may increase the binding affinity of particles toward target cells by receptor-mediated endocytosis [38]. Multifunctional nanoparticles with pH/temperature sensitive moiety can reduce drug induced systemic side effects and improve local tumor treatment effect [27,28,29]. Surface modifications for multifunctional nanoparticles may be easily introduced through conjugation with targeting moieties such as antibodies, peptides, small molecules, or aptamers, fluorescence dyes, genes, or drugs to provide multimodal functionalities [39,40,41].

1.7. Objectives

The aim of the first part is to develop a magnetic-targeted drug delivery system for MRI diagnosis and for targeting and treating the tumor with a chemotherapy agent by externally applied magnet.

The aim of the second part is to develop receptor-mediated active targeting drug delivery system, with pH/temperature sensitive moieties, to target and control releasing

doi:10.6342/NTU201902917

a chemotherapy agent to the tumor. While, the chemotherapy agent was encapsulated in nanogel particles to decrease the systemic side effect.

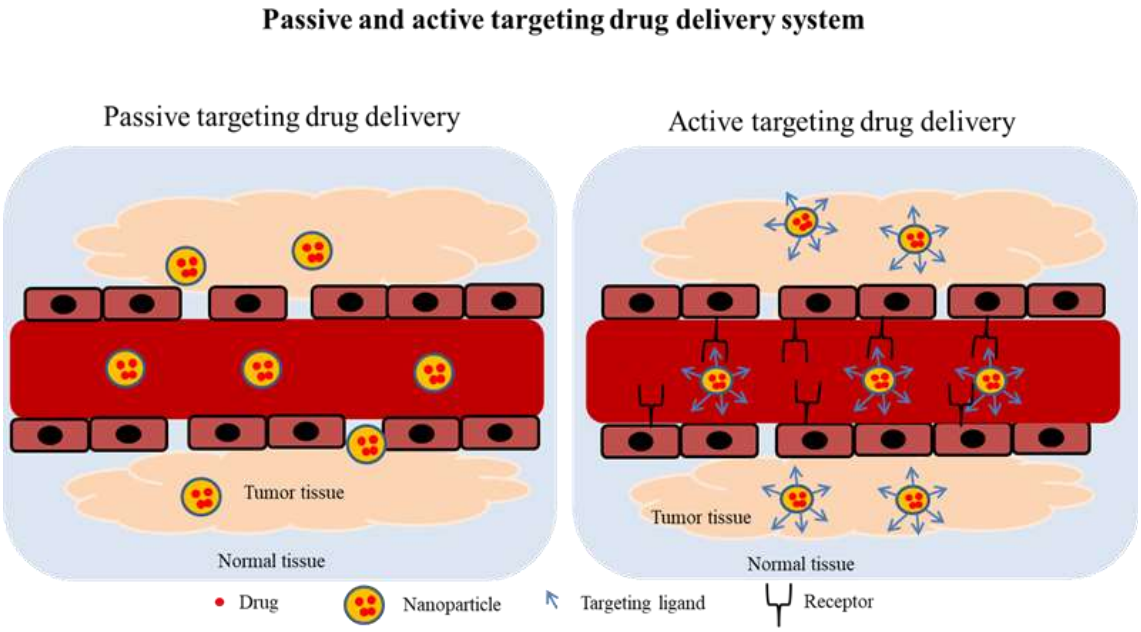

Figure 1-1. Passive targeting drug delivery system was achieved by tumor vascular endothelial gap and impaired lymphatic drainage of tumor tissue, thus enhanced permeability of nanoparticle from endothelial gap into tumor tissue, and enhanced retention in tumor tissue, so called enhanced permeability and retention (EPR) effect. Active targeting drug delivery system with targeting ligand on the nanoparticle surface, to bind a tumor-associated receptor and facilitate the delivery of nanoparticles to the intracellular site by receptor-mediated endocytosis (RME), enabling a greater antitumor efficacy.

doi:10.6342/NTU201902917

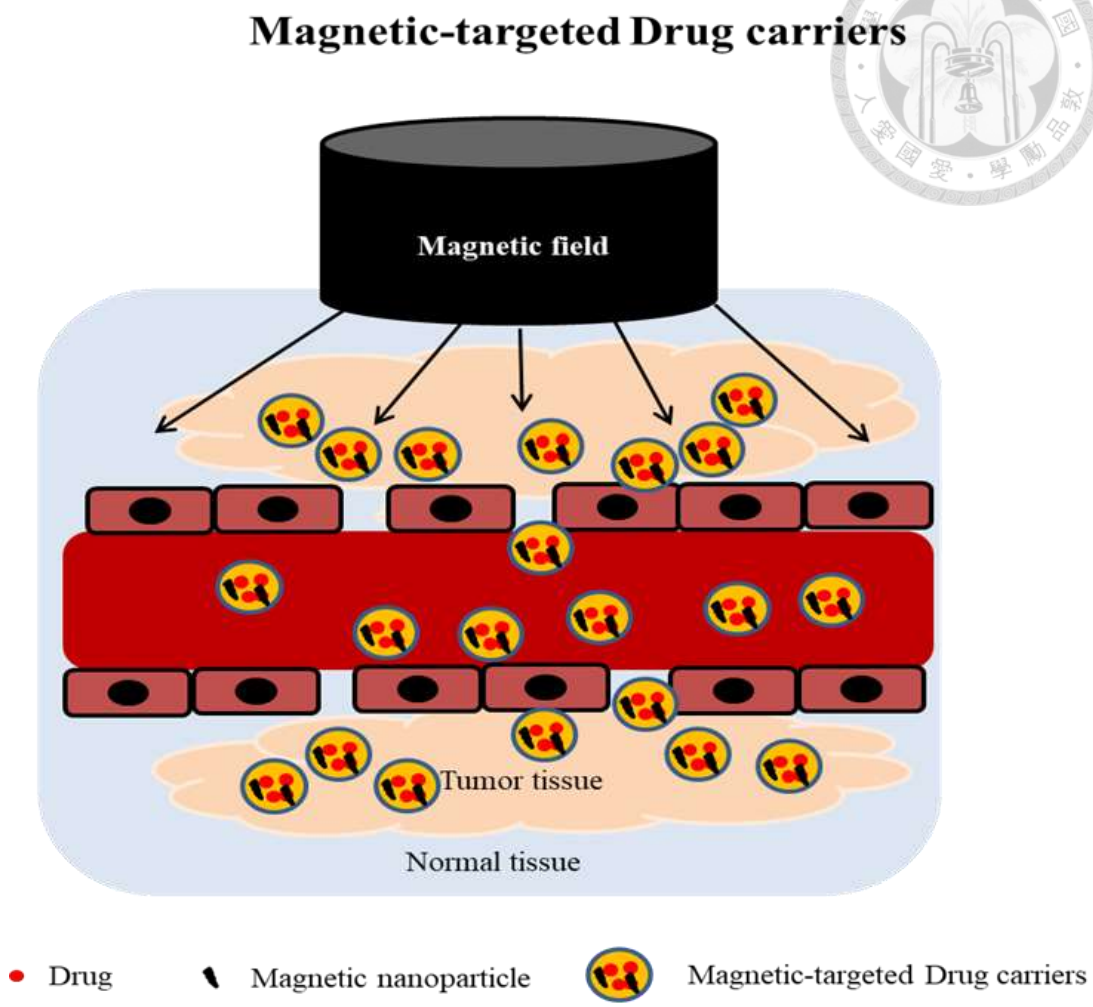

Figure 1-2. Magnetic-Targeted drug delivery systems are magnetic nanoparticles that carry anticancer drug to the target tumor tissue by using an external magnet, which can keep larger amount of anticancer drug at tumor site for longer time, and prevent normal tissue from side effects of chemotherapy.

doi:10.6342/NTU201902917

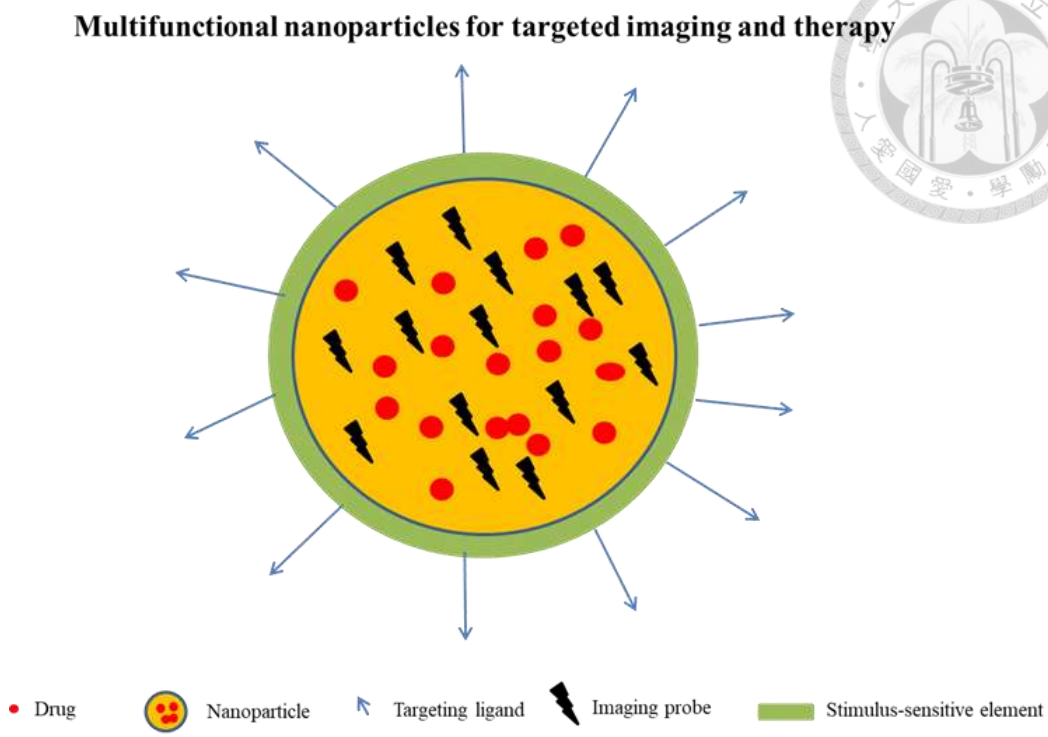

Figure 1-3. Multifunctional nanoparticles surface modifications with tumor-associated targeting ligand may increases the binding affinity toward tumor cells by receptor-mediated endocytosis. Multifunctional nanoparticles with pH/thermosensitive moieties, can control releasing anticancer drug in tumor cells, thus improving local tumor treatment effect and reducing drug induced systemic side effects. Multifunctional nanoparticles with SPIO as imaging probe, may use MRI as a diagnostic tool, and make theranostics possible.

doi:10.6342/NTU201902917

Chapter 2. (My study Part I)

Doxorubicin-eluting magnetic nanoparticles as a drug delivery system for magnetic resonance imaging-monitoring magnet-enhancing tumor chemotherapy

2.1. Introduction

Nanoparticles have been developed for their great potential application in drug delivery systems and tumor diagnosis [42,43,44,45,46]. The development of multifunctional nanoparticles for the delivery of both therapeutic and contrast agents to cancer tumors would be possible for tumor theranostics [33,35,36]. In addition, nanoparticles offer many functions, such as combining magnetic resonance imaging (MRI) contrast agent, chemotherapeutics, and active targeting, in one nano-carrier, representing a novel strategy in nanomedicine [47,48,49,50].

Doxorubicin (Dox) is one of the most effective anticancer drugs against many types of cancer tumors. However, its clinical application is limited by its side effects and drug resistance. Consequently, many new nanocarriers, such as polymeric nanoparticles [51,52], are widely used to reduce the side effects of anticancer drugs and improve their half-life in blood circulation. However, these systems cannot be controlled to release drugs accurately. Therefore, it is important to combine the nano-carrier with a targeting method to reduce the side effects of the anticancer drugs on healthy organs.

Superparamagnetic iron oxide (SPIO) nanoparticles possess specific magnetic properties as being an effective contrast agent for MRI to increase the detection and characterization of tumor lesions within the body. The magnetic property of

doi:10.6342/NTU201902917

Superparamagnetic iron oxide nanoparticles (SPIONs) can also be used as a magnetically guided drug delivery method for a lesion-targeting system. Magnetic nanoparticles are actively being developed based on their unique properties responsive to magnetic fields, including magnetic hyperthermia and MRI contrast agent [12,13,14,15]. Active targeting for superficial tumors can also be performed using magnetic fields [53,54,55,56].

This strategy has been tested in patients with advanced stages of cancer [57,58]. Many targeting studies [59,60,61,62] were focused on the magnetic particles as drug carriers, but the half-life of these particles is very short, restricting their use through the systemic route. Magnetic vehicles are attractive for the targeting delivery of therapeutic agents to specific locations in the body through the application of a magnetic field. The magnetic localization of therapeutic agents results in a higher concentration of the therapeutics at the target site and consequently reduces the side effects of systemic drug administration. The first clinical cancer therapy trials in humans using magnetic particles were reported and involved treatment of advanced solid liver cancer in 14 patients [62]. The results showed that the magnetic particles accumulated in the magnetic target area and were nontoxic [62]. The targeting using magnetic drug nanocarriers could provide a higher drug accumulation at tumor sites for cancer therapy with a lower therapeutic dose [61,62].

Although SPIO is a well-known drug carrier, it has many disadvantages, such as low water solubility and a lack of targeting ability. Therefore, it is important to combine the nanocarrier with a targeting modality to reduce the side effects of chemotherapeutic agents on normal organs. The biocompatibility of polymers, such as polyethylene glycol (PEG), has been demonstrated both in vivo and in vitro, and such compounds have been applied to tissue engineering. Imparting a stealth shielding on the surface of

doi:10.6342/NTU201902917

nanoparticles can prevent opsonization by the reticuloendothelial system (RES) cells and then increase the circulation time from minutes to hours or days [63]. PEG modification has emerged as a customary method to ensure stealth shielding and to improve the circulation time of therapeutic agents or delivery devices. The hydrophilic PEG can improve the biocompatibility of the delivery system because most of the biological environment is hydrophilic, and biocompatibility appears to be correlated with the degree of hydrophilicity exhibiting on the surface.

We developed multifunctional SPIONs consisting of a magnetic Fe_3O_4 core and a shell of aqueous stable PEG conjugated with Dox (SPIO-PEG-D) for tumor MRI-monitoring chemotherapy. One of the major advantages for SPIO with PEG (SPIO-PEG) as a drug carrier is that the degradation of Dox could be effectively reduced by conjugating Dox on the surface of SPIO-PEG. The degree of freedom of Dox on SPIO-PEG was limited to prevent its molecular distortion and hence increase its half-life. In addition, SPIO-PEG-D could cause DNA crosslink more serious, resulting in a lower DNA expression and a higher cancer cell apoptosis. Finally, the accumulation of SPIO-PEG-D in cancer tumors could be enhanced by applying a magnetic field in the tumor to increase the degree of DNA crosslink and to reduce the damage of normal organs. This functionalized nanoparticle with high payload of Dox, high superparamagnetic property, and high MRI relaxivity could not only be an effective magnetic targeting carrier for anticancer drug but also be a great MRI contrast agent. Figure 2-1 shows how the developed functionalized, magnetic nanoparticles can achieve the objective of improving the drug transport to tumors.

Doxorubicin hydrochloride (Dox HCl) was obtained from Seedchem (Melbourne, Australia). Succinic anhydride, 4-dimethylamino-pyridine, sodium hydroxide, PEG (MW = 2,000 Da), 2-(N-morpholino) ethanesulfonic (MES) acid hydrate, thionyl

doi:10.6342/NTU201902917

chloride, triethylamine, 3-aminopropyl triethoxysilane, 1-ethyl-3-(3-(dimethylamino)-propyl)carbodiimide, and N-hydroxysulfosuccinimide were purchased from Sigma-Aldrich (St Louis, MO, USA) and used as received. Iron(III) chloride ($FeCl_3$) 99% pure granulated and iron(II) chloride tetrahydrate ($FeCl_2 \cdot 4H_2O$) were purchased from Merck (Whitehouse Station, NJ, USA). Oleic acid (IO), dichloromethane, isopropyl ether, and toluene were purchased from Thermo Fisher Scientific (Waltham, MA, USA).

2.2. Materials and Methods

2.2.1. Materials

Dox HCl was obtained from Seedchem (Melbourne, Australia). Succinic anhydride, 4-dimethylamino-pyridine, sodium hydroxide, PEG (MW = 2,000 Da), 2-(N-morpholino)ethanesulfonic acid hydrate (MES), thionyl chloride, triethylamine, 3-aminopropyl triethoxysilane, 1-ethyl-3-(3-(dimethylamino)-propyl)carbodiimide, and N-hydroxysulfosuccinimide were purchased from Sigma-Aldrich (St Louis, MO, USA) and used as received. Iron(III) chloride ($FeCl_3$) 99% pure granulated and iron(II) chloride tetrahydrate ($FeCl_2 \cdot 4H_2O$) were purchased from Merck (Whitehouse Station, NJ, USA). Oleic acid (IO), dichloromethane, isopropyl ether, and toluene were purchased from Thermo Fisher Scientific (Waltham, MA, USA).

2.2.2. Synthesis of HOOC-PEG-triethoxysilane (HOOC-PEG silane)

Fifty grams of PEG, 2.6 g of succinic anhydride, and 0.6 g of 4-dimethylamino-pyridine were dissolved in 150 mL of dichloromethane at 30°C and stirred for 24 hours to form PEG-carboxylate. A 0.45 mL of thionyl chloride was added

doi:10.6342/NTU201902917

to the PEG-carboxylate solution at 30°C. Then, triethylamine was added to adjust the solution pH to be ~5. A total of 1.5 mL of 3-aminopropyl triethoxysilane was added to the solution mixture at 30°C, and the mixture was stirred for 10 hours. The HOOC-PEG-triethoxysilane was crystallized with isopropyl ether and dried under vacuum. The synthetic scheme of the HOOC-PEG silane is shown in Figure 2-2.

2.2.3. Synthesis of magnetite nanoparticles with IO

Ferric chloride (30 mmol) and ferrous chloride tetrahydrate (15 mmol) were dissolved in 50 mL of water. One-normal sodium hydroxide solution was added to the mixture solution until pH reached 12. Five milliliters of IO were added to the dark solution and formed a black precipitate. The precipitate was centrifuged at 6,000 rpm for 10 minutes, washed with water, and isolated as black pellet. The pellet was redispersed in water, and the pH of solution was adjusted to 4 using 6 N HCl. The resulting mixture was centrifuged at 9,000 rpm for 30 minutes to collect dark precipitate and dried under vacuum for 2 days. The dark solid was redispersed in toluene and centrifuged at 9,000 rpm for 30 minutes to collect the supernatant. The supernatant was filtered through 0.45 μm polytetrafluoroethylene filter and collected as an IO nanoparticle suspension solution.

2.2.4. Synthesis of SPIO-PEG

Six grams of HOOC-PEG-triethoxysilane was added to the IO nanoparticle solution and vigorously stirred for 1 day. The resultant HOOC-PEG-immobilized IO nanoparticles were extracted with 2,000 mL of water, and the aqueous layers were collected. The SPIO-PEG nanoparticles in aqueous solution were washed, purified, and concentrated with ultrafiltration. The Fe concentration of the purified SPIO-PEG

doi:10.6342/NTU201902917

solution was determined by inductively coupled plasma spectroscopy. The SPIO-PEG powder was obtained by lyophilization and was analyzed with thermogravimetric analyzer (PerkinElmer Pyris 1; PerkinElmer, Waltham, MA, USA). The thermogravimetric analyses were carried out with 5 mg of SPIO-PEG powder, and the SPIO-PEG powder was heated from 25°C to 850°C at a heating rate of 10°C/min.

2.2.5. Synthesis of SPIO-PEG-D

Twenty-five milligrams of 1-ethyl-3-(3-(dimethylamino)-propyl)carbodiimide and 28 mg of N-hydroxysulfosuccinimide were dissolved in 1.5 mL of 0.5 M MES, and then 0.2 mL of the solution was mixed with 0.2 mL of SPIO-PEG solution at 4°C and sonicated for 30 minutes. After that, the aqueous solution was washed with 1 mL of 0.1 M MES buffer and then resuspended in 0.3 mL of MES. The resulting mixture was mixed with 0.1 mL of Dox by vortexing for 6 hours at 4°C. The amino groups of Dox reacted with active ester and resulted in covalent conjugation of Dox on the SPIO-PEG surface. Finally, the solution was washed with water to remove unbound Dox and dispersed in 0.3 mL of water. The binding capacity of Dox was analyzed using high-performance liquid chromatography (HPLC), and the mobile phase was a 50/15/35 (v/v/v) mixture of water, acetonitrile, and methanol with a flow rate of 1.5 mL/min. The synthetic route for SPIO-PEG-D is shown in Figure 2-3.

2.2.6. Analysis of particle properties

The core particle size of SPIO-PEG and SPIO-PEG-D nanoparticles was analyzed by a transmission electron microscope (TEM) (JEM-2010HR; JEOL, Tokyo, Japan). The mean hydrodynamic diameter of SPIO-PEG and SPIO-PEG-D nanoparticles was analyzed by dynamic laser light scattering (Malvern Zetasizer 3000HSA; Malvern

doi:10.6342/NTU201902917

Instruments, Malvern, UK) at a fixed angle of 90° and a temperature of 25°C. The zeta potential of SPIO-PEG and SPIO-PEG-D nanoparticles was measured using Zetasizer Nano ZS (Malvern Instruments). The crystal lattice properties of nanoparticles were detected by X-ray powder diffraction (Siemens D5000) with the monochromatized Cu K radiation. The magnetic properties were measured with vibrating-sample magnetometer (model 7300; Lakeshore, Westerville, OH, USA). The longitudinal (r1) and transverse relaxivities (r2) of nanoparticles and the magnetic relaxation time (T1, T2) of particle solutions were measured out on a 0.47 T 20 MHz Bruker Minispec (Bruker Medical GmbH, Ettlingen, Germany). The nanoparticles were prepared by dilution to final Fe concentrations ranging from 0.1 to 0.5 mM in water. The r1 and r_2 relaxivities were calculated from the slope of $1/T_1$ and $1/T_2$ plotted against the Fe concentration. A liquid sample of stock solution was used for the Fourier transform infrared spectroscopy analysis (TENSOR Model 27; Bruker Medical GmbH).

2.2.7. MRI analysis of nanoparticles in cancer cells

HT-29 human colon carcinoma cells (Bioresource Collection and Research Center, Taiwan) were grown in astrocyte medium. The human colon cancer cell HT-29 is an established cell line and contained no identity of the patient. Our study was not considered human subject research and did not require ethical approval from the Institutional Research Board. The cells were cultured in standard conditions (at 37°C with 5% CO_2 in a humidified incubator) and subcultured after reaching 80% confluence. HT-29 cancer cells were grown in 175 cm^2 culture flasks at a density of 1×10^5 cells per mL, and the cell internalization of nanoparticles was measured with MRI. The experiments consisted of two groups: one treated with SPIO-PEG-D alone and the other treated with SPIO-PEG-D with a 0.4 T magnet attached to the plate bottom. The

doi:10.6342/NTU201902917

SPIO-PEG-D solution was added to each well at a concentration of 50 μg Fe/mL. After incubation for 3, 6, or 24 hours, the medium was removed, and the plates were washed four times with phosphate-buffered saline (PBS) buffer and then suspended in 300 μL of 0.5% agarose gel. Finally, the samples were transferred to a 96-well plate, and MRI was performed on a 3.0 T MRI scanner (MAGNETOM Trio, A Tim System 3T; Siemens, Munich, Germany).

2.2.8. Qualitative and quantitative studies of cellular uptake

Prussian blue iron staining was used to visualize the cellular uptake of SPIO-PEG-D. The experiment consisted of two groups: one treated with SPIO-PEG-D alone and the other treated with SPIO-PEG-D with a 0.4 T magnet attached to the plate bottom. HT-29 cancer cells were seeded in a six-well chamber slide (1×10^5 per well) and incubated with Dulbecco's Modified Eagle's Medium and 5% fetal calf serum containing SPIO-PEG-D at a concentration of 40 μg Fe/mL for 24 hours. Then, the cells were washed with PBS buffer solution and fixed with 3% paraformaldehyde for 20 minutes. To analyze Prussian blue staining, cells were washed with PBS and incubated with 2% potassium ferrocyanide in 6% HCl. After that, the cells were washed with PBS buffer and then observed under an inverted microscope. To quantitatively determine the cellular uptake, HT-29 cancer cells were seeded in 24-well plates (1×10^5 per well) for 24 hours. The SPIO-PEG-D solution was added separately to each well at a concentration of 100 μg Fe/mL. After incubation for 0.5, 1, 3, 5, or 24 hours, the medium was removed, and the plates were washed with PBS buffer solution. Then, the cells were trypsinized and counted using a hemocytometer. The cell suspension was centrifuged at 2,000 rpm for 5 minutes to form cell pellets, and then 2 mL of hydrochloric acid was added to each pellet. After that, the mixture solution was heated

doi:10.6342/NTU201902917

to 80°C for 5 minutes and diluted with water. Finally, all samples were analyzed using inductively coupled plasma mass spectrometer (Agilent ICP-MS 7500).

2.2.9. Degradation test for free Dox and SPIO-PEG-D

The mobile phase was a 50/50 (v/v) mixture of acetonitrile and mixture solution containing sodium lauryl sulfate (10 g), 80% phosphoric acid (2.5 mL), and water (1,000 mL) with a flow rate of 1.0 mL/min. The ultraviolet (UV) detection was performed at 298 nm, and the internal standard was a 50 mg/mL of papaverini hydrochloridum solution. The degradation of free Dox (FD) and SPIO-PEG-D was analyzed for a period of 114 hours at 37°C.

2.2.10. DNA interstrand crosslink

The ethidium bromide fluorescence assay was used to analyze the degree of DNA interstrand crosslink for HT-29 cells to assess the cytotoxic effects of Dox. The cells were exposed to 1–7 μM of FD or SPIO-PEG-D and incubated for 24 hours. Then, 1×10^5 cells were collected by centrifugation at 5,000 rpm for 10 minutes at 5°C. Forty milliliters of the cell suspension was incubated for 20 minutes at 4°C with 200 mL of lysis buffer. Then, the cell pellets were separated by centrifugation at 5,000 rpm for 10 minutes and incubated with 30 mL of heparin for 30 minutes at 37°C. After that, 1 mL of ethidium bromide solution was added in the mixture, and the mixture was heated for 10 minutes at 100°C. Finally, the mixture was cooled in an ice bath for 10 minutes, and fluorescence of all samples was measured with excitation and emission wavelengths of 525 and 580 nm, respectively.

2.2.11. Cell MTT cytotoxicity

doi:10.6342/NTU201902917

MTT cytotoxicity test was used to analyze the cytotoxic effect of SPIO-PEG-D nanoparticles on cancer cells. HT-29 cells were seeded on a 96-well plate at a density of 1×10^5 cells/well in 100 μL of Dulbecco's Modified Eagle's Medium containing 5% fetal calf serum for 24 hours. The concentration range of Dox was from 1 to 10 μM. Cells incubated without any drug were used as the blank control group. The experiments consisted of three groups: FD, SPIO-PEG-D alone, and SPIO-PEG-D with a 0.4 T magnetic field. After treatment, the cells were incubated for 5 hours, and 5 mg/mL of 3-(4,5-dimethylthiazol-2-yl)-2,5-diphenyl tetrazolium bromide was added (20 μL/well) and incubated for 5 hours. The HT-29 cancer cells were then lysed with dimethylsulfoxide (100 μL) and placed in the incubator at 37°C overnight. The absorbance values of lysed cells were detected by a microplate reader (model 680; Bio-Rad Laboratories Inc., Hercules, CA, USA) at a wavelength of 490 nm.

2.2.12. In vivo MR image and detection of iron

Male Sprague Dawley rats (180–190 g) were obtained from the National Laboratory Animal Center (Taiwan). All experimental protocols were approved by the Institutional Animal Care and Use Committee of the College of Medicine, National Taiwan University. The rats were housed with a 12-hour light/dark cycle and allowed free access to water and standard diet. CT-26 cancer cells were transplanted subcutaneously into the right and left thigh of the rats (6×106 cells/0.1 mL). Sixteen tumor-bearing rats were randomly divided into two groups (12 and 24 hours) for the in vivo MR image experiment. Seven days later, sixteen rats were intravenously injected with SPIO-PEG-D nanoparticles (18 mg Fe/kg) and then with a 0.4 T magnet secured to the left thigh for 12 or 24 hours. The rats were assessed longitudinally by MR image after treatment to determine the tumor size. The MR images were acquired on a 3 T

doi:10.6342/NTU201902917

scanner (Trio with Tim; Siemens) and quantified using T_2-weighted images with the following parameters: repetition time =4,230 ms, echo time =96 ms, slice thickness =1 mm, field of view 48×75 mm, bandwidth 260 Hz/px, resolution =164×256, averages =2, and total scan time =1 minute 37 seconds. After that, male rats bearing tumor were treated with SPIO-PEG-D or SPIO-PEG-D under a 0.4 T magnetic field (SPIO-PEG-D/MF) at a dose of 18 mg/kg Dox. The animals were perfused with saline and 4% paraformaldehyde at 24 hours after the SPIO-PEG-D administration. Tumors were extracted and immersed in the same fixative solution for 4 hours. Before analysis, the tumor tissue was embedded in Tissue-Tek optimum cutting temperature compound (Thermo Fischer Scientific, Waltham, MA, USA) on a specimen disk and cryo-frozen immediately in liquid nitrogen. Subsequently, the tumor tissue was sectioned into 20 μm thick slices with microtome (Cryostat, Leica CM3050s; Leica Biosystems, Wetzlar, Germany). The tumor tissue slices were dried on the gelatin-coated microscopic slides. The slides were rinsed three times and mounted using the Dako Fluorescence Mounting Medium (Dako, Glostrup, Denmark). The tumor tissue sections were imaged under Olympus FV1000 confocal microscope (Olympus, Tokyo, Japan). After that, the tumor tissues were fixed in 10% neutral buffered formalin, processed, and embedded with paraffin for detection of iron expression by Prussian blue staining. The tumor tissues were fixed in phosphate buffer containing 25 mg/mL glutaraldehyde, postfixed in 10 mg/mL osmium tetroxide, dehydrated in alcohol, and embedded for cellular uptake analysis. Finally, the sections were stained with uranyl acetate and lead citrate and then examined using a TEM.

2.2.13. In vivo antitumor activity

Female BALB/c nude mice (30±2 g) were obtained from the National Laboratory

doi:10.6342/NTU201902917

Animal Center (Taiwan). HT-29 cancer cells were transplanted subcutaneously into the abdomen of mice (1×10^5 cells/0.1 mL). Seven days later (size of tumor: ~60 mm^3), the experiments were executed for three groups (n=4 for each group): one group intravenously injected with FD (2.5 mg Dox/kg), another group injected with SPIO-PEG-D nanoparticles (2.5 mg Dox/kg) alone, and the other group injected at the same dose of SPIO-PEG-D and a 0.4 T magnet secured to the hypodermic tumor for 24 hours. The administration was carried out seven times with a 3-day interval for each mouse. The tumor size was calculated by the formula $a\times b^2/2$, with a and b being the longest and shortest diameter, respectively.

2.2.14. Apoptosis detection for tumor cells

The treated mice were sacrificed for apoptosis detection on day 40 after tumor implantation. After sacrifice, the mice were perfused using transcardiac method with 10% neutral buffered formalin. Tumor, heart, kidney, and liver tissues were collected and fixed with 10% neutral buffered formalin for at least 48 hours. The apoptotic cells in tissues were detected with terminal deoxynucleotidyl transferase dUTP nick-end labeling (TUNEL) assays using an in situ cell death detection kit and observed using Olympus FV1000 confocal microscope (Olympus).

2.3. Results and discussion

2.3.1. Synthesis of HOOC-PEG-triethoxysilane (HOOC-PEG silane) and thermal properties of nanoparticles

HOOC-PEG silane was analyzed by 1H NMR spectroscopy using a 400 MHz Bruker spectrometer (AVANCE model; Bruker) at 25°C, and the result is shown in

doi:10.6342/NTU201902917

Figure 2-4A. 1H NMR ($CDCl_3$, δ in ppm): 4.05 (brm, CH_2CH_2OCO–), 3.77 (quart, –$SiOCH_2CH_3$–), 3.46 (brm, –CH_2CH_2O–), 3.24 (brm, –$NHCH_2CH_2CH_2Si$–), 1.80 (brm, –$NHCH_2CH_2CH_2Si$–), 1.15 (trip, –$SiOCH_2CH_3$–), 0.55 (brm, –$NHCH_2CH_2CH_2Si$–). Figure 2-4B shows the dynamic thermogravimetric curves of SPIO-PEG nanoparticles. The initial 5% of total weight loss was due to the residual water. The 75% of total weight loss between 250°C and 450°C was attributed to the thermal degradation of PEG coated on the SPIO surface. The 20% of residual weight after 750°C was counted as the iron oxide.

2.3.2. Characterization of nanoparticles

Figure 2-5 shows the particle size of SPIO-PEG and SPIO-PEG-D nanoparticles. The TEM images displayed the core particle size and morphology for both SPIO-PEG and SPIO-PEG-D nanoparticles. The size of core particles is ~6–10 nm on average for both SPIO-PEG and SPIO-PEG-D nanoparticles, and the high-resolution TEM micrograph showed that the core particles of both SPIO-PEG and SPIO-PEG-D were spherical in shape. The hydrodynamic diameter indicated that the average particle size was ~70 and 85 nm for SPIO-PEG and SPIO-PEG-D, respectively. The discrepancy of the measured particle sizes between dynamic laser light scattering and TEM is a hydrophilic PEG layer conjugated on the surface of nanoparticles. The PEG layer increases the hydrodynamic diameter due to the flexibility of the PEG backbone [64,65,66]. Table 2-1 shows the characterization of SPIO-PEG and SPIO-PEG-D. The hydrodynamic diameter was 70±2.3 and 85±3.1 nm, and polydispersity index was 0.213±0.03 and 0.242±0.05 for SPIO-PEG and SPIO-PEG-D, respectively. The zeta potential of SPIO-PEG in water was −14.2±0.4 mV, and it increased to −1.8±0.21 mV when Dox was conjugated with SPIO-PEG. SPIO-PEG-D is stable in water for a period of 12 months (Figure 2-5E), and

doi:10.6342/NTU201902917

the SPIO-PEG-D particles did not aggregate and change the particle size, and such stability is desirable for use in biological applications.

2.3.3. Qualification and quantification of SPIO-PEG-D

The characteristic absorption peaks of SPIO-PEG, Dox, and SPIO-PEG-D were confirmed by Fourier transform infrared spectroscopy analysis (Figure 2-6A). The O–H (3,405 cm^{-1}) and C=O (1,652 cm^{-1}) peaks are from COOH of SPIO-PEG. The N–H bond and C–O bond from Dox appear at 1,553 and 1,645 cm^{-1}, respectively. The bands at 3,427 and 3,251 cm^{-1} are attributed to NH_2 stretching band on Dox. The characteristic absorption peaks of SPIO-PEG-D showed C=O bonds at 1,692 cm^{-1}, and C–N stretching band from amide bond appears at 1,403 cm^{-1}. The peak at 3,430 cm^{-1} is attributed to N–H stretching band from amide bond. This result indicated the amide bond formation between the carboxyl groups of SPIO-PEG and the amino groups of Dox. The HPLC measurement showed that the amount of Dox conjugated with SPIO-PEG-D increased as the amount of Dox added increased and reached a saturating concentration of 520 μg Dox/mg SPIO-PEG-D (Figure 2-6B).

2.3.4. Structural analysis and magnetic properties of SPIO-PEG and SPIO-PEG-D

In Figure 2-7A, the X-ray diffraction of SPIO-PEG-D nanoparticles shows detectable peaks at 30.2°, 35.7°, 43.7°, 54.8°, 57.5°, and 63.1°. These peaks are similar to the characteristics of Fe_3O_4 nanoparticles [67]. The magnetic properties of SPIO-PEG and SPIO-PEG-D were evaluated by vibrating sample magnetometer and are shown in Figure 2-7B and C. The saturation magnetization value for SPIO-PEG and SPIO-PEG-D was 75 and 63 emu/g, respectively. The decrease of magnetization value for SPIO-PEG-D, as compared to SPIO-PEG, occurred due to the proportional decrease of

doi:10.6342/NTU201902917

Fe_3O_4 in the same mass of SPIO-PEG-D. The shape of the hysteresis curves for SPIO-PEG and SPIO-PEG-D was tight together with no significant hysteresis loss, which is expected as the behavior of superparamagnetism [68].

2.3.5. Relaxivity

The longitudinal and transverse relaxation times (T_1, T_2) for SPIO-PEG and SPIO-PEG-D solutions were detected with a 0.47 T, 20 MHz magnetic relaxometer. The magnetic relaxivities (r_1, r_2) were calculated as the slope of $1/T_1$ and $1/T_2$ versus five different iron concentrations, respectively, as shown in Figure 2-8. There is no significant difference in r_1 between these two nanoparticles. The r_2 value of SPIO-PEG-D nanoparticles was smaller than that of SPIO-PEG, as a result of the conjugation of Dox that covers the SPIO surface and then reduces the paramagnetic effect. The result was shown in the r_2 and r_1 measurements; the r_2/r_1 ratio is 9 and 12 for SPIO-PEG-D and SPIO-PEG, respectively. The r_2/r_1 ratios for both SPIO-PEG-D and SPIO-PEG were higher than Resovist® (a commercial iron oxide nanoparticle with an r_2/r_1 ratio ~7), indicating that both SPIO-PEG-D and SPIO-PEG are more effective than Resovist® as a T_2 contrast agent.

2.3.6. In vitro qualitative and quantitative studies of cellular uptake

MRI and cell viability were used to evaluate the potential of SPIO-PEG-D as an MR contrast agent and as an agent for magnetic-targeting chemotherapy. HT-26 cells were first incubated with SPIO-PEG-D or SPIO-PEG-D/MF for 3, 6, and 24 hours. Figure 2-9A shows the T_2-weighted MR images of HT-29 cells after incubation. The rapid and effective magnetic targeting leads to distinguishably darkened MR images for the SPIO-PEG-D/MF group, as compared to the SPIO-PEG-D group, at a concentration

doi:10.6342/NTU201902917

of 50 μg Fe/mL. The result also indicated that there was a significantly higher cellular uptake for the SPIO-PEG-D/MF group than the SPIO-PEG-D group, and this multifunctional drug carrier could enhance the MR sensitivity to produce a better monitoring and chemotherapy with an application of magnetic field.

Prussian blue staining studies were performed to evaluate the uptake of SPIO-PEG-D by HT-29 cancer cells, and the results are shown in Figure 2-9B. The figure indicates that the SPIO-PEG-D/MF group had an enhanced cellular uptake of nanoparticles, shown as a higher Fe concentration, than the SPIO-PEG-D group. The results of iron concentration inside the cancer cells are shown in Figure 2-9C. The SPIO-PEG-D/MF group displayed a significantly higher cellular uptake of nanoparticles by HT-29 cells than the SPIO-PEG-D group. This is because a higher accumulation of SPIO-PEG-D in the region of HT-29 cells increases the cellular internalization when the system is exposed to a magnetic field. This result demonstrated that the application of a magnetic field can positively affect the efficiency of cellular uptake for SPIO-PEG-D nanoparticles.

2.3.7. In vitro degradation and anticancer cell efficiency test

To determine the thermal stability of Dox conjugated to SPIO-PEG, we performed degradation analysis using HPLC. The time required for the drug degradation to be 50% of its original activity was ~68 and 96 hours for FD and SPIO-PEG-D, respectively, as shown in Figure 2-10A. The degree of Dox degradation increased for a longer incubation time at 37°C, resulting in a lower ability of crosslinking DNA. Degradation could be reduced when Dox was conjugated on the SPIO-PEG surface. The degree of freedom for Dox on SPIO-PEG was limited to significantly prevent it from molecular degradation, and therefore, its half-life of drug degradation was prolonged ~28 hours.

doi:10.6342/NTU201902917

DNA expression and cytotoxicity effect are related to the degree of DNA interstrand crosslink. The occurrence of interstrand crosslink was 31.3% after the treatment of FD with 7 μM for 24 hours, while it increased to 45.2% (1.4-fold) for SPIO-PEG-D with the same conditions (Figure 2-10B). The higher degree of interstrand crosslink was correlated to an increased cytotoxicity reducing DNA expression.

The cytotoxicity of FD, SPIO-PEG-D, and SPIO-PEG-D/MF to HT-29 cells was determined using the MTT assay. Figure 2-10C shows that both SPIO-PEG-D and SPIO-PEG-D/MF were toxic to HT-29 cells in a dose-dependent manner. The IC50 was 5.7 and 3.6 μM for SPIO-PEG-D and SPIO-PEG-D/MF, respectively. The IC50 value was significantly reduced to 3.6 μM for the SPIO-PEG-D/MF group, presumably because more SPIO-PEG-D were driven to the cells when a 0.4 T magnetic field was applied to enhance the local drug concentration. The IC50 of FD was 6.5 μM, higher than that of SPIO-PEG-D (5.7 μM), probably because SPIO-PEG-D could cause a more serious DNA crosslink than FD, resulting in a lower DNA expression and promoting apoptosis [69].

2.3.8. In vivo MR imaging and detection of iron

The short-term distribution of SPIO-PEG-D in mouse tumor tissues was assessed by T_2-weighted MR image before and after an injection of 18 mg Fe/kg, as shown in Figure 2-11A and B. Signal intensity in tumor decreased significantly after the injection of SPIO-PEG-D, indicating that the iron deposition in the tumor was locally increased. The in vivo MR image study also showed that the T_2-weighted signal of the SPIO-PEG-D/MF group was stronger than the SPIO-PEG-D group, indicating a better SPIO-PEG-D deposition in the tumor when a magnet was applied. The result demonstrated that a local magnetic field could help SPIO-PEG-D target the tumor and

doi:10.6342/NTU201902917

have a better retention over time. To validate the existence of SPIO-PEG-D in tumor tissues, microscopic images of Prussian blue-stained tissue slices were acquired, and the images revealed the presence of iron as shown in Figure 2-11C. The Prussian blue staining displayed that the SPIO-PEG-D/MF group had a much higher iron density in tumor tissues than the SPIO-PEG-D group. Figure 2-11C also shows confocal laser scanning microscopic images of Dox in tumor tissues after treatment with SPIO-PEG-D at 24 hours. In Figure 2-11C, the signals of red fluorescence present in the coronal plane of tumor tissue sections correspond to Dox. The confocal images showed that the SPIO-PEG-D/MF group had a much higher Dox accumulation in tumor tissues than the SPIO-PEG-D group. The spatial distributions of Dox and iron oxide nanoparticles in tumors may be able to provide the information of the dissociation of Dox from SPIO-PEG-D in tumor tissues. The results show that there is a mismatch distribution for Dox and iron depositions in tumor sections. This mismatch is probably able to indicate the dissociation of Dox from SPIO-PEG-D in tumor tissues. The TEM image of selected areas showed the internalized SPIO-PEG-D in tumor cells by endocytosis, as shown in Figure 2-11D. Prussian blue staining and TEM images of tumor slices demonstrated that SPIO-PEG-D was guided to and retained in the tumor by applying a magnetic field.

2.3.9. In vivo antitumor study

Figure 2-12A shows the in vivo antitumor efficiency of FD, SPIO-PEG-D, and SPIO-PEG-D/MF for the tumor-bearing mice. From day 7 after tumors were implanted, FD or SPIO-PEG-D solution was administered at a dose of 2.5 mg Dox/kg, seven times with a 3-day interval. The experimental results displayed that there were 992% and 455% of tumor volume change on day 52 for the SPIO-PEG-D and SPIO-PEG-D/MF groups, respectively. The significantly better inhibition of tumor growth for

doi:10.6342/NTU201902917

SPIO-PEG-D/MF can be attributed to the application of a magnetic field in the peritumoral region, enhancing the local concentration of SPIO-PEG-D [69]. The tumor volume change for the FD group on day 40 was larger than the SPIO-PEG-D group, probably due to the Dox stability on SPIO-PEG. The increased stability could maintain activity of Dox to have interaction with topoisomerase II to form DNA-cleavable complexes and produce cytocidal activity, and this prolonged stability could be crucial to extending the therapeutic effect in vivo [70]. Notably, the body weight of mice decreased significantly during the treatment period for the SPIO-PEG-D group as shown in Figure 2-12B, while there was no significant change for the SPIO-PEG-D/MF group. The results demonstrated that SPIO-PEG-D/MF can enhance the tumor treatment and reduce the drug toxicity to provide a safer nanodrug delivery.

Figure 2-12C shows the cell apoptosis of tumor, heart, and liver tissues on day 40 after HT-29 tumor implantation, obtained from the TUNEL analysis of tissue sections from the tumor-bearing mice treated with different therapeutics. There was a significantly greater amount of apoptotic cancer cells observed in the SPIO-PEG-D/MF group than in the SPIO-PEG-D group. This is because a higher deposition of SPIO-PEG-D in the tumor region can increase the cell-killing efficacy of Dox when the tumor is exposed to a magnetic field. Figure 2-12A and C confirms that the magnetization of SPIO-PEG-D was an important factor for the enhancement of chemotherapy under the application of a magnet. The images of apoptotic tissues showed that the highest amount of apoptosis in heart was for the FD group and the highest amount of apoptosis in liver was for the SPIO-PEG-D group, while the TUNEL images of tissues showed that the lowest amount of apoptosis in heart and liver tissues was for the SPIO-PEG-D/MF group, suggesting that this combined system could reduce both cardiotoxicity and hepatotoxicity. SPIONs have been used as a liver-specific MRI

doi:10.6342/NTU201902917

contrast agent for detecting hepatocellular carcinoma [71,72]. This technique relies on the ability of kupffer cells to uptake SPIONs. These particles (30–200 nm) were phagocytized by macrophages of the RES, accumulating in normal liver, spleen, and lymph nodes [73]. In the liver, these particles are sequestered by phagocytic Kupffer cells in normal RES [73]. In our studies, because the particle size of SPIO-PEG-D is ~85 nm, SPIO-PEG-D was easily phagocytized by macrophages of the RES and accumulated in normal liver and spleen. The highest accumulation of SPIO-PEG-D caused the highest amount of apoptosis in liver, and the lowest accumulation of SPIO-PEG-D/MF in liver tissues could cause the lowest amount of apoptosis. Therefore, a constant strength of magnetic field could be used to guide a significant quantity of SPIO-PEG-D to tumor region to increase the local drug concentration and to reduce the side effects.

Additionally, there are two primary routes of clearance of nanoparticles from body. One is the renal filtration with excretion into urine and the other is hepatobiliary (HB) processing with excretion into bile. Clearance of nanoparticles is determined by many factors, including particle size/shape, surface ligand, and surface charge density. Larger particles (>30 nm) are more easily trapped by liver and the RES. Lee et al [74] showed that there was no significant signal change in kidney for SPIONs (>30 nm), indicating that most intravenously injected SPIONs (>30 nm) are captured by liver and spleen, and the elimination of SPION by kidney is limited. Zhang et al [75] also demonstrated that the injected SPIONs with size of 86 nm cannot be metabolized through glomerular filtration. In their studies, the clearance route of 86 nm SPIONs was mainly HB processing with excretion into bile over a period of 14 days. Since SPIO-PEG-D is ~85 nm in our studies, SPIO-PEG-D is probably eliminated via HB processing with excretion into bile.

doi:10.6342/NTU201902917

2.4. Conclusion

In summary, COOH-PEG-triethoxysilane was synthesized, conjugated to the surface of SPIONs to form PEG-bound magnetic nanoparticles (SPIO-PEG), and then Dox was conjugated onto the SPIO-PEG surface to produce SPIO-PEG-D, a multifunctional magnetic nanoparticle. By applying a magnetic field, SPIO-PEG-D could be concentrated in the tumor region to increase the intratumoral concentration of Dox and reduce the drug toxicity for normal organs. Furthermore, the in vivo MRI study showed that there was a better signal contrast enhancement for SPIO-PEG obtained with applying a magnetic field. This multifunctional magnetic nanoparticle with high loading of drug, superparamagnetic property, and high magnetic relaxivities could become not only an effective delivery system for chemotherapeutic agents but also a great contrast agent for MR imaging. Magnetic enhancement delivery of SPIO-PEG-D was a promising targeting technique that could provide more effective cancer treatment and reduce potential side effects of drug.

doi:10.6342/NTU201902917

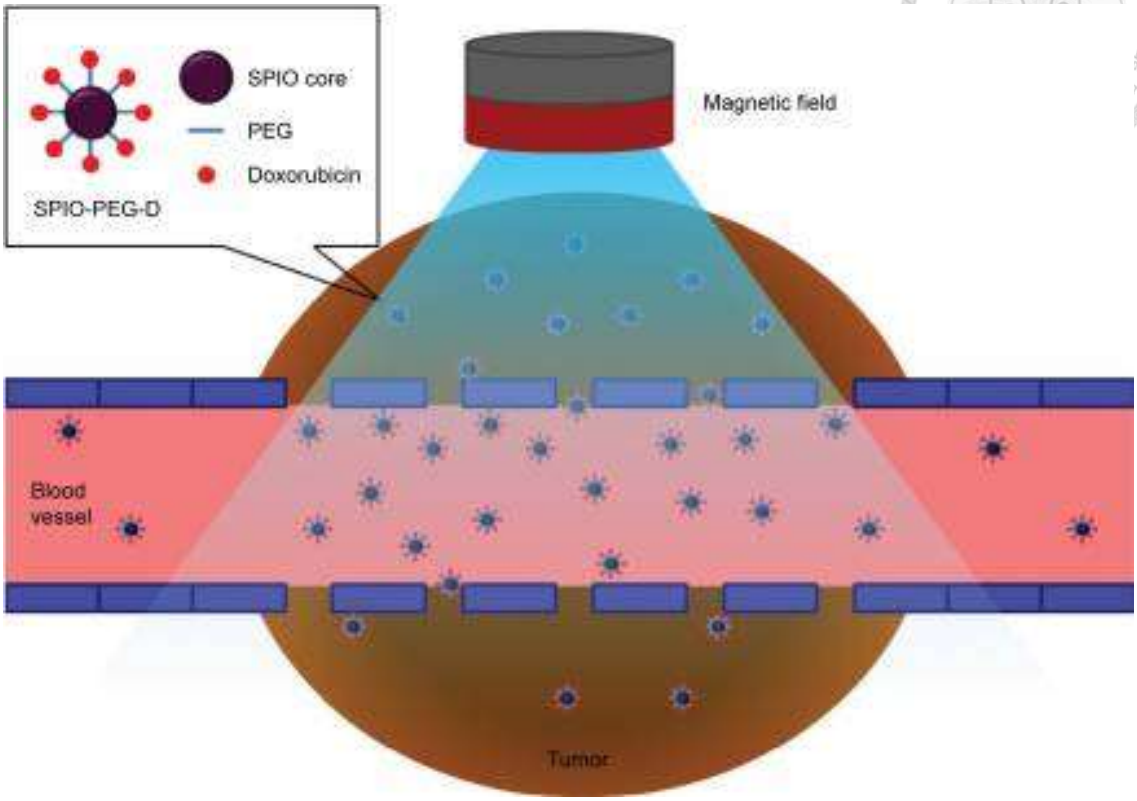

Figure 2-1. SPIO nanoparticles conjugated with PEG and then doxorubicin under a magnetic field during tumor treatment. Abbreviation: SPIO, superparamagnetic iron oxide; PEG, polyethylene glycol; SPIO-PEG-D, SPIO with PEG conjugated with doxorubicin.

doi:10.6342/NTU201902917

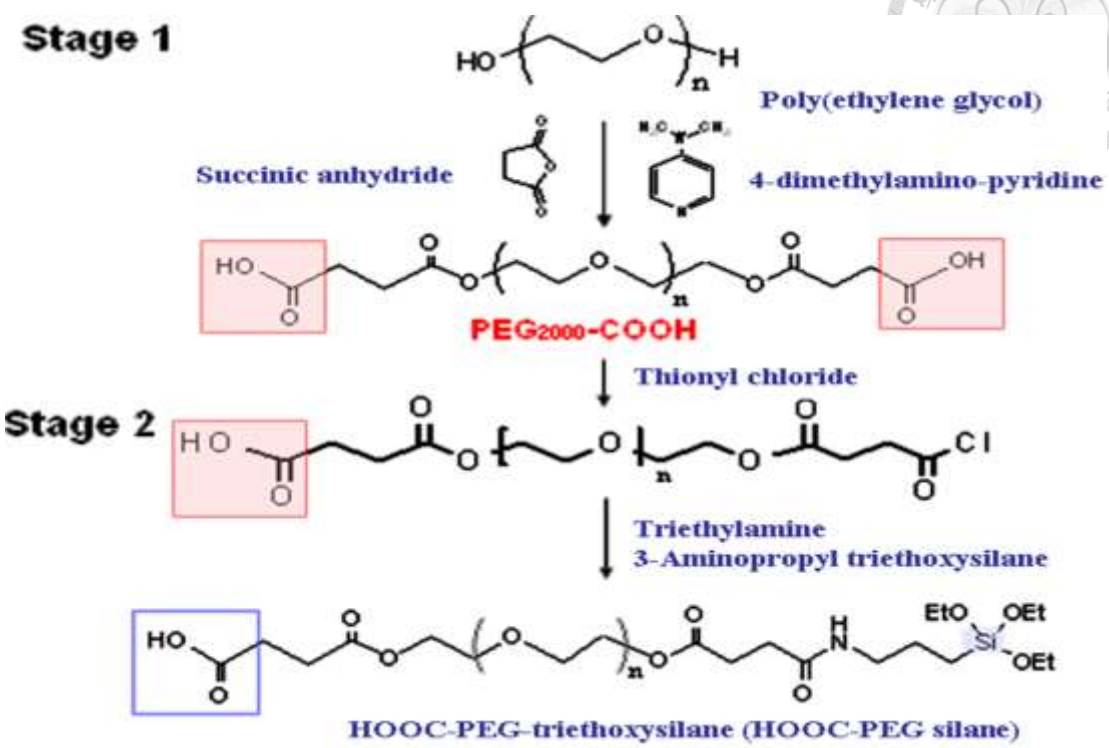

Figure 2-2. Synthetic route for HOOC-PEG silane. Abbreviation: PEG, polyethylene glycol.

doi:10.6342/NTU201902917

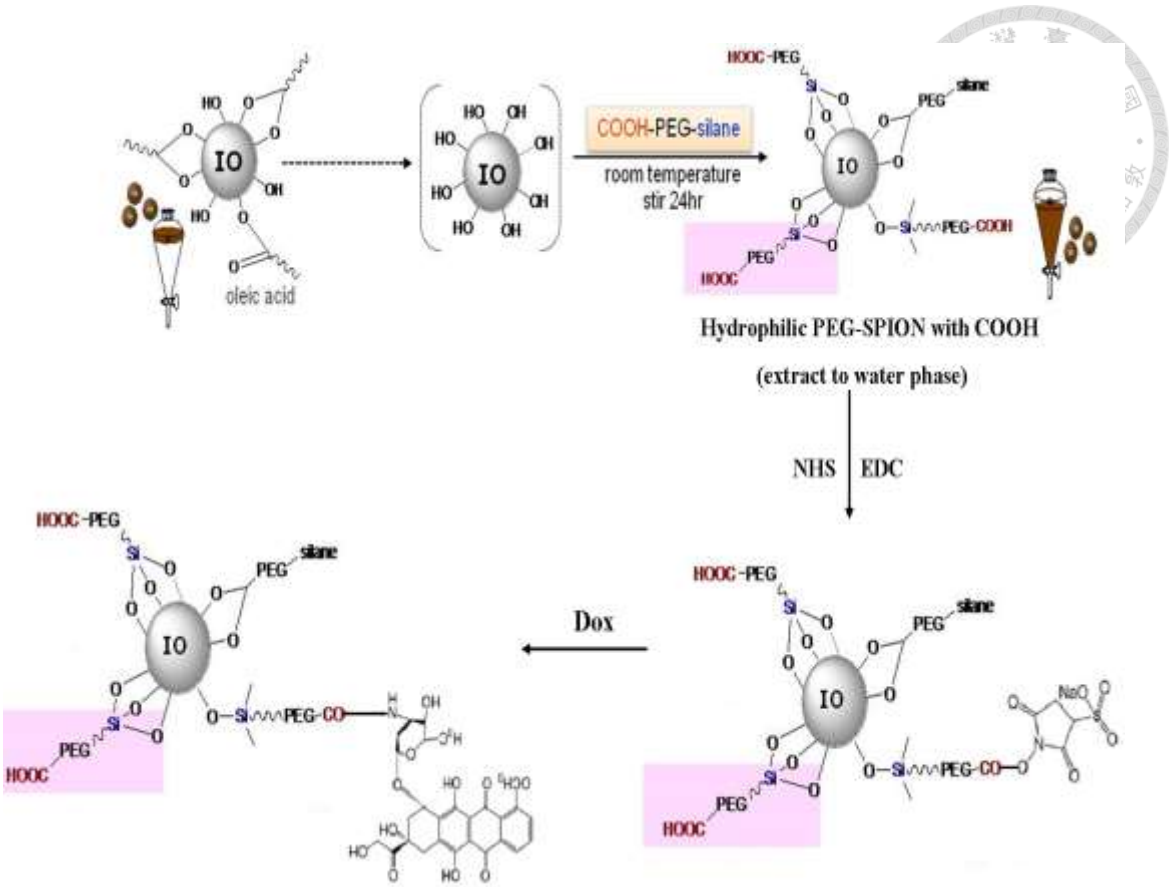

Figure 2-3. Synthetic route for SPIO-PEG-D. Abbreviation: PEG, polyethylene glycol; IO, oleic acid; PEG-SPION, PEG containing superparamagnetic iron oxide nanoparticle; SPIO-PEG-D, SPIO with PEG conjugated with doxorubicin; NHS, N-hydroxysulfosuccinimide; EDC, 1-ethyl-3-(3-(dimethylamino)-propyl)carbodiimide; Dox, doxorubicin.

doi:10.6342/NTU201902917

(A)

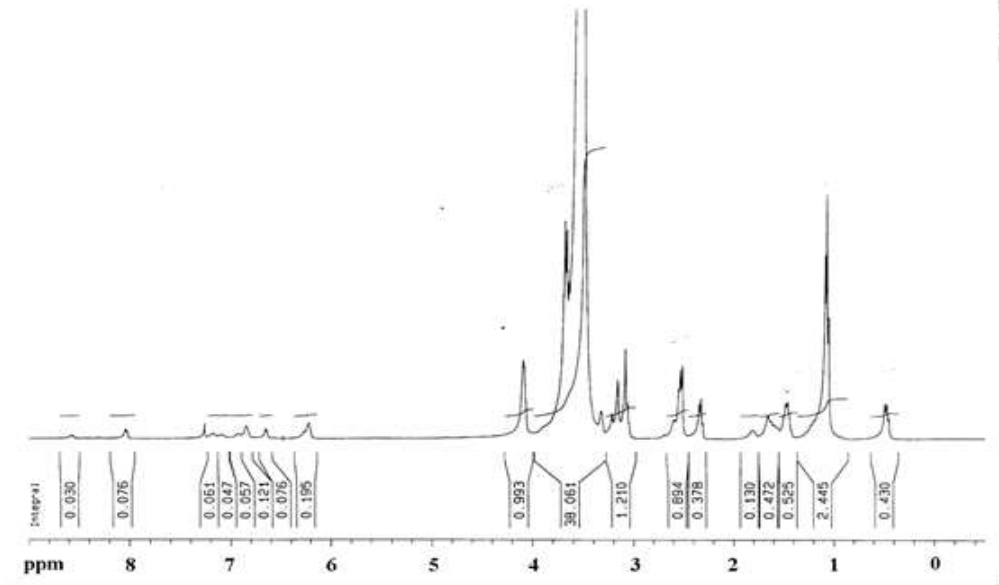

(B)

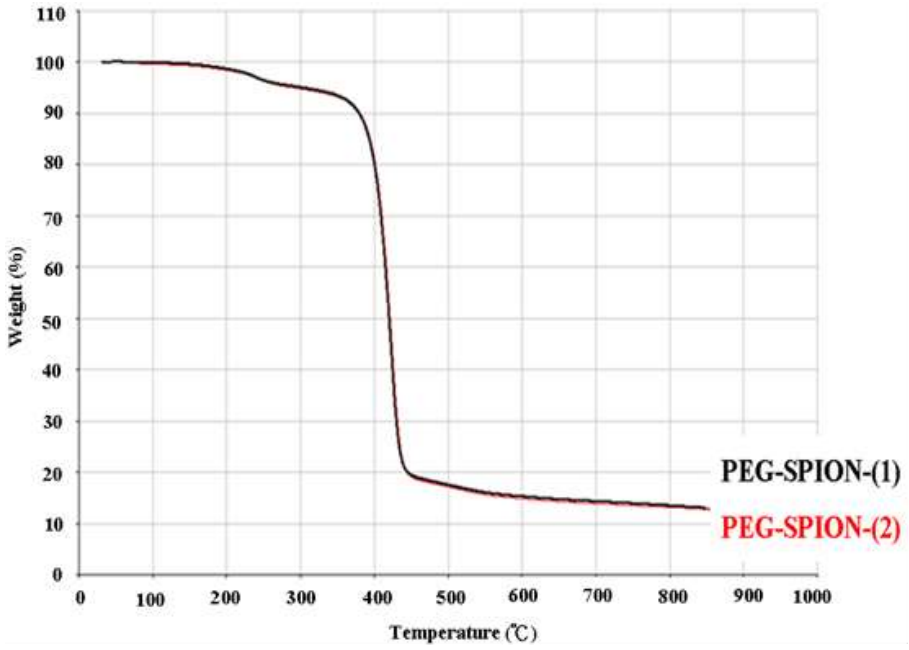

Figure 2-4. (A) 1H NMR spectra for HOOC-PEG silane. (B) TGA curves of the SPIO-PEG were tested twice. Abbreviation: PEG, polyethylene glycol; TGA, thermogravimetric analysis; SPIO-PEG,superparamagnetic iron oxide with PEG.

doi:10.6342/NTU201902917

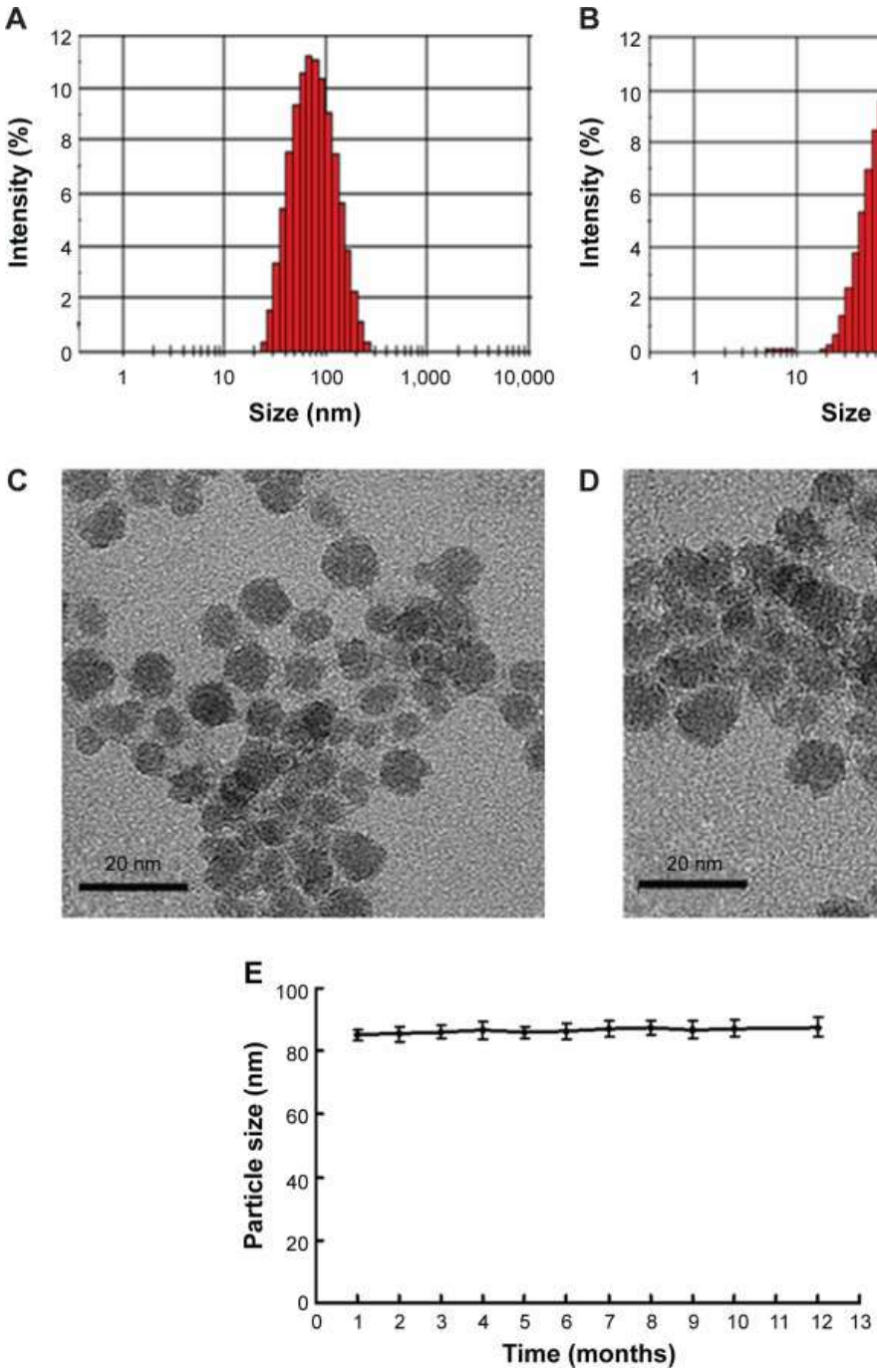

Figure 2-5. Particle size distribution and TEM images for (A and C) SPIO-PEG and (B and D) SPIO-PEG-D. (E) Stability curves of SPIO-PEG-D over 12 months (mean ± SD) (n=3). Abbreviation: TEM, transmission electron microscope; SPIO-PEG, superparamagnetic iron oxide with polyethylene glycol; SPIO-PEG-D, SPIO with PEG conjugated with doxorubicin; SD, standard deviation.

doi:10.6342/NTU201902917

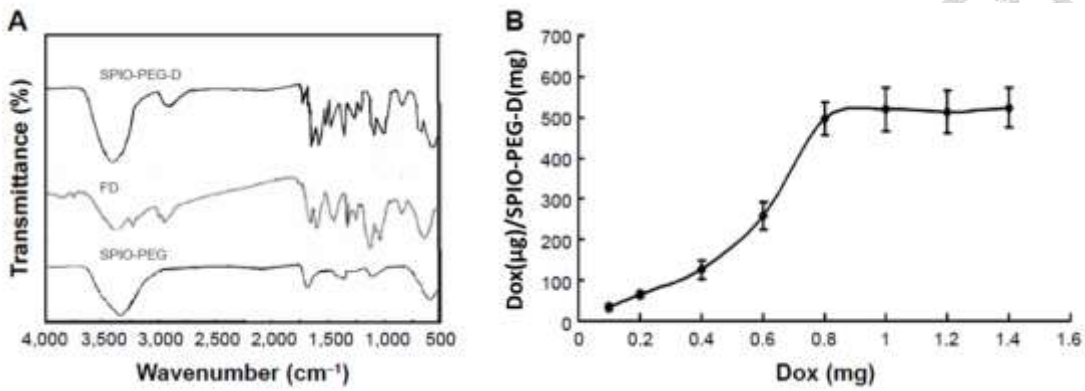

Figure 2-6. (A) FT-IR spectra for SPIO-PEG-D, Dox, and SPIO-PEG. (B) Quantity of Dox conjugate with SPIO-PEG. Abbreviation: FT-IR, Fourier transform infrared; SPIO-PEG-D, superparamagnetic iron oxide with polyethylene glycol conjugated with doxorubicin; Dox, doxorubicin; SPIO-PEG, SPIO with PEG; FD, free doxorubicin.

doi:10.6342/NTU201902917

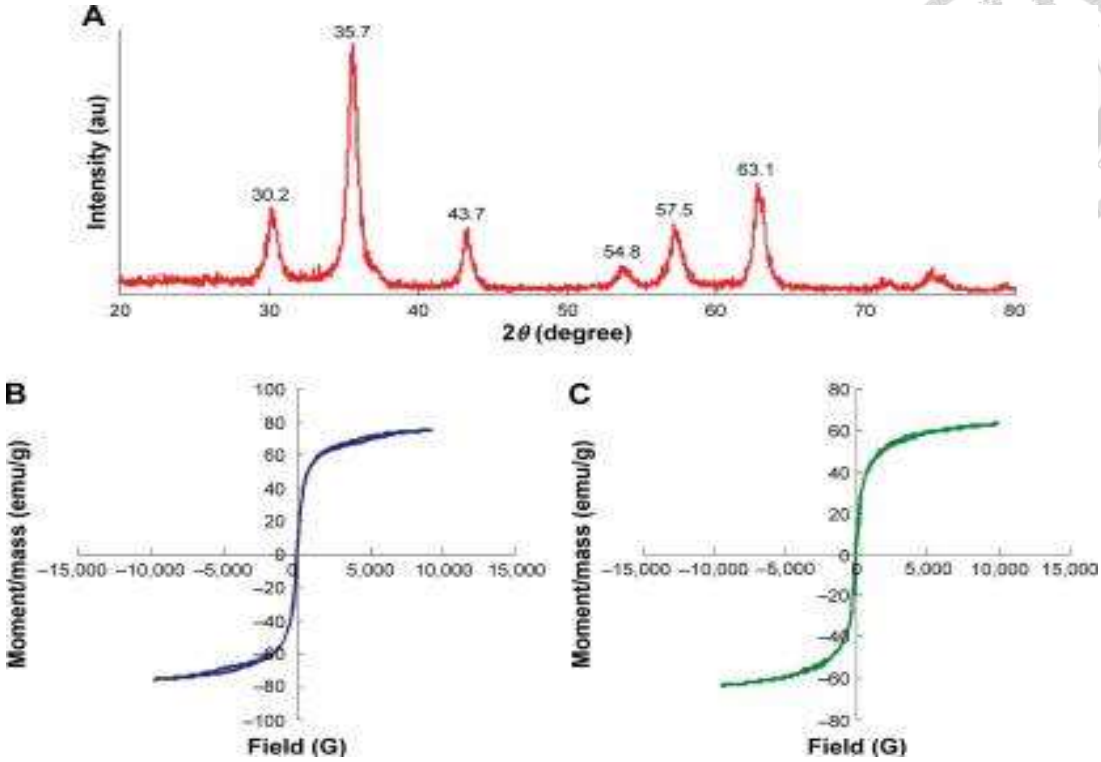

Figure 2-7. (A) X-ray powder diffraction pattern for SPIO-PEG-D, (B) variation of magnetization for SPIO-PEG, and (C) for SPIO-PEG-D as a function of applied magnetic field. Abbreviation: SPIO-PEG-D, superparamagnetic iron oxide with polyethylene glycol conjugated with doxorubicin; SPIO-PEG, SPIO with PEG.

doi:10.6342/NTU201902917

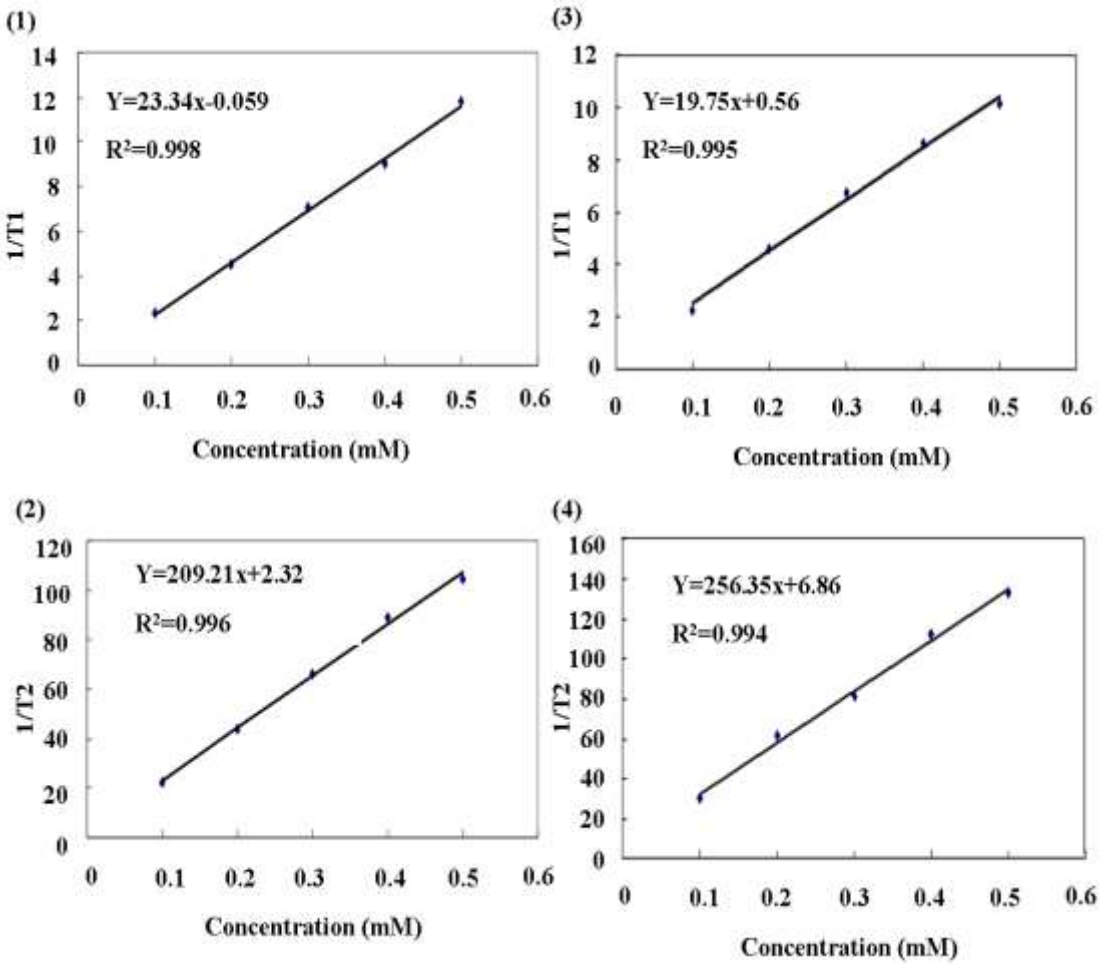

Figure 2-8. Relaxation response for (A and C) SPIO-PEG-D and (B and D) SPIO-PEG. Abbreviation: SPIO-PEG-D, superparamagnetic iron oxide with polyethylene glycol conjugated with doxorubicin; SPIO-PEG, SPIO with PEG.

doi:10.6342/NTU201902917

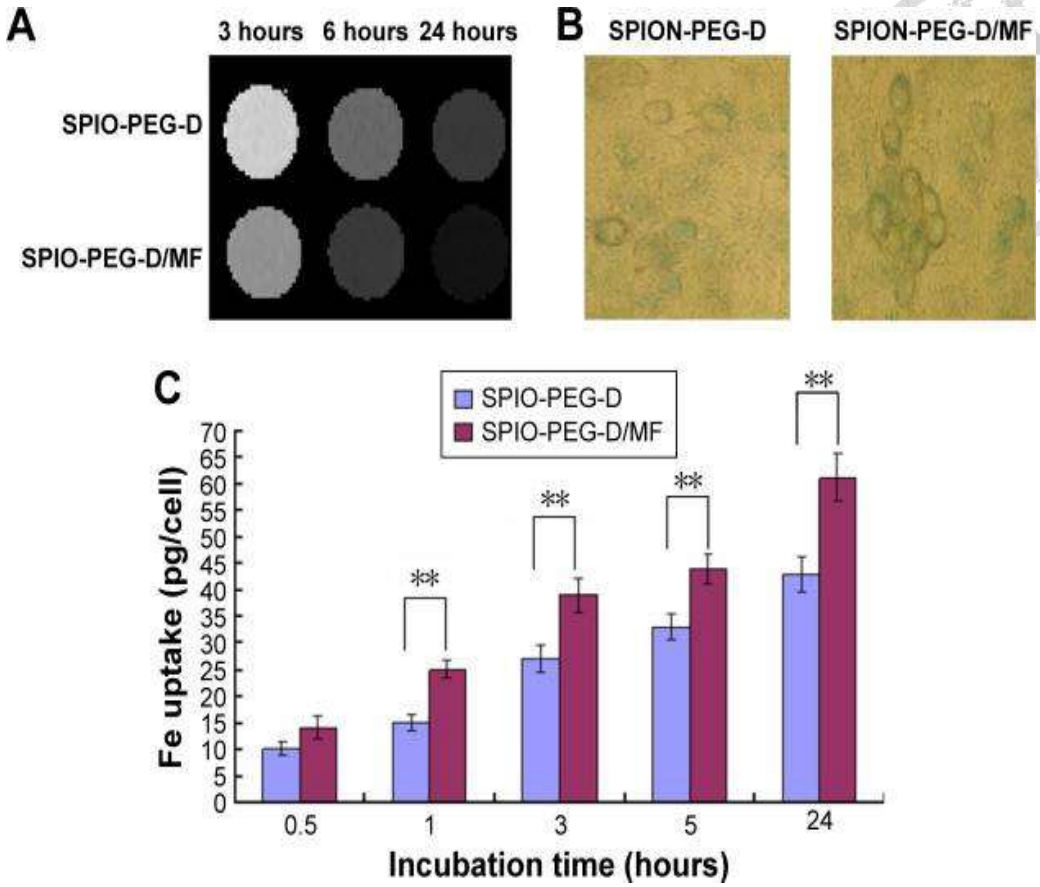

Figure 2-9. Cellular uptake of SPIO-PEG-D with or without magnetic field.

Notes: (A) T_2-weighted MR phantom images of HT-29 cells after incubation with SPIO-PEG-D or SPIO-PEG-D/MF for 3, 6, or 24 hours and (B) Prussian blue staining images of HT-29 cells after 24-hour treatment with SPIO-PEG-D and SPIO-PEG/MF. (C) The iron uptake in HT-29 cells treated with 100 μg Fe/mL of SPION-PEG-D after treatment with SPIO-PEG-D and SPIO-PEG/MF at different incubation time (mean ± SD) (n=5). **P<0.01. Abbreviation: MR, magnetic resonance; SPIO-PEG-D, superparamagnetic iron oxide with polyethylene glycol conjugated with doxorubicin; SPIO-PEG-D/MF, SPIO-PEG-D under magnetic field; SPIO-PEG/MF, SPIO-PEG under magnetic field; SPION-PEG-D, SPIO nanoparticle with PEG conjugated with doxorubicin; SD, standard deviation; SPION-PEG-D/MF, SPION-PEG-D under magnetic field.

doi:10.6342/NTU201902917

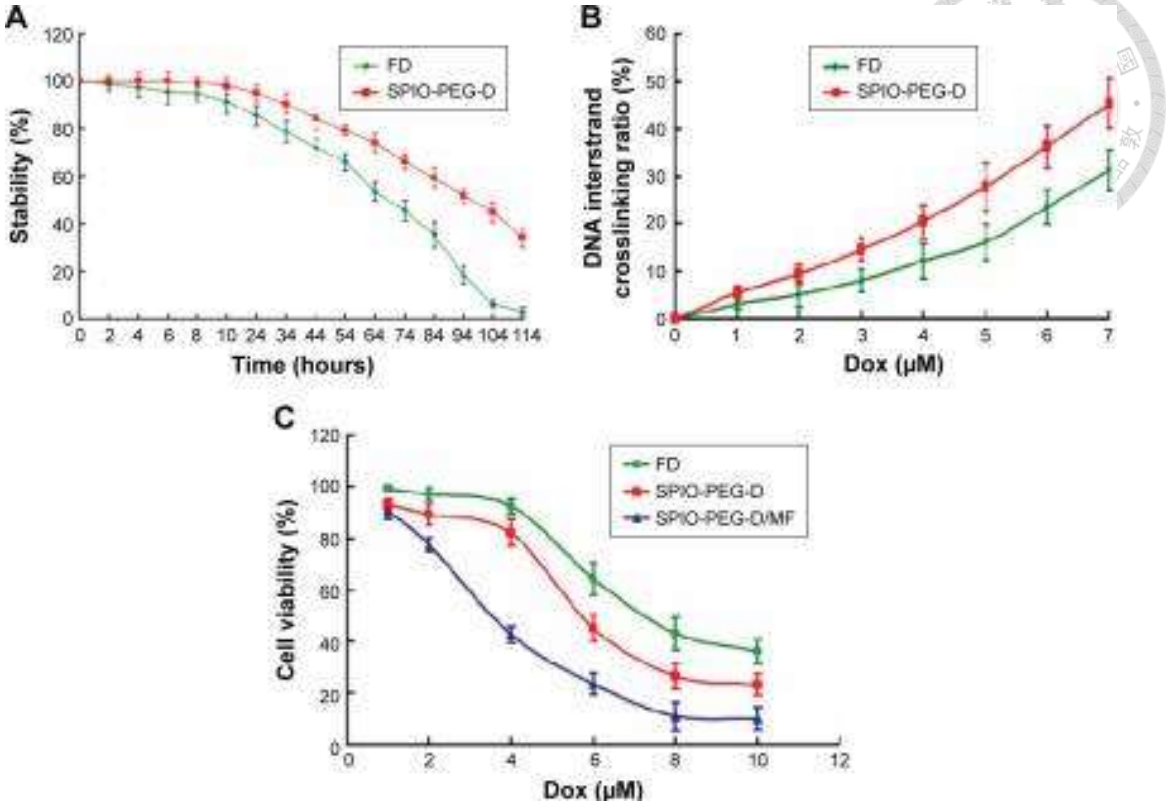

Figure 2-10. (A) Degradation curves of FD and SPIO-PEG-D over 114 hours. (B) DNA interstrand crosslinking in HT-29 cells after treatment with FD or SPIO-PEG-D for 24 hours. (C) Viability of HT-29 cells after incubation with FD, SPIO-PEG-D, or SPIO-PEG-D/MF (mean ± SD) (n=5). Abbreviation: FD, free doxorubicin; SPIO-PEG-D, superparamagnetic iron oxide with polyethylene glycol conjugated with doxorubicin; SPIO-PEG-D/MF, SPIO-PEG-D under magnetic field; SD, standard deviation.

doi:10.6342/NTU201902917

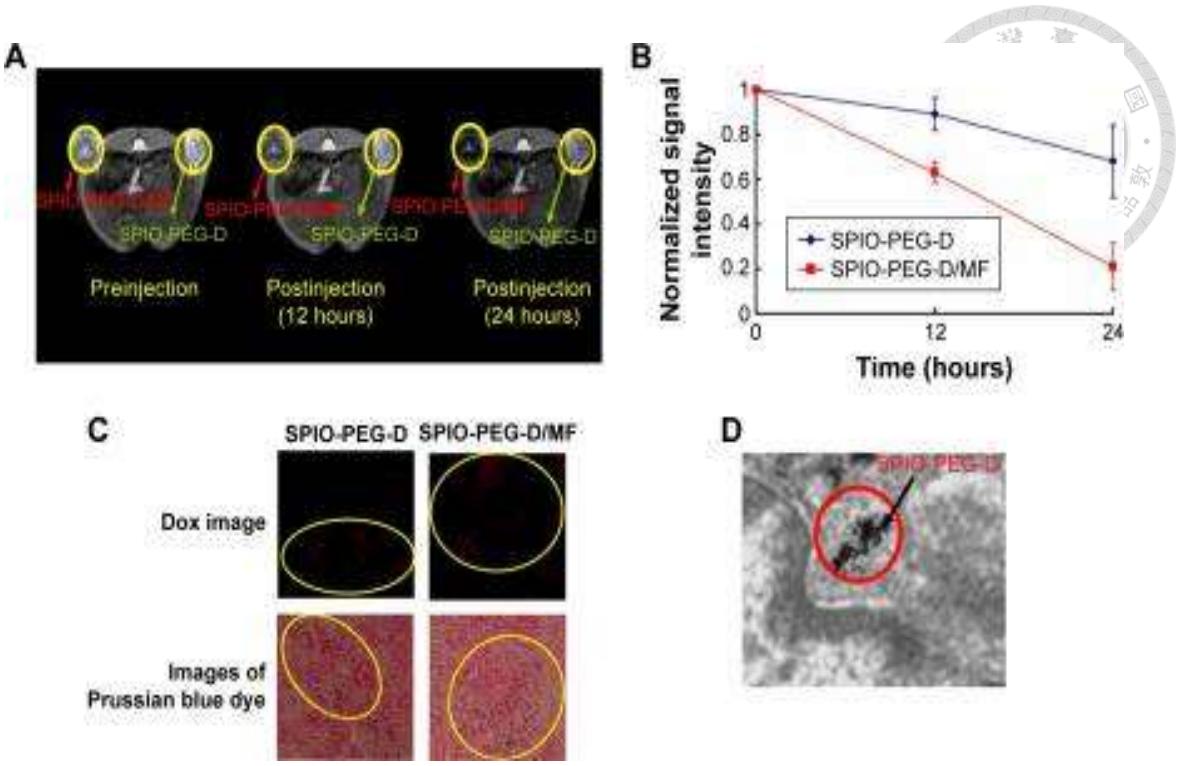

Figure 2-11. In vivo MR imaging and detection of SPIO-PEG-D.

Note: (A) T2-weighted MR images before and after treatment with SPIO-PEG-D (green arrows) or SPIO-PEG-D/MF (red arrows) and (B) MR signal intensity in mouse tumors (mean ± SD) (n=8). (C) Confocal laser scanning microscopic images of Dox in tumor tissues and microscope images of Prussian blue dye-stained tumor tissues after treatment with SPIO-PEG-D and SPIO-PEG-D/MF at 24 hours. Circled regions show the deposition of SPIO-PEG-D. (D) TEM image of tumor tissues after treatment with SPIO-PEG-D/MF. Black arrow indicates SPIO-PEG-D deposition. Abbreviation: MR, magnetic resonance; SPIO-PEG-D, superparamagnetic iron oxide with polyethylene glycol conjugated with doxorubicin; SPIO-PEG-D/MF, SPIO-PEG-D under magnetic field; SD, standard deviation; Dox, doxorubicin; TEM, transmission electron microscope.

doi:10.6342/NTU201902917

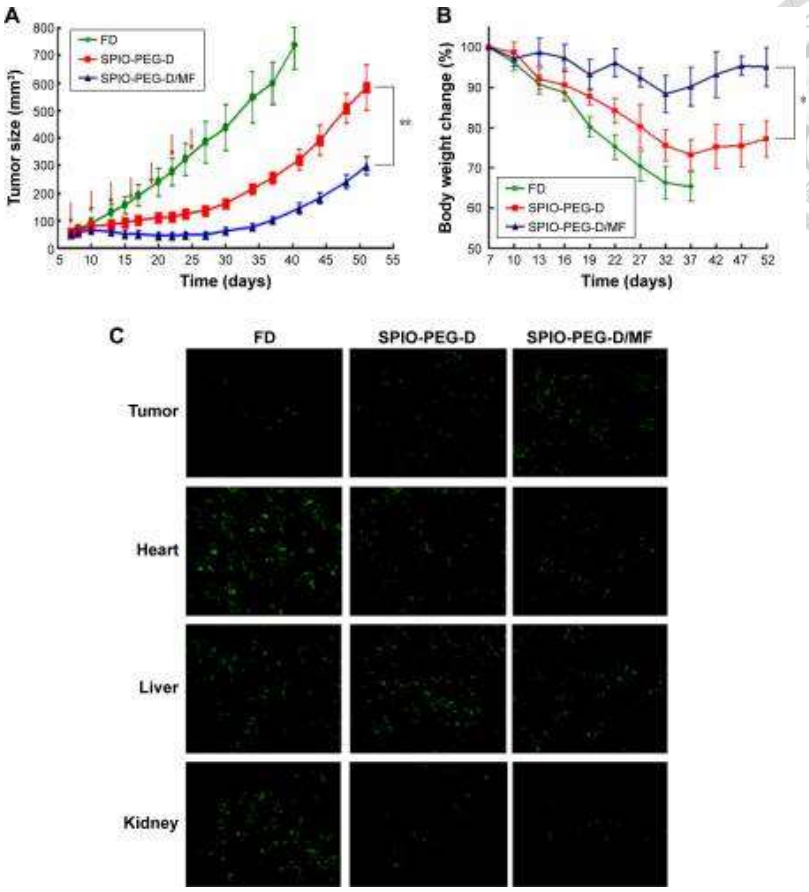

Figure 2-12. Tumor growth inhibition test of sc HT-29 xenografts in BALB/c nude mice.

Note: (A) Mice were IV injected with SPIO-PEG-D at a dose of 2.5 mg/kg Dox. The administration was carried out seven times with a 3-day interval (arrows: treatment days). (B) Body weight changes of the tumor-bearing mice. (C) TUNEL analysis of different tissue sections from the tumor-bearing mice treated with different therapeutics at a dose of 2.5 mg/kg Dox on day 40 after HT-29 cell implantation. The administration was carried out seven times with a 3-day interval. Green: apoptotic cells show green fluorescence (mean ± SD [n=4]. *P<0.05 and **P<0.01). Abbreviation: sc, subcutaneous; IV, intravenous; SPIO-PEG-D, superparamagnetic iron oxide with polyethylene glycol conjugated with doxorubicin; Dox, doxorubicin; TUNEL, terminal deoxynucleotidyl transferase dUTP nick-end labeling; SD, standard deviation; FD, free doxorubicin; SPIO-PEG-D/MF, SPIO-PEG-D under magnetic field.

doi:10.6342/NTU201902917

Table 2-1

Characterization of SPIO-PEG and SPIO-PEG-D (n=3)

Formulation	Hydrodynamic diameter (nm)	Polydispersity index	Zeta potential (mV)
SPIO-PEG	70±2.3	0.213±0.03	-14.2±0.4
SPIO-PEG-D	85±3.1	0.242±0.05	-1.8±0.2

SPIO-PEG: superparamagnetic iron oxide with polyethylene glycol.

SPIO-PEG-D: SPIO with PEG conjugated with doxorubicin.

doi:10.6342/NTU201902917

Chapter 3. (My study Part II)

Temperature/pH sensitive magnetic nanogel particles loaded with doxorubicin and conjugated with iRGD for enhancing colon cancer tumor chemotherapy and MR imaging

3.1. Introduction

Stimuli-sensitive drug carriers have attracted attention due to their response to external stimuli, such as temperature, pH, ultrasound, magnetic field, light, etc [76,77,78,79,80,81,82,83,84,85]. Compared with the conventional drug delivery system, carriers sensitive to multi-stimuli could deliver drug more effectively to the targeted site [86,87,88,89,90,91]. Temperature and pH-sensitive vehicles have been reported to meet the conditions of many diseased tissues with the change of their temperature and pH, and these two properties could also be regulated by external triggers [85,22,92].

Poly(ethylene glycol) (PEG) have been used to extend blood circulation time of nanoparticles. At a lower critical solute on temperature (LCST), some temperature-sensitive polymers had a transition property between hydrophilicity and hydrophobicity [93]. Therefore, it could be used for enhanced targeting of tissues by temperature variation [93]. For example, a temperature-sensitive polymer, poly(N-isopropylacrylamide) (PNIPAM), could increase the circulation times of drug carriers and reduce the adsorption of serum proteins in vivo below LCST [93]. The LCST of poly (NIPAM-co-AA) nanogel is above 37 °C. Therefore, these temperature/pH-sensitive nanogels have been used in local hyperthermia therapy for cancer treatment due to the increased deposition of drugs towards cancer cells and the decreased toxicity towards normal cells [94]. The studies also indicated that poly

doi:10.6342/NTU201902917

(NIPAM-co-AA) nanogels were hydrophilic under the physiological condition, whereas they became hydrophobic in an acidic environment and this property could improve cellular uptake of anticancer drugs [94].

In recent years, some bifunctional nanoparticles with both MR imaging and anticancer drug delivery have been developed for tumor diagnosis and therapy [48,95,96,97,98]. The development of multifunctional vehicles for the tumor-targeting delivery of both MR contrast agents and anticancer drugs would make cancer theranostics possible [33,35,36]. Nanocarriers containing tumor-targeting moiety, chemotherapy, and MRI contrast agent in one system can be useful drug delivery systems [48,47,49,50].

MRI is a powerful imaging modalities used in clinics and a higher MR sensitivity is required to more accurately diagnose and prognose early-staged cancer tumors. Superparamagnetic iron oxide nanoparticles (SPION) have magnetic properties to be an effective contrast agent for MRI to detect tumor tissues [48,95].

Doxorubicin (Dox) is one of the most effective anti-cancer drugs to treat many kinds of cancer [99]. However, its clinical use is limited by side effects, such as cytotoxicity and drug resistance. Novel drug carriers are used to reduce the toxicity and side-effects of anticancer drugs [51,67]. These drug carriers can effectively improve their blood circulation life-time, but cannot achieve the controlled release of the carried drugs accurately.

Arginine–glycine–aspartic acid (RGD) is a well-known peptide that is able to target tumor vasculature. RGD can specifically bind to integrin receptors in tumor endothelial cells [100]. The targeting ligand, RGD, has been used for delivering drugs, SPIONs, and drug carriers to tumors [101,102,103]. CRGDKGPDC peptide contains the RGD sequence and was named internalized RGD (iRGD) for its superior ability for binding

doi:10.6342/NTU201902917

on the cell surface at 4°C, while being internalized at body temperature (37°C) [104]. Furthermore, it is also able to penetrate tumor tissues deeply via binding to neuropilin-1 receptors expressed in tumor neo-vasculature and tumor cells [104]. iRGD was reported to enhance the vascular and tissue permeability in a tumor-specific and neuropilin-1-dependent manner, whereas conventional RGD peptides only help deliver the cargo to the tumor blood vessels [102]. The iRGD peptide targets tumor tissues through the RGD motif-mediates binding an integrin on tumor endothelium and a proteolytic cleavage then exposes a binding motif for neuropilin-1, which mediates penetration into tumor cells [102]. Thus, iRGD is highly effective in cancer therapy when combined with traditional drug delivery system.

In this study, a method used to develop temperature/pH sensitive magnetic nanogel particles (MNP-D) loaded with Dox and SPION was presented, and this MNP-D was conjugated with iRGD to be iMNP-D and be evaluated as a bifunctional nanomedicine for both cancer MR imaging and chemotherapy. iMNP-D was an efficient drug carrier which could achieve targeted and controlled release of therapeutic agent in tumor cells and could have enhanced MR signal to be detected in biological systems.

Figure 3-1 shows how the multifunctional magnetic nanogels can increase the drug delivery to the tumor and to have hyperthermia-induced drug release.

3.2. Methods and materials

3.2.1. Materials

1-Ethyl-3-(3-dimethylaminopropyl) carbodiimide hydrochloride (EDC-HCl), N-hydroxysulfosuccinimide (Sulfo-NHS), potassium persulfate (KPS) and sodium dodecyl sulfate (SDS), and Polyethylene glycol di-amine (MW=2000 kDa) were

doi:10.6342/NTU201902917

purchased from Sigma-Aldrich (St. Louis, USA). Iron(III) chloride and iron(II) chloride tetrahydrate were purchased from Merck. Oleic acid (OA), dichloromethane, isopropyl ether and toluene were purchased from Fisher Scientific. N,N'-methylene diacrylamide (MBA), acrylic acid (AA) and N-isopropylacrylamide (NIPAM) were purchased from Tokyo Chemical Industry Co., Ltd. (Tokyo, Japan). MBAm and NIPAM were recrystallized from methanol and n-hexane, respectively. iRGD (CRGDRCPDC) was purchased from Synpeptide Co., Ltd. (Shanghai, China). Doxorubicin HCl was obtained from Seedchem (Vic Melbourne, Australia).

3.2.2. Preparation of poly (ethylene glycol) di-acrylamide (PEGDA)

A solution of poly (ethylene glycol) diamine (0.0206 mol, 70 g) dissolved in dichloromethane (70 mL) was charged into a 250 mL round-bottom flask. The flask was flushed with N_2 for 30 min, then excess acryloyl chloride (4 molar excess to PEG diamine, 6.5 mL, 0.083 mol) and TEA (2 molar excess to poly (ethylene glycol) diamine, 5.7 mL, .0412 mol) were added. Then, the solution was stirred at room temperature for 2 h. After that, the mixture was filtered to remove triethylamine hydrochloride, and the fit rate was concentrated by a rotary evaporator to yield the colorless liquid compound poly (ethylene glycol) di-acrylamide [105].

3.2.3. Synthesis of magnetite nanoparticles with oleic acid (IO-OA)

Ferric chloride (30 mmol) and ferrous chloride tetrahydrate (15 mmol) were dissolved in water (50 mL). Sodium hydroxide solution (1N) was added to the solution until pH reached 12. Oleic acid (5 mL) was added to the solution and formed a black precipitate. The precipitate was centrifuged at 5000 rpm for 20 min and washed with water. Then, the pallet was re-dispersed in water. The solution was adjusted to pH 4

doi:10.6342/NTU201902917

using HCl (6 N). The mixture was centrifuged at 8000 rpm for 40 min and dried for 3 days. The solid was re-dispersed in toluene and centrifuged at 8000 rpm for 40 min to collect the supernatant. The supernatant was filtered through a 0.45 μm polytetrafluoroethylene (PTFE) filter, and collected as IO-OA nanoparticles [106].

3.2.4. Synthesis of magnetite nanoparticles with citric acid (IO-CA)

IO-OA nanoparticles were precipitated through the addition of a large excess of ethanol, separated via centrifugation (8000 rpm, 30 min), and dried in an oven to evaporate all alcohol. IO-OA nanoparticles (100 mg) were dispersed in a mixture solution (20 mL) of DCB and DMF (50/50). Then, citric acid (0.2 g) was added and stirred at 100 °C for one day. The IO-CA nanoparticles were precipitated by the addition of 50 mL of ethyl ether. The IO-CA nanoparticles were re-dispersed in acetone and dried at 70 °C for 24 h.

3.2.5. Synthesis of magnetic nanogel particles (MNP) and iRGD-conjugated MNP (iMNP), and loaded with doxorubicin (MNP-D or iMNP-D)

NIPAM (2.3 mmol), MBAm (0.13 mmol), SDS (0.04 mmol), and IO-CA nanoparticles (250 mg) were dissolved in water (50 mL). The solution was heated to 80 °C with stirring. KPS (0.04 mmol) was added and maintained at 80 °C. After 1 h, AA (0.33 mmol), poly (ethylene glycol) di-acrylamide (0.01 mmol) and KPS (0.012 mmol) were added for the free radical polymerization and maintained at 80 °C for 6 h. The magnetic nanogel particles (MNP) were dialyzed (molecular weight cutoff: 12,000-14,000 Da) for 3 weeks. Then, the dried MNP was obtained by lyophilization process and the Fe concentration of the purified MNP was determined by an ICP-mass spectrometer (Agilent ICP-MS 7500). MNP (2 mg of iron), EDC-HCl (4 mg) and

doi:10.6342/NTU201902917

Sulfo-NHS (8 mg) were mixed in 0.5 mL of a sodium acetate solution (1 M, pH 5.0) at 4 °C. After 1 h, the mixture was separated and the pellet was suspended in 0.5 mL of PBS (0.1 M, pH 7.4). 0.5 mL of iRGD (50 mg/mL) dissolved in PBS (0.1 M, pH 7.4) was added. After 24 h, the iRGD-conjugated MNP (iMNP) was collected after magnetic separation and washed 5 times with PBS to remove unreacted iRGD peptide. The iMNP was lyophilized and stored in PBS at 4 °C. The binding efficiency of iRGD to MNP was determined using a high performance liquid chromatography (HPLC) to analyze the amount of unconjugated iRGD. The value was compared to the total amount of added iRGD to analysis the binding efficiency of iRGD. For drug loading, iMNP (or MNP) (20 mg) and Dox (10 mg) were dispersed in PBS. The solution was stirred at 4°C for 5 days. The Dox loaded nanogel particles were separated from the solution using an external magnet. The solution was then analyzed using an ultraviolet-visible spectrofluorometer (Hitachi, Japan) to determine the amount of unencapsulated Dox. This value was compared to the total amount of added Dox to analysis the Dox-loading efficiency of the magnetic nanogel particles. Figure 3-2 shows the preparation of poly(AA-co-PEGDA-co-NIPAM) nanogel particles.

3.2.6. Characterizations of MNP-D and iMNP-D

The hydrodynamic diameters and Zeta potentials of MNP-D and iMNP-D were determined by dynamic laser light scattering (DLS, Malven Zetasizer 3000HSA, Worcs, UK). The sizes of MNP-D and iMNP-D were examined by the transmission electron microscopy (TEM, JEM-2010HR, Japan).

The crystal lattice properties of MNP-D and iMNP-D were determined by X-ray diffraction (XRD, Siemens D5000), and the magnetic properties were measured with vibrating-sample magnetometer (VSM) (Lakeshore, model 7300). The magnetization (M,

doi:10.6342/NTU201902917

emu g^{-1}) of MNP-D and iMNP-D was detected as a function of the magnetic field at 25℃. To determine the longitudinal (r_1) and transverse relaxivities (r_2) of the nanogel particles, the magnetic relaxation time (T_1, T_2) measurements of MNP-D and iMNP-D were carried out on a 0.47-T 20-MHz Bruker Minispec (Bruker Medical GmbH, Ettingen) at 37℃.

3.2.7. In vitro drug release

In vitro release of Dox from MNP-D and iMNP-D were investigated by dialysis method. MNP-D and iMNP-D were dispersed in water (5 mL) and introduced into dialysis bags (molecular weight cutoff: 3500 Da). Then, these bags were placed into buffer solution (50 mL) and stirred at 37 °C or 42 °C. The release solution (5 mL) was taken at different time intervals and replaced the media with fresh buffer solution (5 mL) every time. After that, the samples were analyzed using a UV-Vis spectrofluorometer (Hitachi, Japan) to analysis the concentration of Dox released into the dialysate. In addition, both pH 7.4 and pH 5.0 were chosen to evaluate the influence of different pH environment on Dox release.

3.2.8. MRI analysis of cellular internalization of MNP-D, iMNP-D, and i+iMNP-D

HT-29 human colon carcinoma cells (Bioresource Collection and Research Center, Taiwan) were grown in astrocyte medium. To assess the cellular internalization of MNP-D, iMNP-D, and i+iMNP-D with MR imaging, HT-29 cancer cells were grown in culture flasks at a density of 1×10^5 cells/mL. The experiments consisted of three groups: one treated with MNP-D, another treated with iMNP-D, and the other treated with i+iMNP-D). MNP-D or iMNP-D was added to every well at a concentration of 50 μg Fe/mL. The competitive effect was also studied by incubating the cells with excess free

doi:10.6342/NTU201902917

iRGD (200 μg/mL) for 1 h before incubating with iMNP-D (i+IMNP-D). After incubation for 3h, 6h, or 24h, the medium was removed, and the plates were washed five times with PBS buffer and then suspended in 300 μL of 0.5% agarose gel. Samples were then quickly transferred to a 96-well plate. MR imaging was performed with a 3.0-T whole-body MR scanner (MAGNETOM Trio, A Tim System 3T, Siemens, Erlangen, Germany).

3.2.9. Qualitative and quantitative studies of cellular uptake

Prussian blue staining was employed to analyze the cellular uptake of MNP-D, iMNP-D, and i+iMNP-D. The experiments consisted of three groups: one treated with MNP-D, another treated with iMNP-D, and the other treated with i+iMNP-D). The competitive effect was also studied by incubating the cells with excess free iRGD (200 μg/mL) for 1 h before incubating with iMNP-D (i+IMNP-D). HT-29 cancer cells were seeded in a chamber slide (1×10^5 per well) and incubated with DMEM and FCS (5%) containing MNP-D or iMNP-D at a concentration of 40 μg Fe/mL at 4°C for 24 h. Then, the HT-29 cancer cells were incubated at 37°C for 4 h and washed with PBS buffer solution. After that, the cells fixed with paraformaldehyde (3%) for 30 min and washed with PBS. The cells then incubated with potassium ferrocyanide (2%) in HCl (6%) for 40 min. After incubation, cells were washed with PBS buffer and observed under an inverted microscope for photo taking. To determine the cellular uptake, HT-29 cancer cells were seeded (1×10^5 per well) and were allowed to grow for 24 h. The competitive effect was also studied by incubating the cells with excess free iRGD (200 μg/mL) for 1 h before incubating with iMNP-D (i+IMNP-D). MNP-D or iMNP-D solution was added to every well at a concentration of 100 μg Fe/mL. After incubation, the medium was then removed, and the plates were washed with PBS buffer. The cells were trypsinized

doi:10.6342/NTU201902917

and counted using a hemocytometer. The cell suspension was centrifuged at 3000 rpm for 10 min. hydrochloric acid (2 mL) was added to pellet and the mixture was heated to 70°C for 10 min. After that, the samples were diluted with water and analyzed by an ICP-mass spectrometer (Agilent ICP-MS 7500).

3.2.10. Cell MTT cytotoxicity

MTT cytotoxicity tests were performed with MNP-D or iMNP-D. HT-29 cancer cells were seeded on a plate at a density of 1×10^5 cells/well in DMEM medium (100 μL) for 24 h. The medium was replaced with medium (100 μL) containing MNP-D or iMNP-D at the Dox concentration from 1 to 10 μM or nanogel particles without Dox loaded (MNP and iMNP) at the Fe concentration from 0.5 to 10 μM. The experiment consisted eight groups: MNP (37℃), iMNP (37℃), MNP (42℃), iMNP (42℃), MNP-D (37℃), iMNP-D (37℃), MNP-D (42℃), iMNP-D (42℃). After treatment, cells were incubated at 37℃ for 5 h. Then, 3-(4,5-dimethylthiazol-2-yl)-2,5-diphenyl tetrazolium bromide (5 mg/mL) was added and incubated for 5 h. The HT-29 cancer cells were lysed with dimethylsulfoxide (DMSO) (100 μL) and placed in an incubator at 37 ℃ for 24 h. The absorbance values of lysed cells were read using a microplate reader (model 680, BIO-RAD) at a wavelength of 490 nm.

3.2.11. In vivo MR image and detection of iron

Male BALB/c nude mice (6–8 weeks old) were obtained from the National Laboratory Animal Center (Taiwan). HT-29 cancer cells (5×10^6 cells/0.1 mL) were transplanted s.c. into the left flank region of mice. Seven days later, experiments were executed for two groups (n=5 for each group): one i.v. injected with MNP-D (15 mg

doi:10.6342/NTU201902917

Fe/kg), the other injected with iMNP-D (15 mg/kg Fe). All MR images were acquired on a 3T scanner (Trio with Tim, Siemens, Erlangen, Germany). The mice were anesthetized with isoflurane (2%) throughout the MRI process, placed in an acrylic holder and positioned in the center of the magnet. MRI images were quantified using T_2-weighted imaging with the following parameters: repetition time (TR): 4350 ms, echo time (TE): 95 ms, slice thickness: 1 mm, field of view (FoV): 50x85mm, bandwidth: 280 Hz/px, and resolution: 175x278, averages: 2, total scan time: 1 min 37 s. Then, the mice were euthanized by a lethal dose of pentobarbital and all of the tumors were harvested. The HT-29 tumors were fixed in neutral buffered formalin (10%), processed and paraffin embedded for the detection of iron expression by Prussian blue staining.

3.2.12. In vivo antitumor activity

6–8 weeks old of male BALB/c nude mice were obtained from the National Laboratory Animal Center (Taiwan). 1×10^5 cells/0.1 ml of HT-29 cancer cells were transplanted s.c. into the left flank region of mice. Seven days later, the tumor's size reached 200 mm^3 and the experiment was executed. The experiment included five groups (n=10 for each group, and the injected dose: 5 mg Dox/kg): FD (free Dox), MNP-D (37°C), iMNP-D (37°C), MNP-D (42°C), and iMNP-D (42°C). For hyperthermia groups, the tumor site was locally heated to 42 °C at 4 h after an intravenous injection of MNP-D or iMNP-D. It has been reported that a circulation time of about 4 h was ideal for nanoparticles accumulation in tumors through the EPR effect [107]. A near infrared laser (NIR) was used as a heat source. Four hours after nanogel particles injected, the tumor was exposed to NIR at a power intensity of 1.70 W/cm^2 (the temperature rise about 42 ˚C) for 3 min. The administration was carried out 5 times

doi:10.6342/NTU201902917

with a 3-day interval for hyperthermia groups. The tumor sizes and body weights of each group were measured and normalized to their initial values. The tumor size was calculated by $a \times b^2/2$, with a and b the largest and smallest diameter, respectively.

3.2.13. In vivo Dox accumulation

FD (free Dox), MNP-D, and iMNP-D solutions were injected via the tail vein for the mice bearing HT-29 cancer tumors. After four hours, the mice were sacrificed and the tumors were harvested and then quickly rinsed with saline to remove surface blood. The tumor tissues were homogenized with water, and then followed by an addition of 10 μL of daunomycin (10 μg/mL). The tumor tissues were extracted with 2 mL of chloroform/methanol (4/1, v/v) mixtures, and then intensely vortexing for 5 min. The samples were centrifuged (20000×g) for 30 min. The supernatant was collected and evaporated at 50 ℃. The residue was re-dissolved in methanol (300 μL) and analyzed with liquid chromatography. The separation assay of Dox was carried out by high performance liquid chromatography (HPLC), using a C18 column (5 μm, 4.6× 200mm, Diamonsil, Dikma). The mobile phase was a solution (70/30/0.3, v/v/v) of potassium dihydrogen phosphate, acetonitrile and glacial acetic acid. The mice were perfused with saline and paraformaldehyde about 4 h after the injection of nanogel particles. After NIR hyperthermia, tumors were removed and immersed in a fixative solution for 4 h. The tumor tissue was embedded in a Tissue-Tek optimum cutting temperature compound (Thermo Fischer Scientific, USA). In addition, the tumor tissues were sliced into 20 μm thick and dried on gelatin-coated microscopic slides. Then, the slides were rinsed and mounted using Dako Fluorescence Mounting Medium (Dako, USA). Finally, the tumor sections were imaged using a confocal microscope (FV1000, Olympus, Japan).

doi:10.6342/NTU201902917

3.2.14. Apoptosis detection for tumor cells

After treating, the mice were sacrificed on day 35 after tumor implantation. Then, the mice were perfused using trans-cardiac method with buffered formalin (10%). The tumor tissues were collected and fixed for at least 48 h. The apoptotic cells in tumor tissues were detected with TUNEL assays and observed using a confocal microscope (FV1000, Olympus, Japan).

3.3. Results and discussion

3.3.1. Characterization of poly(ethylene glycol) di-acrylamide and conjugation ratio of iRGD

Poly(ethylene glycol) di-acrylamide was identified by ^{1}H NMR analysis. Figure 3-3(1) shows 1H NMR spectrum of the compound displaying the secondary amine protons of amidic bonds (-CONH-) at 7.4 ppm, the protons of vinyl groups at 6.20~6.38 and 5.97~6.00 ppm, the methylene protons of ketone bonds (-CH_2CO-) at 4.23 ppm, the protons of poly(ethylene glycol) (-OCH_2CH_2-) at 3.55 ppm, and the methylene protons (-$NHCH_2$-) at 3.35 ppm. ^{1}H NMR (DMSO-d6, δH) ppm: 7.40 (4H, m, dH, gH), 6.20~6.38 (5H, t, jH), 5.97~6.00 (2H, q, iH), 4.23 (4H, t, bH), 3.55 (41H, m, aH), 3.35 (8H, s, eH, fH). The conjugation of iRGD to magnetic nanogel particles (MNP) was characterized with reverse phase HPLC. Figure 3-3(2) shows the HPLC chromatogram for iMNP and iRGD. The binding efficiency of iRGD to iMNP was 96%.

3.3.2. Characterization of MNP-D and iMNP-D

The average encapsulation efficiencies (EE) for Dox entrapment were approximately 85%, and the average EE for IO-CA entrapment was approximately 20% (Table 3-1). There is no difference in EE for the nanogel particles with or without the

doi:10.6342/NTU201902917

conjugation of iRGD. Dynamic light scattering (DLS) was used to determine the hydrodynamic particle size (Dh) and size distribution of small particles in suspension of nanogel solution. Figure 3-4 shows that the hydrodynamic particle sizes (D_h) are 97.1±2.4 nm, and 101.2±3.5 nm for MNP-D and iMNP-D, respectively. The polydispersity was less than 0.2 demonstrating that there was a narrow distribution of particle sizes (Table 3-1). The zeta potentials for the iMNP-D and MNP-D are -14.23±1.4 mV and -20.52±3.1 mV, respectively. Poly(AA-co-PEGDA-co-NIPAM) is an anionic polymer so that the zeta potential of iRGD conjugated nanoparticles was slightly more positive than the nanoparticles without iRGD modification (Table 3-1). To investigate the shape of MNP-D and iMNP-D, their morphology was visualized using transmission electron microscopy (TEM) as shown in Figure 3-4. The figure displayed the closely packed arrangement of IO-CA inside an organic layer indicating that IO-CA was successfully encapsulated in the nanogels with a particle size around 100 nm in diameter.

The magnetic properties of MNP-D and iMNP-D were evaluated by vibrating sample magnetometer (VSM) as shown in Figures 3-5(1) and 3-5(2). The magnetic moment was measured as a function of applied field at 298 K; the saturated magnetization value for iMNP-D and MNP-D was 80 and 83 emu/g, respectively. There is no significant difference in magnetization value between the nanogel particles with or without the conjugation of iRGD. Figures 3-5(3) and 3-5(4) show the dynamic thermogravimetric curves of iMNP-D and MNP-D, respectively. 5% of weight loss was attributed to the residual water and 75 % of weight loss between 250-650℃ was due to the degradation of organic components. 20% of residual weight after 650℃ was counted as the inorganic iron oxide ash. Figure 3-5(5), the powder X-ray diffraction (XRD) analysis of iMNP-D, shows detectable peaks at 30.2°, 35.5°, 43.9°, 54.8°, 57.6°,

doi:10.6342/NTU201902917

and 63.2°. These peaks are similar with Fe_3O_4 nanoparticles [52].

Iron oxide nanoparticles as a superparamagnetic contrast agent characteristically show a stronger T_2 effect with an r_2/r_1 ratio generally larger than 5, which permits a negative enhancement in MR imaging. Figure 3-6 showed the magnetic relaxivities, r_1 and r_2, were calculated as the slope of $1/T_1$ and $1/T_2$ versus iron concentrations. There is no difference in r_1 between iMNP-D and MNP-D (Fig. 3-6(1)). The r_2 value of iMNP-D (165 $Mm^{-1}S^{-1}$) was slightly smaller than that of MNP-D (188 $Mm^{-1}S^{-1}$) (Fig. 3-6(2)), as a result of the conjugation with iRGD that covers the nanogel particles and then slightly reduces the paramagnetic effect. The r_2/r_1 ratio is 15.6 and 15 for MNP-D and iMNP-D, respectively. The r_2/r_1 ratios for both MNP-D and iMNP-D were higher than Resovist® (r_2/r_1 ratio around 7), indicating that MNP-D and iMNP-D are more efficient than Resovist® [108].

3.3.3. In vitro Dox release

Figure 3-7 illustrates the temperature/pH-sensitive drug release profiles of MNP-D and iMNP-D. It is observed that about 60% of Dox was released from the nanogel particles at pH 5 and 37 °C within 72 h, but only about 40% of Dox was released at pH 7.4 over the same time (Fig. 3-7(1)). The acid-triggered Dox release behavior for the nanogel particles occurs because of Dox can be protonated at low pH resulting in an increase of drug solubility in aqueous solutions. Another reason causing the faster release of Dox at pH 5 might be due to this ion pair of Dox with acrylate will be lost due to protonation of the acrylate to acrylic acid at low pH. This pH-dependent release action was favorable for the antitumor drug delivery systems, since tumor cells were often at a lower pH environment, which would enhance a faster drug release in tumors than in normal tissues [109,110]. In addition, the poly(AA-co-PEGDA-co-NIPAM)

doi:10.6342/NTU201902917

nanogel particles serving as a drug carrier are expected to exhibit thermosensitive controlled-release character due to PNIPAM is a thermosensitive polymer. In order to verify this inference, MNP-D and iMNP-D were dialyzed in PBS (pH 5 and pH 7.4) at different temperatures. Figure 3-7(2) depicts the release profiles at different temperatures. The promoted drug release of MNP-D and iMNP-D in response to temperature increase was observed, particularly at pH 5. It is presumed that the thermo-evolved phase transition of PNIPAM at pH 5 and 42 °C could act as an efflux pump by inducing dehydration of nanogel assemblies to promote the concurrent out flow of water molecules with detached drug payloads. Based on the previous analysis, it was concluded that the developed iMNP-D with Dox release being dual-sensitive to temperature and pH could be able to distinguish between cancer cells and normal cells, achieving a better targeting efficiency and foreseeing an application to drug controlled-released systems.

3.3.4. In vitro qualitative and quantitative studies of cellular uptake

Figure 3-8(1) shows the T_2-weigthed MR phantom images of HT-29 cancer cells after incubation of MNP-D or iMNP-D. At a concentration of 50 μg Fe/mL, the rapid and efficient iRGD-targeting leads to a distinguishable darkening of MR images for the iMNP-D group, as compared to the MNP-D group. The result also showed that the iMNP-D group was a significantly higher cellular uptake than the MNP-D group, and this iRGD conjugated nanogel particles could produce a better MR monitoring and chemotherapy. In addition, the MR intensity of the i+iMNP-D group was comparable to that of the MNP-D group. This indicates that there was a competitive effect from the excess free iRGD, which reduced the binding sites available for iMNP-D, thus inhibiting the active receptor-mediated endocytosis process.

doi:10.6342/NTU201902917

The results of the iron concentration inside cancer cells were shown in Fig. 3-8(2). The iMNP-D group showed a significantly higher cellular uptake than the MNP-D group for HT-29 cancer cells. This was caused by the capability of iRGD conjugation to bind to HT-29 cancer cells, which have over-expressed integrin receptor, increasing the cellular internalization. In addition, the Fe concentrations inside HT-29 cells were found to increase along with incubation time for both MNP-D and iMNP-D groups. The uptake of iMNP-D was suppressed at all times when the cells were incubated with excess iRGD before the incubation with iMNP-D. It can be observed that the cellular uptake efficiency for the i+iRGD group was reduced to the level comparable with the MNP-D group. As a result, the inhibitory effect of the excess free iRGD confirmed that the uptake of iMNP-D is likely via receptor-mediated endocytosis, in accordance with the qualitative study as shown in Fig. 3-8(1) and Fig. 3-8(3). Prussian blue staining was performed to qualitatively assess the uptake of nanogel particles by HT-29 cancer cells, and the result was shown in Fig. 3-8(3). The result also indicated that the iMNP-D group had an enhanced cellular uptake of nanogel particles, shown as a higher Fe concentration, than the MNP-D group. This was caused by the capability of iRGD conjugated on MNP-D to bind to the HT-29 cancer cells to increase the cellular internalization via receptor-mediated endocytosis.

3.3.5. In vitro cytotoxicity of MNP-D and iMNP-D against HT-29 cancer cells

To investigate the potential toxicity of the nanogel particles and the pharmacological activity of Dox released from the nanogel particles, solutions of nanogel particle without Dox-loaded (MNP and iMNP) and nanogel particle with Dox-loaded (MNP-D and iMNP-D) were incubated with HT-29 cancer cells at different temperatures to examine their effects on cell viability. The MTT assay (Fig. 3-9(1))

doi:10.6342/NTU201902917

shows that, even at a high Fe concentration of 10 μg/mL, both MNP and iMNP have no significant cytotoxicity. In-vitro cytotoxicity of MNP-D and iMNP-D against HT-29 cancer cells is exhibited in Figure 3-9(2). It could be observed that the cytotoxicity of both MNP-D and iMNP-D had anticancer efficiency, implying that MNP and iMNP had virtually no toxicity to cancer cells. In addition, no significant difference in cell viability was found for MNP and iMNP at 37°C and at 42°C in Figure 3-9(1). This result indicated that the effect of a short time local heating was negligible. The data for the cell treated with iMNP-D exhibited a higher cytotoxicity as compared to the MNP-D group as shown in Fig. 3-9(2). This result suggested that iRGD can bind to the neuropilin-1 receptors and increases in cellular uptake via receptor-mediated endocytosis (RME) [111]. With the conjugation of iRGD, iMNP-D becomes a more potent drug carrier to deliver Dox against cancer cells. MNP-D or iMNP-D combined with a short time local heating (42°C) had a better antitumor activity than the group without (37°C), indicating the importance of Dox release from the carriers. The in-vitro drug-release study showed that the amount of Dox released from the heating groups (42°C, about 75%) was significantly higher than that from the no-heating groups (37°C, about 55%) as shown in Fig. 3-9(2). This finding indicated that the pharmaceutical effect of MNP-D or iMNP-D with a short time tumor heating (42°C) is more efficient since considerably more Dox was released and accumulated in the cancer tumors.

3.3.6. In vivo MR imaging and detection of iron

The distribution of MNP-D and iMNP-D in mouse tumor tissues was investigated by T_2-weighted MR imaging, as shown in Figures 3-10(1) and 3-10(2). Signal intensity in tumors decreased significantly after an injection of MNP-D or iMNP-D, indicating that the iron concentration was locally increased. The *in-vivo* MRI image also indicated

doi:10.6342/NTU201902917

that there was a stronger T_2-weighted signal for the iMNP-D group, indicating iMNP-D exhibited a higher iron accumulation in tumors as compared to the MNP-D group. These demonstrated that iRGD could help iMNP-D target the tumor tissues and have a better retention over time. To further validate the existence of iMNP-D in tumor tissues, microscope images of Prussian blue stained tissue slices were obtained and the images revealed the presence of iron as shown in Figures 3-10(3). The staining showed that the iMNP-D group had a much higher iron density in tumor tissues than the MNP-D group. Both Prussian blue staining and T_2-weighted MR image of tumor tissues confirmed that while circulating in the blood stream, iMNP-D would actively accumulate in the neovasculature tumor tissues via the cleaved sequence of iRGD by proteolysis. This would lead to the binding of neuropilin-1 receptors expressed by cancer cells and mediate the penetration of iMNP-D into cancer cells and tumor tissues.

3.3.7. In vivo antitumor activity

Figure 3-11(1) shows that tumor growth was more significantly suppressed for MNP-D (or iMNP-D) combined with a short time tumor heating than that with MNP-D (or iMNP-D) only. This finding reveals that the pharmaceutical effect of MNP-D (or iMNP-D) with a hyperthermic temperature heating (42℃) is more efficient than at body temperature (37℃) since considerably more Dox was released and accumulated in tumor cells. In addition, the iMNP-D group displayed a better treatment result than the MNP-D group for both with and without tumor heating conditions. This can be attributed to the iRGD targeting for the over-expressed neuropilin-1 receptors on tumor cells to increase the internalization of iMNP-D for HT-29 cancer cells. The group with iMNP-D and a short time tumor heating (42℃) was subject to the highest drug exposure

doi:10.6342/NTU201902917

for the tumors, and hence the best therapeutic effect was achieved [112]. The body weight of mice was also showed in Figure 3-11(2). There were no significant variations of the body weights for the mice treated with MNP-D or iMNP-D combined with or without a short time tumor heating, while the body weight of mice treated with free Dox decreased significantly. The results demonstrated that nanogel particles can reduce the anticancer drug toxicity to provide a safer delivery and have a greater kinetic stability.

3.3.8. Dox accumulation analysis for tumors

Figures 3-12(1) and 3-12(2) show the Dox concentrations and accumulation in tumor tissues for the tumor-bearing mice treated with FD, MNP-D (37℃), iMNP-D (37 ℃), MNP-D (42℃), or iMNP-D (42℃) at a dose of 5 mg Dox/kg. The signals of red fluorescence present in tumor tissue sections correspond to Dox. The results showed that the FD group had the weakest red fluorescence signal (the lowest Dox concentration) in tumor tissues, while the iMNP-D (42℃) group resulted in the strongest red fluorescence signal (the highest Dox concentration) in tumor tissues. For tumor-bearing mice receiving MNP-D or iMNP-D, a few fluorescence spots and a low Dox concentration in tumors were found at 37℃; however, as the local tumor temperature was elevated to 42 ℃, the strength of fluorescence signal and the Dox concentration in tumors increased. Confocal laser scanning microscopic images of tumor tissues and Dox concentrations illustrated that Dox was retained inside the nanogel particles at the body temperature; however, when heating was applied, a marked release of Dox occurred locally. That is, the combination of iMNP-D and a local short time tumor heating increased intratumoral anti-cancer drug concentrations. This finding demonstrated that iMNP-D (42℃) could overcome the delivery barriers and enhance drug release by

doi:10.6342/NTU201902917

temperature rise, resulting in the highest tumor retention and concentration of Dox.

3.3.9. Apoptosis detection for tumor cells

A greater amount of apoptotic tumor cells was found in the iMNP-D group than the MNP-D group, probably attributing to the increased intracellular delivery of iRGD into HT-29 cancer cells, as shown in Figure 3-13. In addition, a greater amount of apoptotic tumor cells was observed in the iMNP-D (42℃) group than in the iMNP-D (37℃) group. This is due to a short time tumor heating can enhance the Dox release from iMNP-D and increase its efficacy for the cancer cell killing. The images of heart tissues showed the highest amount of cell apoptosis for the free drug (FD) group. While, the apoptotic images of the iMNP-D groups (37℃ and 42℃) showed the lowest amount of cell apoptosis in heart, suggesting that Dox-caused cardiomyopathy may be reduced by treating iRGD-conjugated MNP-D. Therefore, iRGD could be used to increase the local concentration of anticancer drug in tumors and reduce the side effect of drug in heart. These results also confirmed that the combination of iMNP-D with a short time tumor heating was one of the important factors to enhance drug release and accumulation in tumors for chemotherapy.

3.4. Conclusion

We had prepared a temperature/pH-sensitive iMNP-D and utilized it as a MR-monitoring drug delivery system. The experimental results have demonstrated that iMNP-D has a great potential for providing an enhanced cellular uptake and drug release with a short-time tumor heating and significantly improving drug accumulation in the treated tumors. The highly tumor-penetrating cancer cell-targeting and temperature/pH-sensitive properties of the iMNP-D contribute the efforts to establishing

doi:10.6342/NTU201902917

an effective tumor-selective and controlled release chemotherapy. iMNP-D can reduce the toxicity and side effects of Dox and improve tumor targeting delivery. Furthermore, the *in-vivo* MRI study showed a better contrast enhancement of signals for iMNP-D, indicating iMNP-D could not only be an effective carrier of chemotherapeutic agent but also be an excellent contrast agent for MR monitoring. Hence, iMNP-D might have a great potential for the application of MR monitoring and drug controlled release chemotherapy in the treatment of cancer tumors.

doi:10.6342/NTU201902917

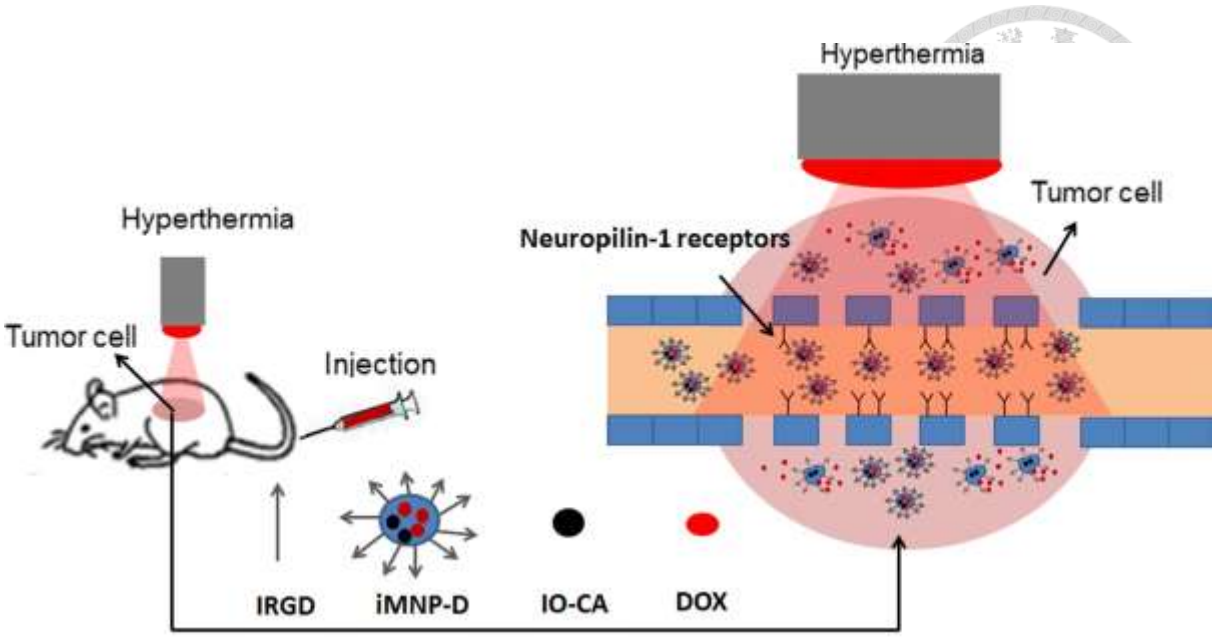

Figure 3-1. Schematic illustration of hyperthermia-induced DOX release from iMNP-D.

doi:10.6342/NTU201902917

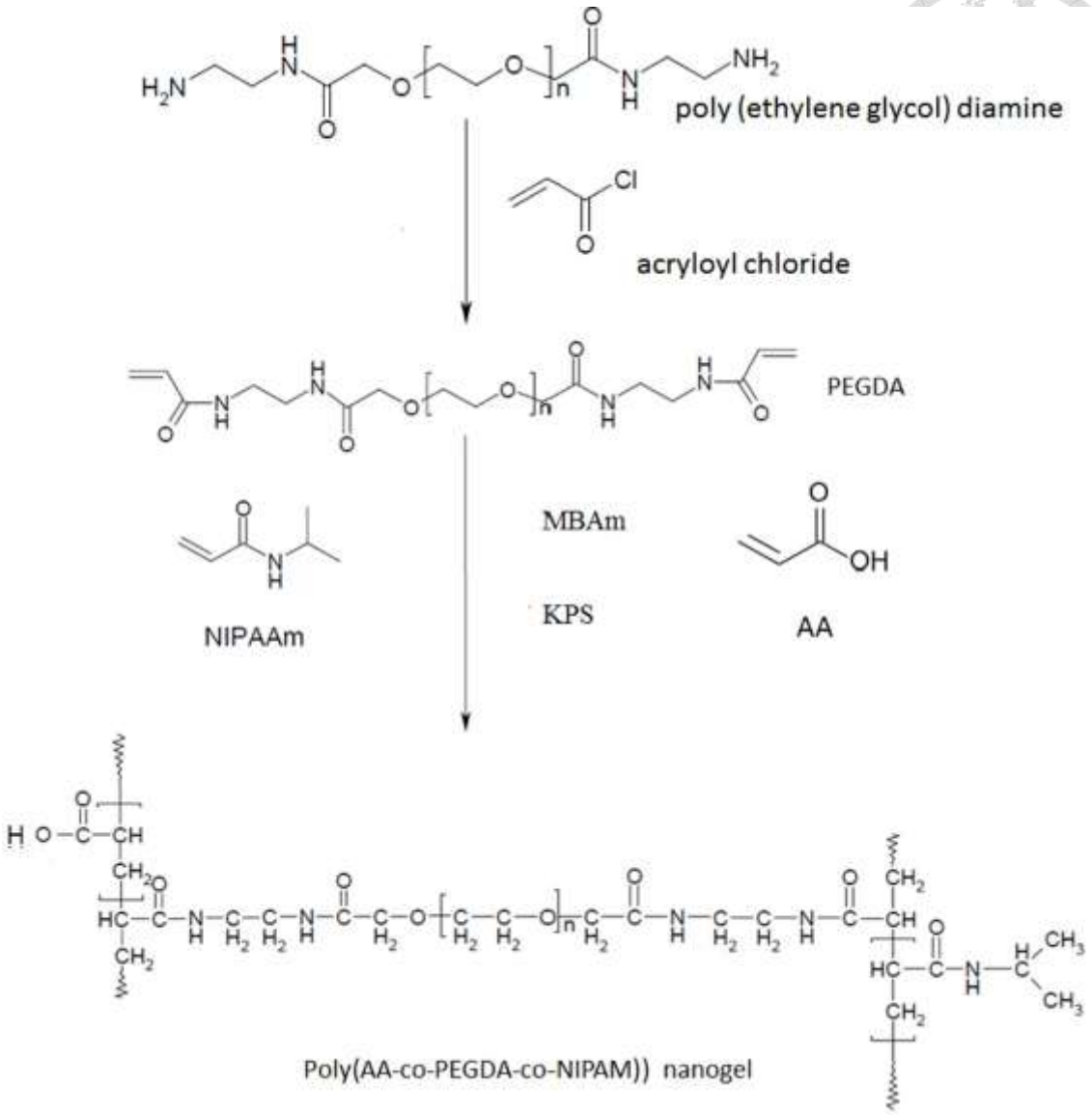

Figure 3-2. Preparation of poly(AA-co-PEGDA-co-NIPAM) nanogels.

doi:10.6342/NTU201902917

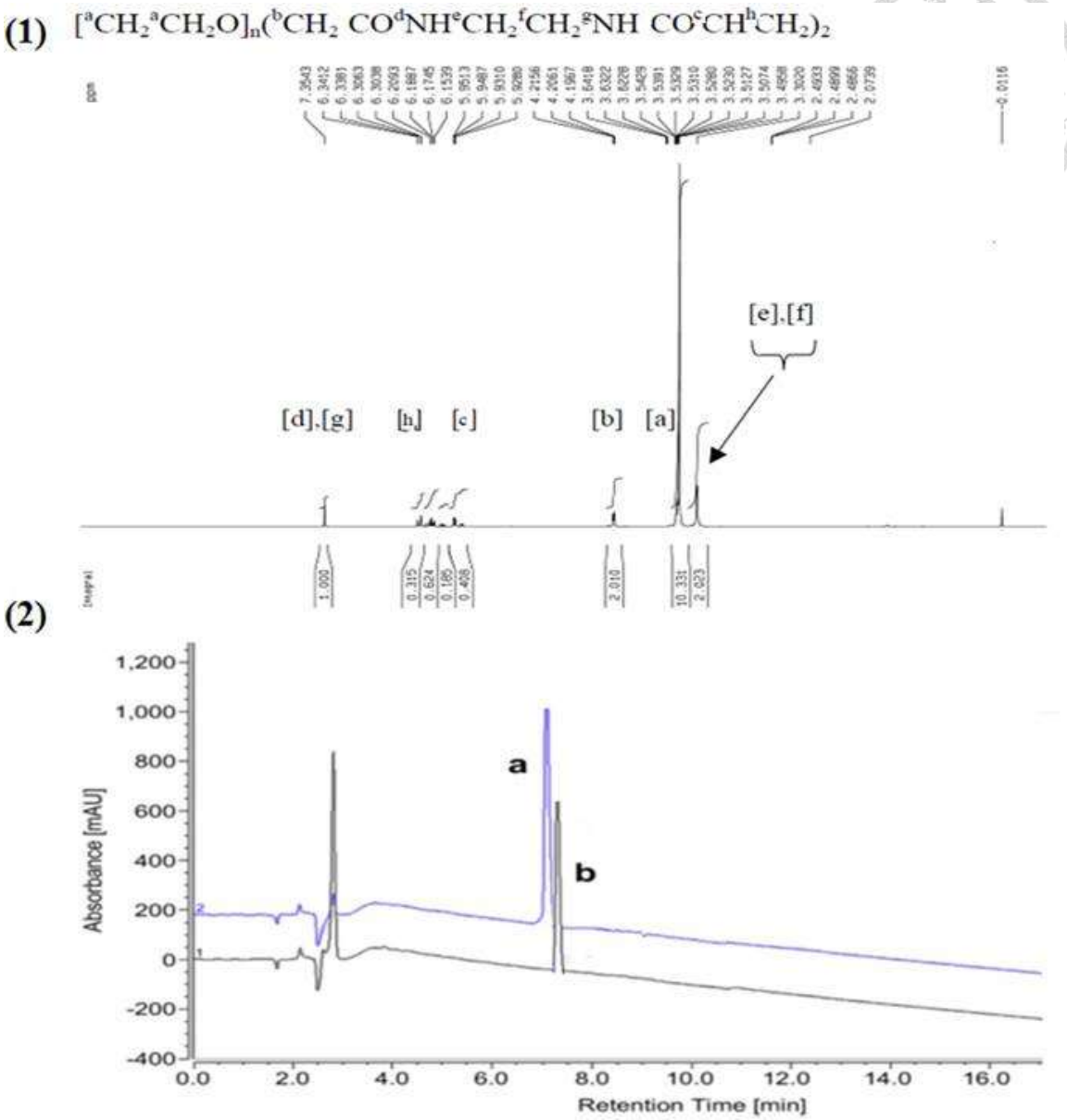

Figure 3-3. (1) 1H NMR spectra of poly (ethylene glycol) di-acrylamide and

(2) HPLC chromatogram for (a) added iRGD and (b) unconjugated iRGD.

doi:10.6342/NTU201902917

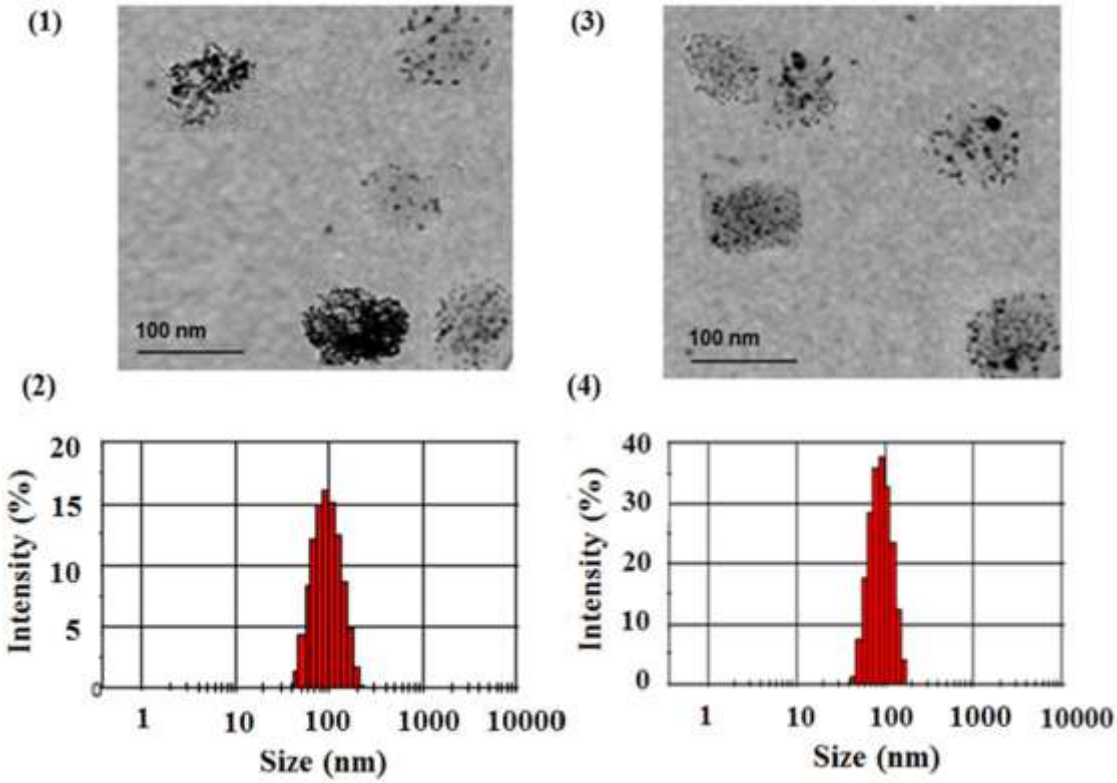

Figure 3-4. TEM images and DLS graphs for iMNP-D (1 and 2), MNP-D (3 and 4)

doi:10.6342/NTU201902917

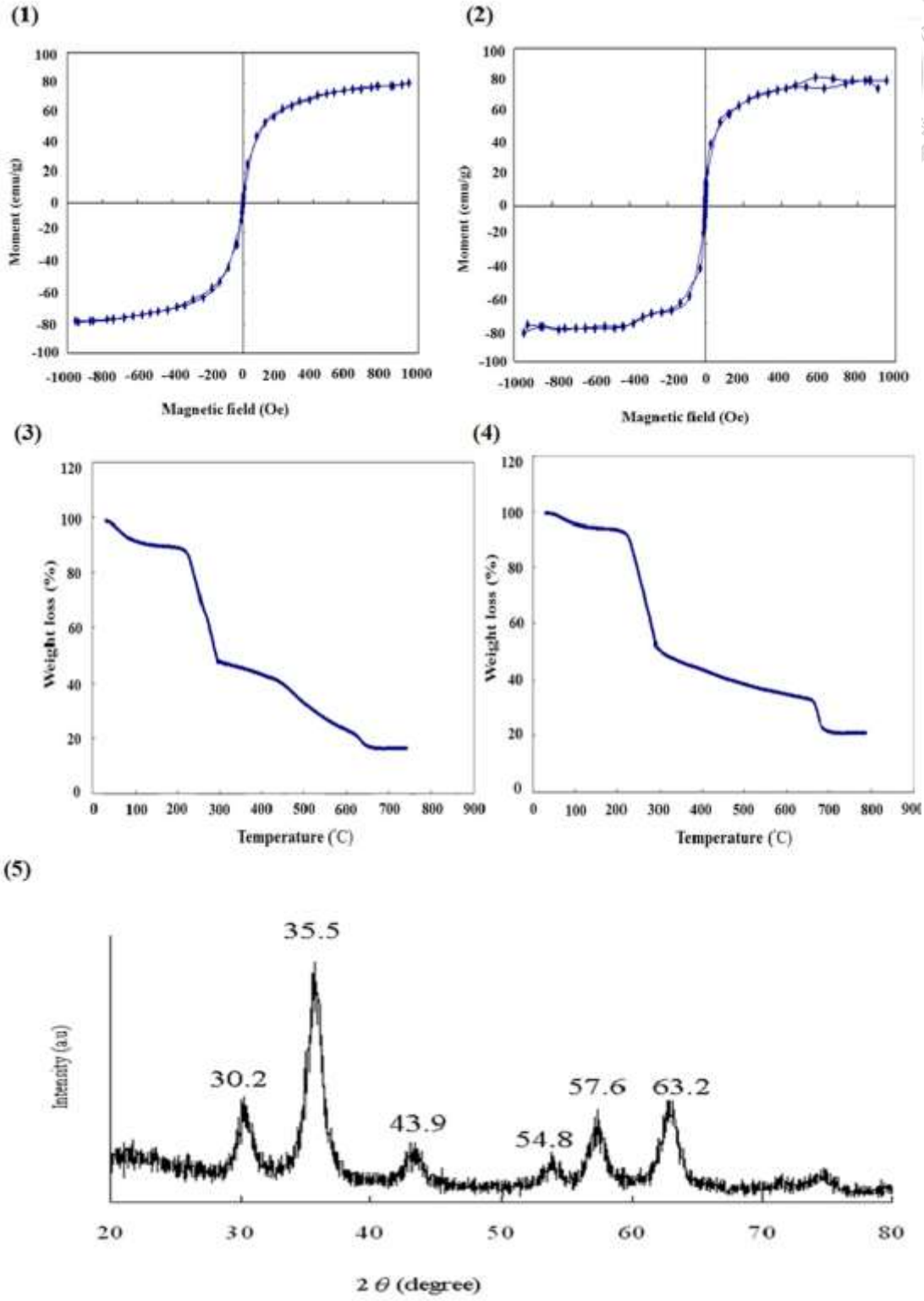

Figure 3-5. (1) Variation of magnetization for iMNP-D and (2) for MNP-D as a function of applied magnetic field. (3) TGA curves of the iMNP-D and (4) MNP-D. (5) X-ray powder diffraction pattern for iMNP-D.

doi:10.6342/NTU201902917

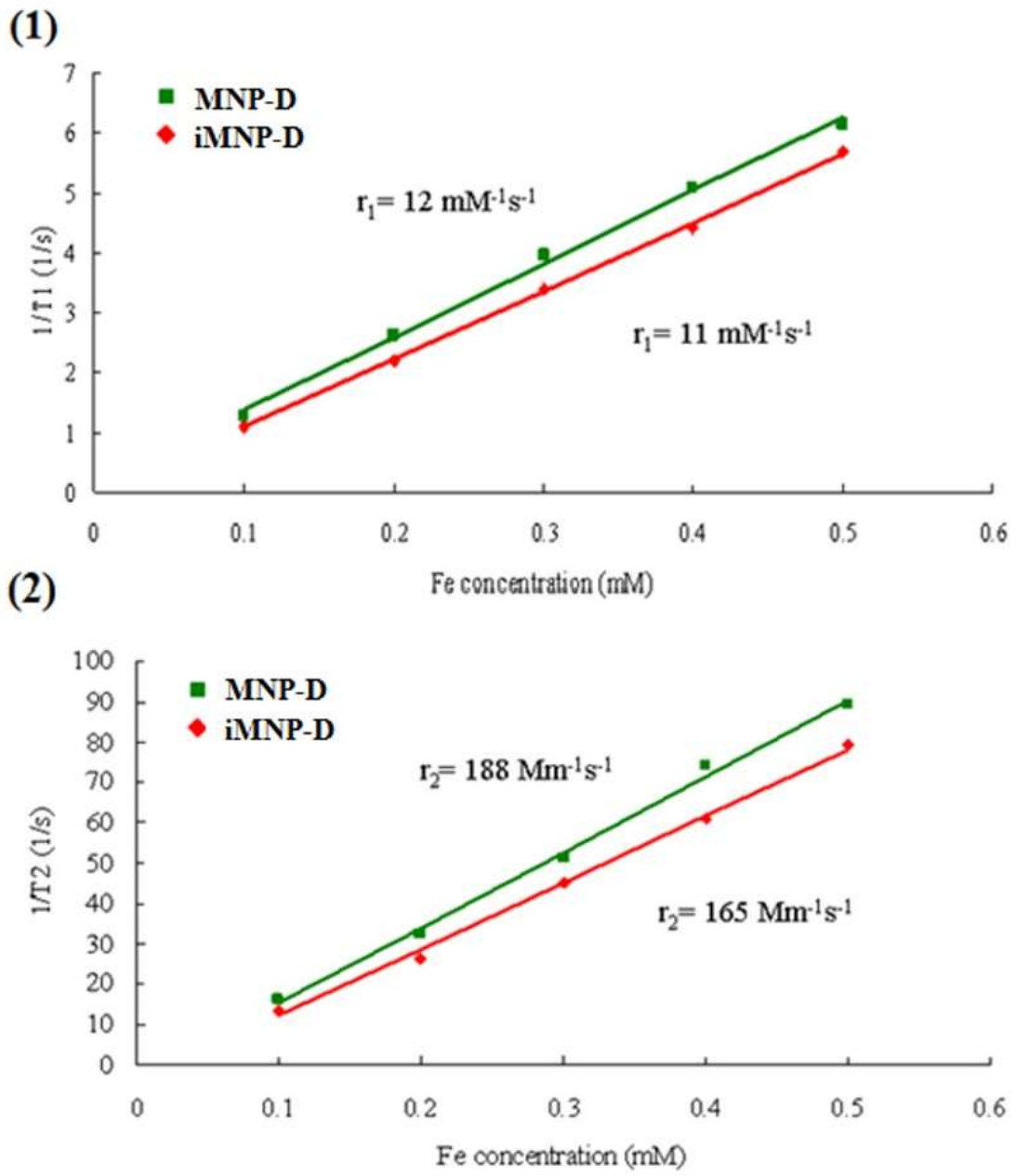

Figure 3-6. (1) Relaxation response (r_1) for iMNP-D and MNP-D, and (2) relaxation response (r_2) for iMNP-D and MNP-D.

doi:10.6342/NTU201902917

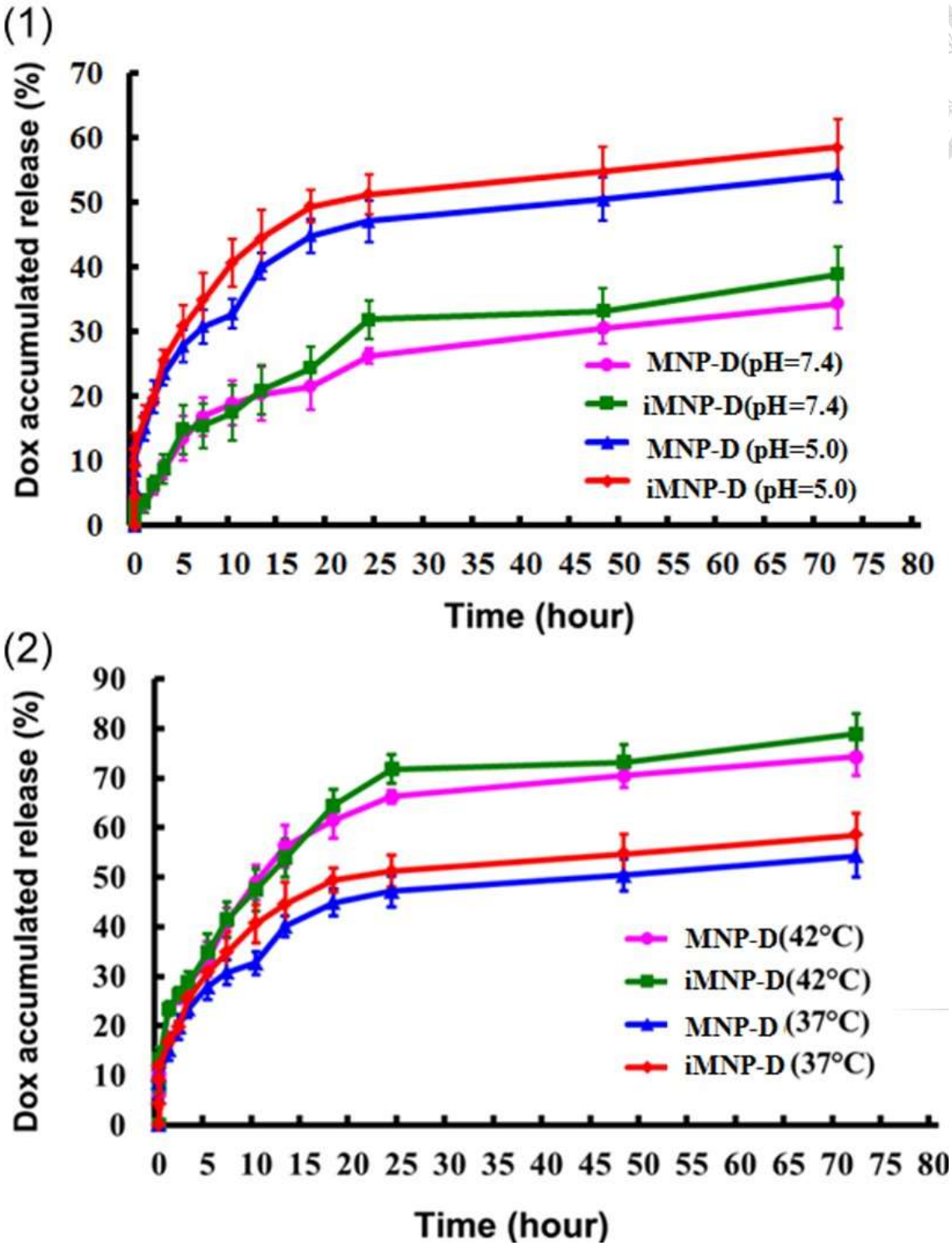

Figure 3-7. (1) In-vitro Dox release profiles for two nanogels, MNP-D and iMNP-D at neutral (pH 7.4) and acidic (pH 5.0) conditions at 37℃. (2) In-vitro Dox release profiles for two nanogels, MNP-D and iMNP-D at 37℃ and 42℃ at acidic (pH 5.0) conditions. (Mean±SD (n=5).

doi:10.6342/NTU201902917

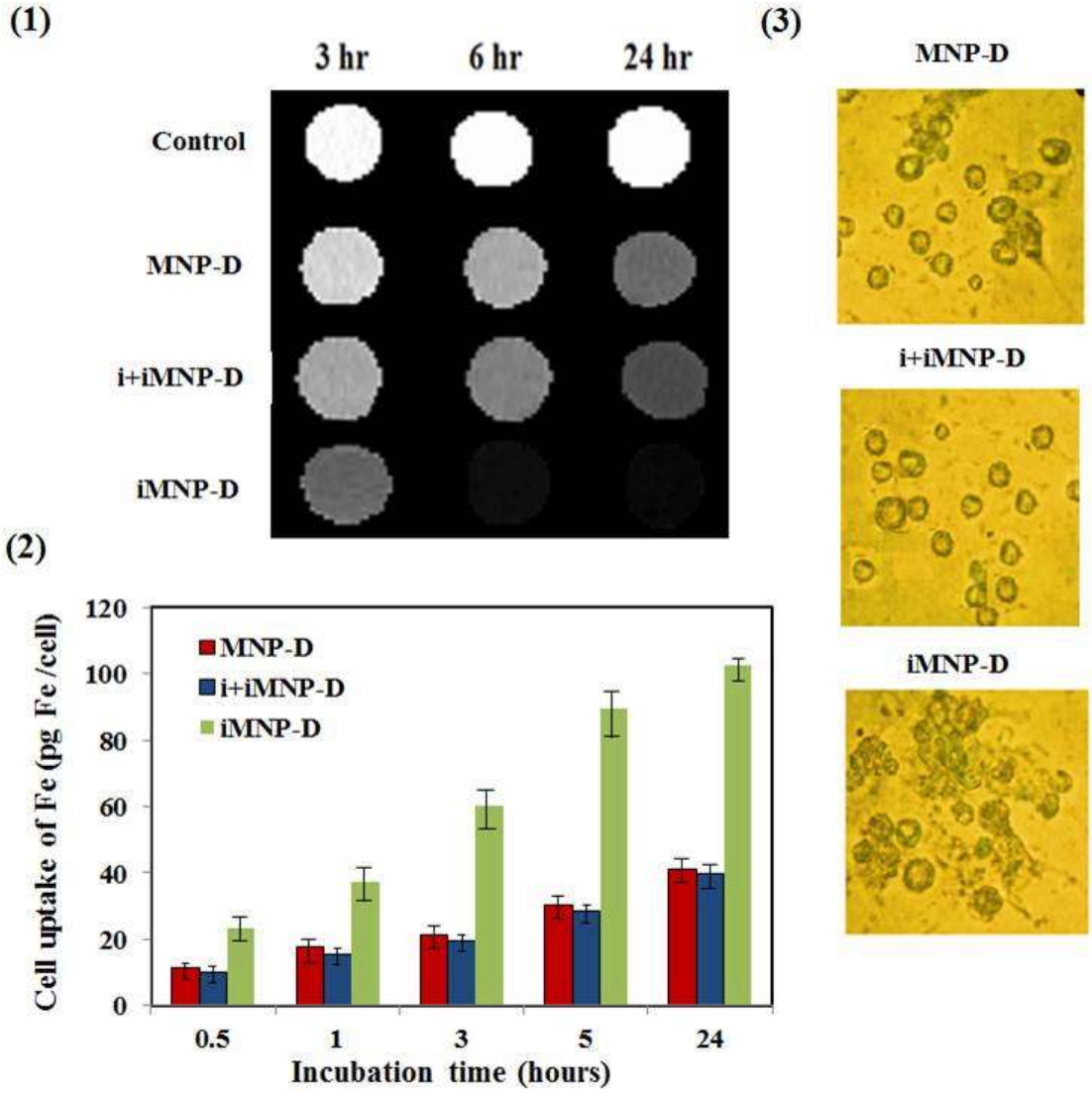

Figure 3-8. (1) T_2-weighted MR phantom images of HT-29 cells after incubation with MNP-D, iMNP-D, or i+iMNP-D for 3 hr, 6 hr, or 24 hr, and (2) The iron uptake in HT-29 cells treated with 100 μg Fe/mL of MNP-D, iMNP-D, or i+iMNP-D at different incubation times. (3) Prussian blue staining images of HT-29 cells after 24 h treatment with MNP-D, iMNP-D, or i+iMNP-D. (Mean±SD (n=5).

doi:10.6342/NTU201902917

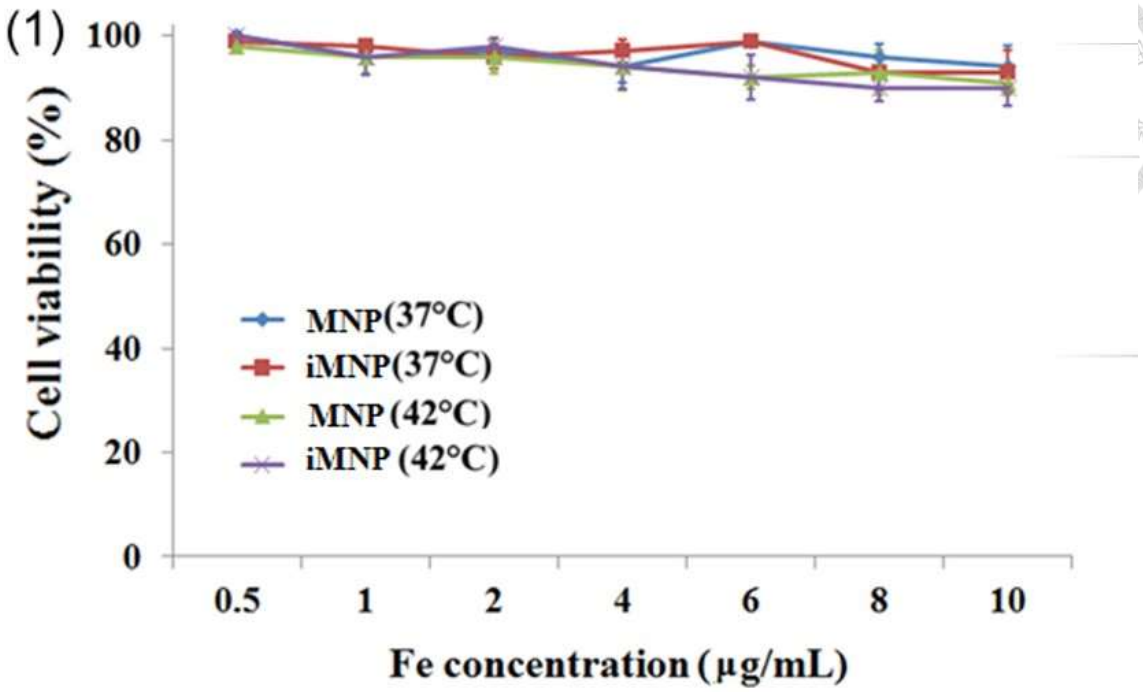

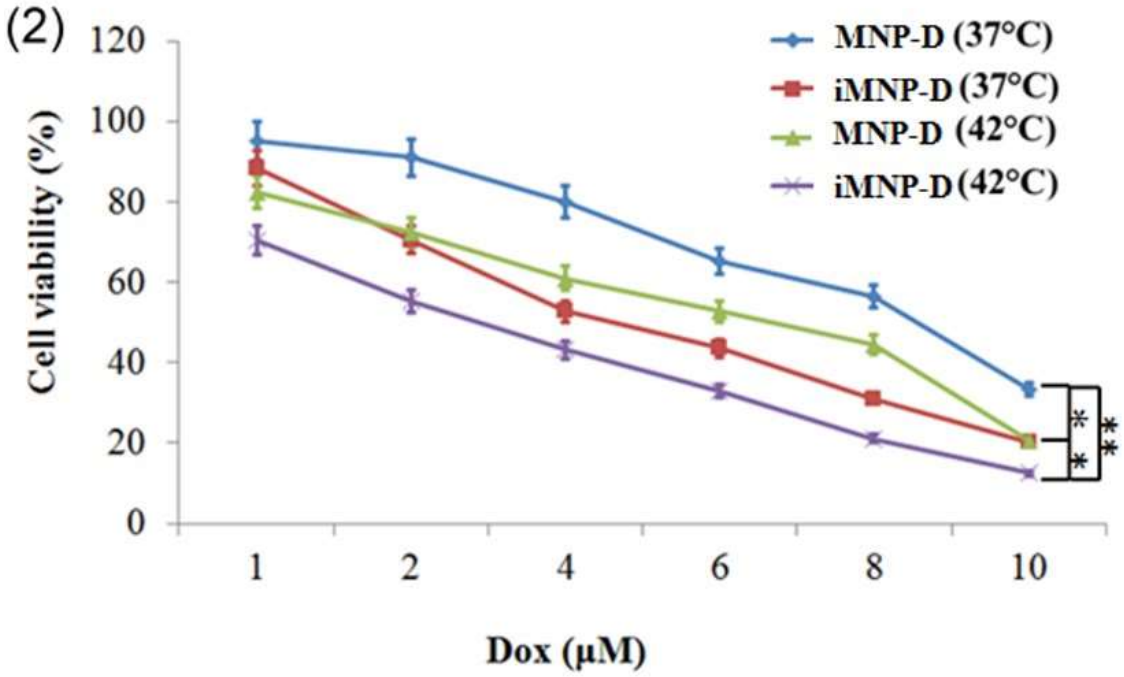

Figure 3-9. (1) Viability of HT-29 cells after incubation with MNP and iMNP at 37℃ or 42℃. (2) Viability of HT-29 cells after incubation with MNP-D and iMNP-D at 37℃ or 42℃. (Mean±SD (n=5), *: P＜0.05; **: P＜0.01).

doi:10.6342/NTU201902917

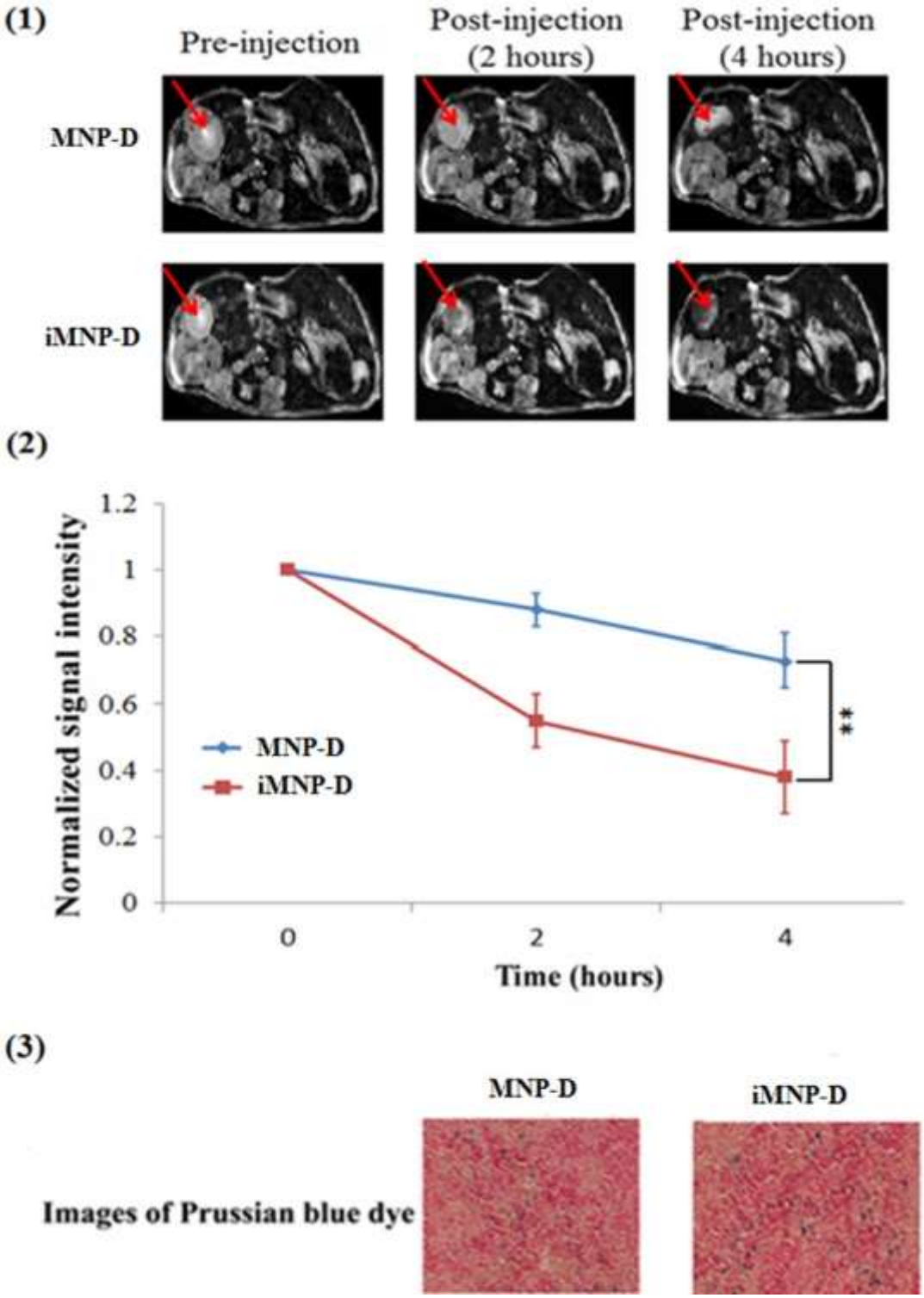

Figure 3-10. (1) T_2-weighted MR images before and after treatment with MNP-D or iMNP-D, and (2) MR signal intensity in mouse tumors. (Mean±SD (n=5) , *: $P < 0.05$; **: $P < 0.01$). (3) Microscope images of Prussian blue dye stained tumor tissues after treatment with MNP-D or iMNP-D.

doi:10.6342/NTU201902917

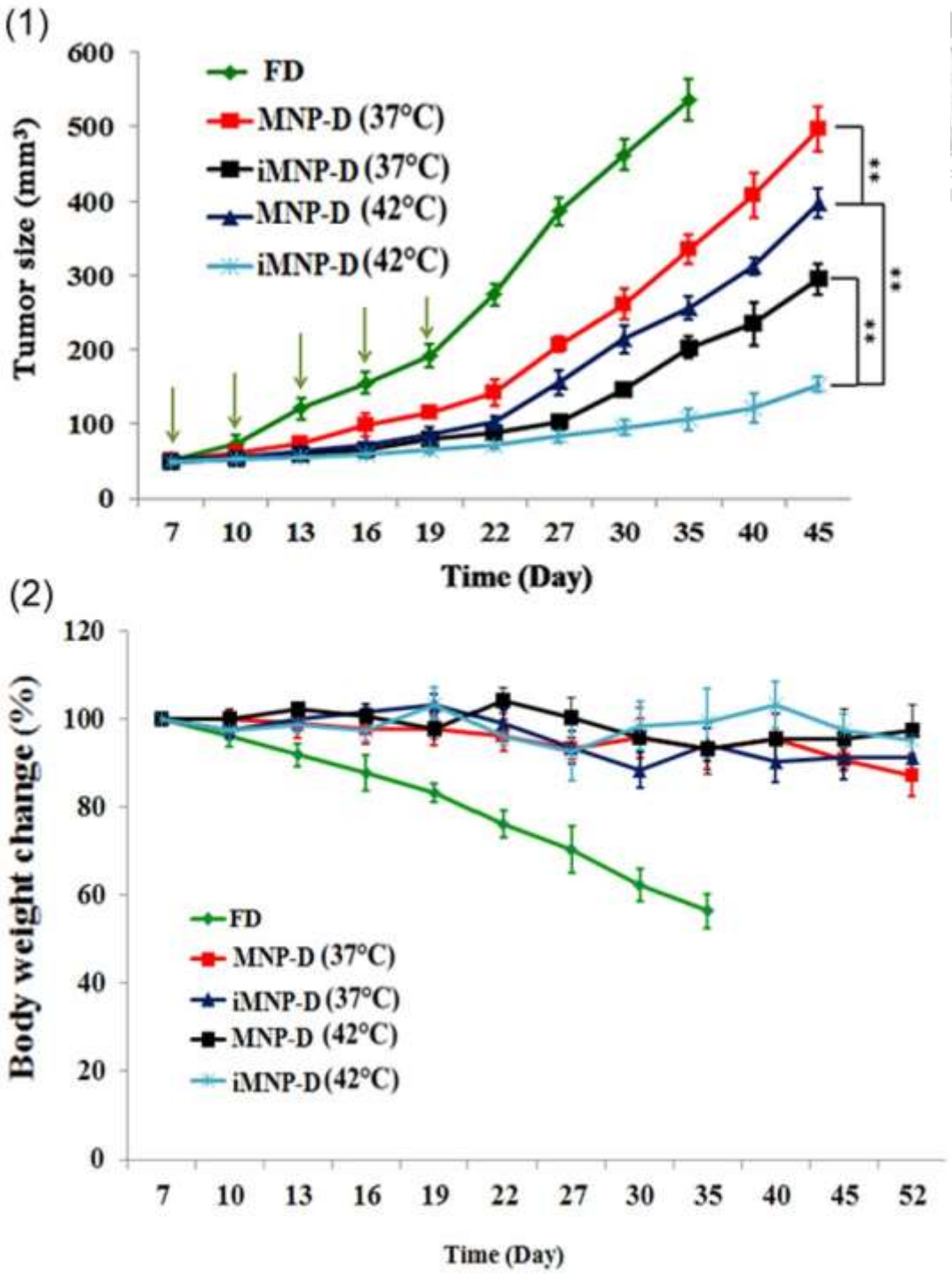

Figure 3-11. Tumor growth inhibition test of s.c. HT-29 xenografts in BALB/c nude mice. Mice were i.v. injected with MNP-D or iMNP-D at 37℃ or 42℃. The administration was carried out 5 times with a 3-day interval (green arrows: treatment days) (Mean±SD (n=10), *: $P < 0.05$; **: $P < 0.01$). (2) Body weight changes of the tumor-bearing mice. (Mean±SD (n=8).

doi:10.6342/NTU201902917

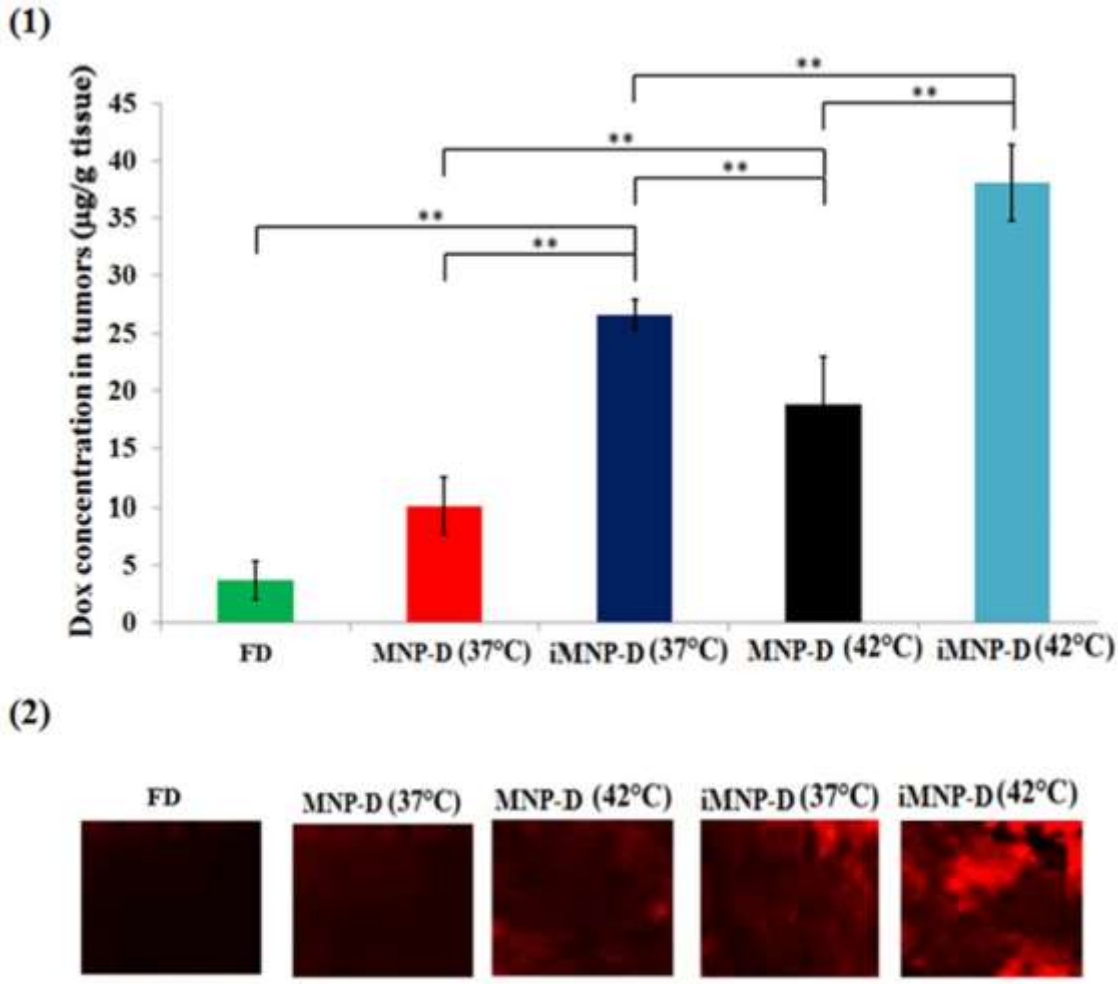

Figure 3-12. (1) Dox concentrations in tumor tissues for the tumor-bearing mice treated with FD, MNP-D (37℃), iMNP-D (37℃), MNP-D (42℃),and iMNP-D (42℃). (Mean±SD (n=4), *: P＜0.05; **: P＜0.01). (2) Confocal laser scanning microscopic images of tumor tissues at 4 h after the injection.

doi:10.6342/NTU201902917

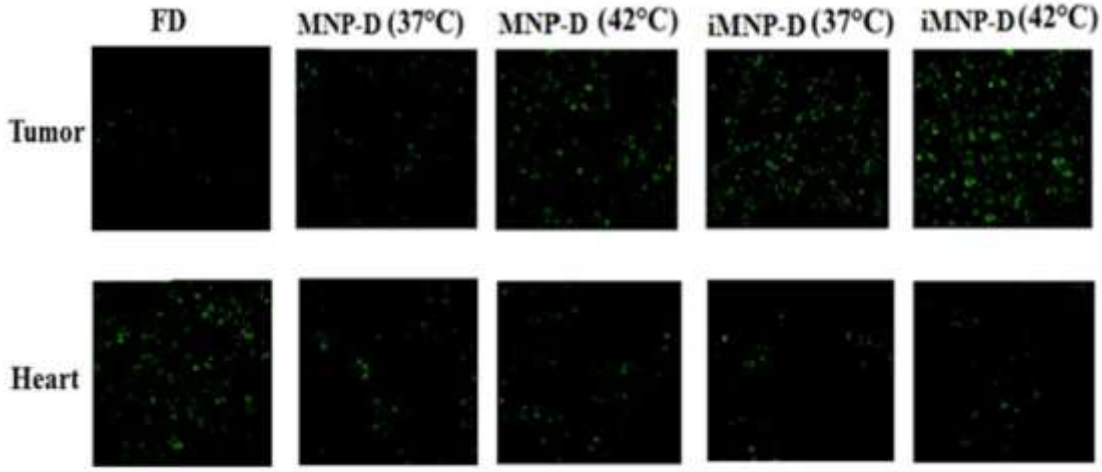

Figure 3-13. TUNEL analysis of tumor sections obtained from s.c. HT-29 xenografts in BALB/c nude mice. Mice were treated with FD, MNP-D or iMNP-D at 37℃ or 42℃ on day 45 after HT-29 cell implantation. The administration was carried out 5 times with a 3-day interval. Green: apoptosis cells marked by FITC.

doi:10.6342/NTU201902917

Table 3-1. Characterization of MNP-D and iMNP-D (n=3).

Groups	Particle size (nm)	Polydispersity	Zeta potential (mV)	Encapsulation Efficiency of Dox (%)	Encapsulation Efficiency of IO-CA (%)
iMNP-D	101.2 ± 3.5	0.15 ± 0.03	-14.23 ± 1.7	85.33 ± 2.7	20.16 ± 1.2
MNP-D	97.11 ± 2.7	0.09 ± 0.01	-20.52 ± 0.8	85.17 ± 1.2	21.58 ± 2.4

doi:10.6342/NTU201902917

Chapter 4. Summary and future work

In summary, COOH-PEG-triethoxysilane was synthesized, conjugated to the surface of SPIONs to form PEG-bound magnetic nanoparticles (SPIO-PEG), and then Dox was conjugated onto the SPIO-PEG surface to produce SPIO-PEG-D, a multifunctional magnetic nanoparticle. By applying a magnetic field, SPIO-PEG-D could be concentrated in the tumor region to increase the intratumoral concentration of Dox and reduce the drug toxicity for normal organs. In addition, the in vivo MRI study showed that there was a better signal contrast enhancement for SPIO-PEG obtained with applying a magnetic field. This multifunctional magnetic nanoparticle with high loading of drug, superparamagnetic property, and high magnetic relaxivities could become not only an effective delivery system for chemotherapy but also a great contrast agent for MR imaging. Magnetic enhancement delivery of SPIO-PEG-D was a promising targeting technique that could provide more effective cancer treatment and reduce potential side effects of drug.

Furthermore, we had prepared a temperature/pH-sensitive iMNP-D and utilized it as a MR-monitoring drug delivery system. The experimental results have demonstrated that iMNP-D has a great potential for providing an enhanced cellular uptake and drug controlled release with a short-time tumor heating and significantly improving drug accumulation in the treated tumors. The highly tumor-penetrating cancer cell-targeting and temperature/pH-sensitive properties of the iMNP-D contribute the efforts to establishing an effective tumor-selective and controlled release chemotherapy. iMNP-D can reduce the toxicity and side effects of Dox and improve tumor targeting delivery. Furthermore, the in-vivo MRI study showed a better contrast enhancement of signals for iMNP-D, indicating iMNP-D could not only be an effective carrier of chemotherapeutic

doi:10.6342/NTU201902917

agent but also be an excellent contrast agent for MR monitoring. Hence, iMNP-D might have a great potential for the application of MR monitoring and drug controlled release chemotherapy in the treatment of cancer.

The future work, we may use magnetic nanoparticles with externally applied magnet for superficial tumor, such as breast cancer, head and neck cancer, and for extremity tumor, to enhance local treatment effect and decrease systemic side effect. Additionally, we can also use magnetic nanoparticles and drainage tube or NG tube with magnetic segment to treatment endoluminal tumors, such as cholangiocarcinoma or esophageal cancer, not only for palliative drainage or feeding, but also aggressive treatment.(Fig 4-1)

Furthermore, we can use RFA instead of infrared to create local heat of tumors, make protein coagulation and tumor necrosis in the center of the tumors at lethal temperature, and trigger drug controlled release from temperature/pH-sensitive iMNP-D at margin of tumor at sublethal temperatures, thus achieve complete treatment of the tumor.(Fig 4-2) In addition, this multifunctional nanoparticle can carry target therapy or immunotherapy drug, small molecules, aptamers, or genes for other novel treatment.

doi:10.6342/NTU201902917

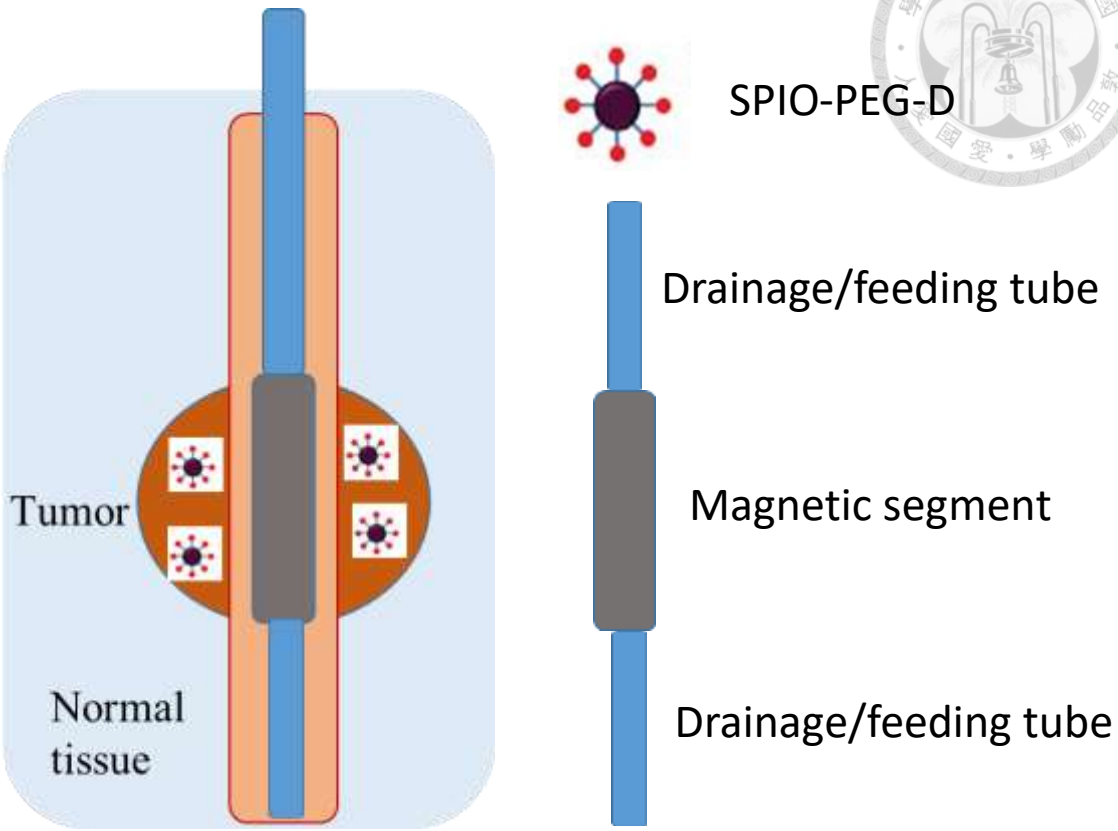

Fig 4-1. Through the esophageal cancer or cholangiocarcinoma, the NG tube or drainage tube with magnetic segment corresponding to the tumor location, can attract magnetic nanoparticles SPIO-PEG-D toward tumor, not only for feeding or drainage, but also for aggressive treatment of tumor.

doi:10.6342/NTU201902917

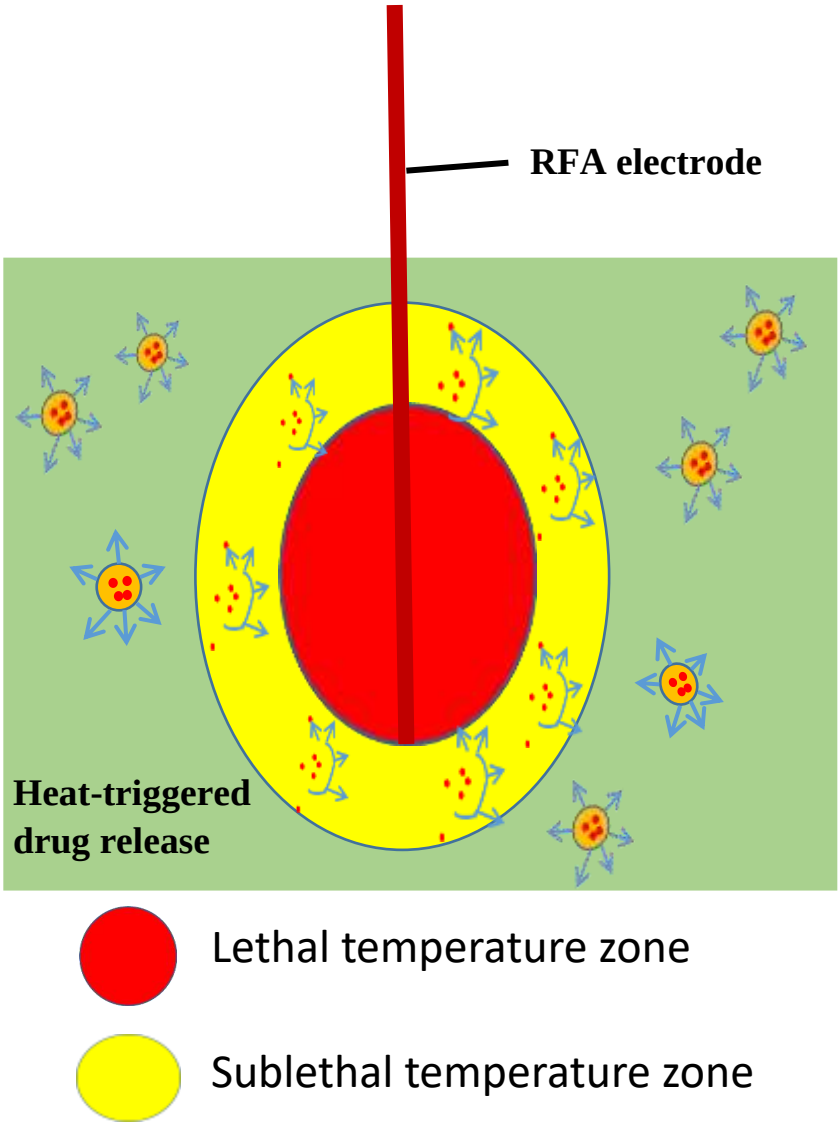

Fig 4-2. We can completely ablate the tumor by RFA alone at lethal temperature zone, but we should combine heat-triggered drug release in sublethal temperature zone to complete treat the tumor, because sublethal temperature is not high enough to kill the tumor.

doi:10.6342/NTU201902917

Acknowledgement

醫工所老師

林文澧 教授

謝銘鈞 教授

翁昭旼 教授

醫工所同學

陳永竹

江季峰

台大醫院

施庭芳主任

張允中主任

曾旭明教授

李伯皇教授

黃凱文教授

魏淑圓 放射師

國家衛生研究院

科技部

工研院 生醫所

謝文元 博士

義大醫院　牟聯瑞副執行長

doi:10.6342/NTU201902917

Reference

[1] Greish K. Enhanced permeability and retention of macromolecular drugs in solid tumors: a royal gate for targeted anticancer nanomedicines. J Drug Target. 2007;15:457–464.

[2] Greish K. Enhanced permeability and retention (EPR) effect for anticancer nanomedicine drug targeting. Methods Mol Biol. 2010;624:25–37.

[3] Wang X, Wang Y, Shin DM. Advances of cancer therapy by nanotechnology. Cancer Res Treat. 2009;41:1–11.

[4] Byrne JD, Betancourt T, Brannon-Peppas L. Active targeting schemes for nanoparticle systems in cancer therapeutics. Adv Drug Deliv Rev. 2008;60:1615–1626.

[5] Kreuter J. Nanoparticles - a historical perspective. Int J Pharm. 2007;331:1–10.

[6] Maeda H, Matsumura Y. Tumoritropic and lymphotropic principles of macromolecular drugs. Crit Rev Ther Drug Carrier Syst. 1989;6:193–210.

[7] Matsumura Y, Maeda H. A new concept for macromolecular therapeutics in cancer chemotherapy: mechanism of tumoritropic accumulation of proteins and the antitumor agent smancs. Cancer Res. 1986;46:6387–6392.

[8] Stohrer M, Boucher Y, Jain RK. Oncotic pressure in solid tumors is elevated. Cancer Res. 2000;60:4251–4255.

[9] Kirpotin DB, Drummond DC, Park JW. Antibody targeting of long-circulating lipidic nanoparticles does not increase tumor localization but does increase internalization in animal models. Cancer Res. 2006;66:6732–6740.

[10] Bartlett DW, Su H, Davis ME. Impact of tumor-specific targeting on the biodistribution and efficacy of siRNA nanoparticles measured by multimodality in

doi:10.6342/NTU201902917

vivo imaging. Proc Natl Acad Sci U S A. 2007;104:15549–15554.

[11] Farokhzad OC, Cheng J, Langer R. Targeted nanoparticle-aptamer bioconjugates for cancer chemotherapy in vivo. Proc Natl Acad Sci U S A. 2006;103:6315–6320.

[12] Alexiou C, Arnold W, Lübbe AS. Locoregional cancer treatment with magnetic drug targeting. Cancer Res. 2000;60:6641–6648.

[13] Reiss G, Hutten A. Magnetic nanoparticles are useful for a wide range of applications from data storage to medicinal imaging. The large-scale preparation of FeCo nanoparticles boosts this potential. Nat Mater. 2005;4:725–726.

[14] Qiao R, Jia Q, Gao M. Receptor-mediated delivery of magnetic nanoparticles across the blood–brain barrier. ACS Nano. 2012;6:3304–3310.

[15] Dilnawaz F, Singh A, Sahoo SK. Dual drug loaded superparamagnetic iron oxide nanoparticles for targeted cancer therapy. Biomaterials. 2010;31:3694–3706.

[16] Polyak B, Friedman G. Magnetic targeting for site-specific drug delivery: applications and clinical potential. Expert Opinion on Drug Delivery. 2009; 6 (1): 53–70.

[17] Arruebo M, Fernandez-Pacheco R, Santamaria J. Magnetic nanoparticles for drug delivery. Nanotoday 2007;2(3):22-32.

[18] Johannsen M, Gneveckow U, Jordan A, et al. Clinical hyperthermia of prostate cancer using magnetic nanoparticles: presentation of a new interstitial technique. Int J Hyperthermia 2005;21(7):637-47.

[19] Johannsen M, Thiesen B, Loening SA, et al. Magnetic fluid hyperthermia (MFH) reduces prostate cancer growth in the orthotopic Dunning R3327 rat model. Prostate 2005;64(3):283-92.

[20] Alexiou C, Jurgons R, Odenbach S, et al. Delivery of superparamagnetic nanoparticles for local chemotherapy after intraarterial infusion and magnetic drug

doi:10.6342/NTU201902917

targeting. Anticancer Res 2007;27(4A):2019-22.

[21] Jurgons R, Seliger C, Alexiou C, et al. Drug loaded magnetic nanoparticles for cancer therapy. J Phys Condens Matter 2006;18(38):S2893-S902.

[22] Ito A, Ino K, Honda H, et al. Novel methodology for fabrication of tissue-engineered tubular constructs using magnetite nanoparticles and magnetic force. Tissue Eng 2005;11(9-10):1553-61.

[23] Ito A, Takizawa Y, Kobayashi T, et al. Tissue engineering using magnetite nanoparticles and magnetic force: heterotypic layers of cocultured hepatocytes and endothelial cells. Tissue Eng 2004;10(5-6):833-40.

[24] Shimizu K, Ito A, Honda H, et al. Bone tissue engineering with human mesenchymal stem cell sheets constructed using magnetite nanoparticles and magnetic force. J Biomed Mater Res B Appl Biomater 2007;82(2):471-80.

[25] Kumar CS. Nanomaterials for medical diagnosis and therapy. Wiley-VCH. 2007.

[26] Na K, Lee ES and Bae YH. Self-organized nanogels responding to tumor extracellular pH: pH-dependent drug release and in vitro cytotoxicity against MCF-7 cells. Bioconjug Chem 2007; 18: 1568–1574.

[27] Leroux J, Roux E, Drummond DC. (2001) N-Isopropylacrylamide copolymers for the preparation of pH-sensitive liposomes and polymeric micelles. J. Controlled Release 72, 71−84.

[28] Cammas S, Suzuki K, Okano T. (1997) Thermo-responsive polymer nanoparticles with a core-shell micelle structure as site-specific drug carriers. J. Controlled Release 48, 157−164.

[29] Na K, Lee KH, Bae YH. (2006) Biodegradable temperature-sensitive nanoparticles from poly(ethylene glycol)(PEG)/poly(L-lactic acid)(PLLA) alternating multiblock copolymer for anticancer drug delivery. Eur. J. Pharm. Sci.

doi:10.6342/NTU201902917

27, 115−122.

[30] Chung JE, Yokoyama M, and Okano T. (2000) Inner core segment design for delivery control of thermo-responsive polymeric micelles. J. Controlled Release 65, 93−103.

[31] Bae Y, Nishiyama N, Kataoka K. (2005) Preparation and biological characterization of polymeric micelle drug carriers with intracellular pH-triggered drug release property: tumor permeability, controlled subcellular drug distribution, and enhanced in vivo antitumor efficacy. Bioconjugate Chem. 16, 122−130.

[32] (a) Bulmus V, Woodward M, Hoffman A. A new pH-responsive and glutathione-reactive, endosomal membrane-disruptive polymeric carrier for intracellular delivery of biomolecular drugs. Journal of Controlled Release. 2003;93:105–120. (b) You YZ, Zhou QH, Oupický D. Dually responsive multiblock copolymers via RAFT polymerization: Synthesis of temperature- and redox-responsive copolymers of PNIPAM and PDMAEMA. Macromolecules2007;40:8617-8624.

[33] V.P. Torchilin.Multifunctional nanocarriers.Adv Drug Deliv Rev, 58 (2006), pp. 1532-1555.

[34] J.M. Chan, L. Zhang, OC. Farokhzad, et al.PLGA-lecithin-PEG core-shell nanoparticles for controlled drug delivery .Biomaterials, 30 (2009), pp. 1627-1634.

[35] J. Kim, J.E. Lee, T. Hyeon, et al.Designed fabrication of a multifunctional polymer nanomedical platform for simultaneous cancer-targeted imaging and magnetically guided drug delivery.Adv Mater, 20 (2008), pp. 478-483.

[36] D. Peer, J.M. Karp, R. Langer.Nanocarriers as an emerging platform for cancer therapy.Nat Nanotechnol,2 (2007), pp. 751-760.

[37] L. Zhang, J.M. Chan, O.C Farokhzad, et al.Self-assembled lipid–polymer hybrid

doi:10.6342/NTU201902917

nanoparticles: a robust drug delivery platform.ACS Nano, 2 (2008), pp. 1696-1702

[38] Montet X, Funovics M, Josephson L. Multivalent effects of RGD peptides obtained by nanoparticle display. J Med Chem. 2006;49:6087–93.

[39] Gao J, Gu H, Xu B. Multifunctional magnetic nanoparticles: design, synthesis, and biomedical applications. Acc Chem Res. 2009;42:1097–107.

[40] Pan D, Caruthers SD, Lanza GM. et al. Ligand-directed nanobialys as theranostic agent for drug delivery and manganese-based magnetic resonance imaging of vascular targets. J Am Chem Soc. 2008;130:9186–7.

[41] Bae KH, Lee K, Park TG. Surface functionalized hollow manganese oxide nanoparticles for cancer targeted siRNA delivery and magnetic resonance imaging. Biomaterials. 2011;32:176–84.

[42] Xiong D, He Z, Shi L, et al. Temperature-responsive multilayered micelles formed from the complexation of PNIPAM-b-P4VP block-copolymer and PS-b-PAA core–shell micelles. Polymer. 2008;49:2548–2552.

[43] Kim SY, Shin G, Lee YM. Amphiphilic diblock copolymeric nanospheres composed of methoxy poly(ethylene glycol) and glycolide: properties, cytotoxicity and drug release behavior. Biomaterials. 1999;20:1033–1042.

[44] Li JB, Shi L, Dong H, et al. Reverse micelles of star-block copolymer as nanoreactors for preparation of gold nanoparticles. Polymer. 2006;47:8480–8487.

[45] Kataoka K, Matsumoto T, Kwon GS, et al. Doxorubicin-loaded poly(ethylene glycol)–poly(β-benzyl-L-aspartate) copolymer micelles: their pharmaceutical characteristics and biological significance. J Control Release. 2000;64:143–153.

[46] Liu D, Zhong C. Multicompartment micelles formed from star-dendritic triblock copolymers in selective solvents: a dissipative particle dynamics study. Polymer. 2008;49:1407–1413.

doi:10.6342/NTU201902917

[47] Nasongkla N, Bey E, Gao J, et al. Multifunctional, polymeric micelles as cancer-targeted, MRI-ultrasensitive drug delivery systems. Nano Lett. 2006;6:2427–2430.

[48] Yang J, Lee CH, Haam S, et al. Multifunctional magneto-polymeric nanohybrids for targeted detection and synergistic therapeutic effects on breast cancer. Angew Chem Int Ed. 2007;46:8836–8839.

[49] Liong M, Lu J, I.Zink J, et al. Multifunctional inorganic nanoparticles for imaging, targeting, and drug delivery. ACS Nano. 2008;2:889–896.

[50] Yang X, Grailer JJ, Gong S, et al. Multifunctional SPIO/DOX-loaded wormlike polymer vesicles for cancer therapy and MR imaging. Biomaterials. 2010;31:9065–9073.

[51] Zhang HZ, Gao FP, Zhang QQ, et al. Pullulan acetate nanoparticles prepared by solvent diffusion method for epirubicin chemotherapy. Colloids Surf B Biointerfaces. 2009;71:19–26.

[52] Liu Z, Jiao Y, Zhang Z, et al. Polysaccharides-based nanoparticles as drug delivery systems. Adv Drug Deliv Rev. 2008;60:1650–1662.

[53] Lubbe AS, Alexiou C, Bergemann C. Clinical applications of magnetic drug targeting. J Surg Res. 2001;95:200–206.

[54] Häfeli UO. Magnetically modulated therapeutic systems. Int J Pharm. 2004;277:19–24.

[55] Lübbe AS, Bergemann C, Huhn D, et al. Preclinical experiences with magnetic drug targeting: tolerance and efficacy. Cancer Res. 1996;56:4694–4701.

[56] Wang X, Wei F, Wang J, et al. Cancer stem cell labeling using poly(L-lysine)-modified iron oxide nanoparticles. Biomaterials. 2012;33(14):3719–3732.

doi:10.6342/NTU201902917

[57] Laurent S, Dutz S, Häfeli UO, Mahmoudi M. Magnetic fluid hyperthermia: focus on superparamagnetic iron oxide nanoparticles. Adv Colloid Interface Sci. 2011;166(1–2):8–23.

[58] Alexiou C, Jurgons R, Parak F, et al. Magnetic drug targeting: biodistribution of the magnetic carrier and the chemotherapeutic agent mitoxantrone after locoregional cancer treatment. J Drug Target. 2003;11:139–149.

[59] Asmatulu R, Zalich MA, Riffle J.S, et al. Synthesis, characterization and targeting of biodegradable magnetic nanocomposite particles by external magnetic fields. J Magn Magn Mater. 2005;292:108–119.

[60] Ma YH, Hsu YW, Wu Tony, et al. Intra-arterial application of magnetic nanoparticles for targeted thrombolytic therapy: a rat embolic model. J Magn Magn Mater. 2007;311:34–36.

[61] Liu HL, Hua MY, Wei KC., et al. Magnetic resonance monitoring of focused ultrasound/magnetic nanoparticle targeting delivery of therapeutic agents to the brain. Proc Natl Acad Sci U S A. 2010;107(34):15205–15210.

[62] Lübbe AS, Bergemann C, Huhn D, et al. Clinical experiences with magnetic drug targeting: a phase I study with 4´-epidoxorubicin in 14 patients with advanced solid tumors. Cancer Res. 1996;56:4686–4693.

[63] Owens DE, 3rd, Peppas NA. Opsonization, biodistribution, and pharmacokinetics of polymeric nanoparticles. Int J Pharm. 2006;307:93–102.

[64] Lin JJ, Chen JS, Wang LF, et al. Folic acid-Pluronic F127 magnetic nanoparticle clusters for combined targeting, diagnosis, and therapy applications. Biomaterials. 2009;30:5114–5124.

[65] Babic M, Horák D, Syková E, et al. Poly(N, N-dimethylacrylamide)-coated maghemite nanoparticles for stem cell labeling. Bioconjug Chem.

doi:10.6342/NTU201902917

2009;20:283–294.

[66] Chen AL, Ni HC, hen JS, et al. Biodegradable amphiphilic copolymers based on poly(epsilon-caprolactone)-graft chondroitin sulfate as drug carriers. Biomacromolecules. 2008;9:2447–2457.

[67] Liu X, Hu Q, Zhang B, et al. Magnetic chitosan nanocomposites: a useful recyclable tool for heavy metal ion removal. Langmuir. 2009;25:3–8.

[68] Bumb A, Brechbiel M, Dobson PJ, et al. Synthesis and characterization of ultra-small superparamagnetic iron oxide nanoparticles thinly coated with silica. Nanotechnology. 2008;19:335601.

[69] Chertok B, Moffat BA, Yang VC, et al. Iron oxide nanoparticles as a drug delivery vehicle for MRI monitored magnetic targeting of brain tumors. Biomaterials. 2008;29:487–496.

[70] Liu CG, Desai KG, Chen XG, et al. Linolenic acid-modified chitosan for formation of self-assembled nanoparticles. J Agric Food Chem. 2005;53:437–441.

[71] Imai Y, Murakami T, Nakamura H, et al. Superparamagnetic iron oxide-enhanced magnetic resonance images of hepatocellular carcinoma: correlation with histological grading. Hepatology. 2000;32:205–212.

[72] Ward J, Guthrie JA, obinson PJ, et al. Hepatocellular carcinoma in the cirrhotic liver: double-contrast MR imaging for diagnosis. Radiology. 2000;216:154–162.

[73] Hori M, Murakami T, Nakamura H, et al. Detection of hypervascular hepatocellular carcinoma: comparison of SPIO-enhanced MRI with dynamic helical CT. J Comput Assist Tomogr. 2002;26:701–710.

[74] Lee PW, Hsu SH, Sung HW, et al. The characteristics, biodistribution, magnetic resonance imaging and biodegradability of superparamagnetic core–shell nanoparticles. Biomaterials. 2010;31:1316–1324.

doi:10.6342/NTU201902917

[75] Zhang B, Li Q, Shi D, et al. Ultrasound-triggered BSA/SPION hybrid nanoclusters for liver-specific magnetic resonance imaging. ACS Appl Mater Interfaces. 2012;4:6479–6486.

[76] Zhang WQ, Shi LQ, Wu K, et al. Thermoresponsive micellization of poly(ethylene glycol)-b-poly(Nisopropylacrylamide) in water. Macromolecules 2005; 38: 5743–5747.

[77] Motokawa R, Morishita K, Annaka M, et al. Thermosensitive diblock copolymer of poly(N-isopropylacrylamide) and poly(ethylene glycol) in water: polymer preparation and solution behavior. Macromolecules 2005; 38: 5748–5760.

[78] Qin S, Geng Y, Yang S, et al. Temperature-controlled assembly and release from polymer vesicles of poly(ethylene oxide)-block-poly(N-isopropylacrylamide). Adv Mater 2006; 18: 2905-2909.

[79] Hoogenboom R, Thij HML, Schubert U.S, et al. Tuning solution polymer properties by binary water-ethanol solvent mixtures. Soft Matter 2008; 4: 103–107.

[80] Ahmed F and Discher DE. Self-porating polymersomes of PEG–PLA and PEG–PCL: hydrolysis-triggered controlled release vesicles. J Control Release 2004; 96: 37–53.

[81] Lomas H, Massignani M, Battaglia G, et al. Non-cytotoxic polymer vesicles for rapid and efficient intracellular delivery. Faraday Discuss 2008; 139: 143–159.

[82] Hu J, Qian Y, Liu S, et al. Drug-loaded and superparamagnetic iron oxide nanoparticle surface embedded amphiphilic block copolymer micelles for integrated chemotherapeutic drug delivery and MR imaging. Langmuir 2011; 28: 2073–2082.

[83] Sanson C, Diou O, Lecommandoux S, et al. Doxorubicin loaded magnetic polymersomes: theranostic nanocarriers for MR imaging and magneto-chemotherapy. ACS Nano 2011; 5: 1122–1140.

doi:10.6342/NTU201902917

[84] Jiang JQ, Tong X, Zhao Y, et al. Toward photocontrolled release using light-dissociable block copolymer micelles. Macromolecules 2006; 39: 4633–4640.

[85] Oerlemans C, Bult W, Hennink WE, et al. Polymeric micelles in anticancer therapy: targeting, Imaging and Triggered Release. Pharm Res 2010; 27: 2569–2589.

[86] Chen J, Qiu X, Xing M.Q, et al. pH and reduction dual-sensitive copolymeric micelles for intracellular Doxorubicin delivery. Biomacromolecules 2011; 12: 3601–3611.

[87] Zhang J, Wu L, Zhong Z, et al. pH and reduction dual-bioresponsive polymersomes for efficient intracellular protein delivery. Langmuir 2011; 28: 2056–2065.

[88] Wei C, Guo J, Wang C. Dual stimuli-responsive polymeric micelles exhibiting "AND" logic gate for controlled release of Adriamycin. Macromol Rapid Commun 2011; 32: 451–455.

[89] Xiong Z, Peng B, Hu Y, et al. Dual-stimuli responsive behaviors of diblock polyampholyte PDMAEMA-b-PAA in aqueous solution. J Colloid Interface Sci 2011; 356: 557–565.

[90] Han D, Tong X, Zhao Y. Block copolymer micelles with a dual-stimuli-responsive core for fast or slow degradation. Langmuir 2012; 28: 2327–2331.

[91] Klaikherd A, Nagamani C, Thayumanavan S. Multi-stimuli sensitive amphiphilic block copolymer assemblies. J Am Chem Soc 2009; 131: 4830–4838.

[92] Morimoto N, Qiu XP, Winnik FM, et al. Dual stimuli-responsive nanogels by self-assembly of polysaccharides lightly grafted with thiol-terminated poly(Nisopropylacrylamide) chains. Macromolecules 2008; 41: 5985–5987.

[93] De Las Heras Alarcon C, Pennadam S and Alexander C. Stimuli responsive

doi:10.6342/NTU201902917

polymers for biomedical applications. Chem Soc Rev 2005; 34: 276–85.

[94] Xiong W, Wang W, Yang X, et al. Dual temperature/pH-sensitive drug delivery of poly(N- isopropylacrylamide-co-acrylic acid) nanogels conjugated with Doxorubicin for potential application in tumor hyperthermia therapy. Colloids and Surfaces B: Biointerfaces 2011; 84: 447-453.

[95] Yu MK, Kim D, Jon S, et al. Image-guided prostate cancer therapy using aptamer-functionalized thermally cross-linked superparamagnetic iron oxide nanoparticles. Small 2011; 7: 2241–2249.

[96] Lim EK, Huh YM, Haam S, et al. pH-Triggered drug-releasing magnetic nanoparticles for cancer therapy guided by molecular imaging by MRI. Adv Mater 2011; 23: 2436–2342.

[97] Yu MK, Jeong YY, Jon S, et al. Drug-loaded superparamagnetic iron oxide nanoparticles for combined cancer imaging and therapy in vivo. Angew Chem Int Ed Engl 2008; 47: 5362–5365.

[98] Srinivas M, Aarntzen EH, Figdor CG, et al. Imaging of cellular therapies. Adv Drug Deliv Rev 2010; 62: 1080–1093.

[99] Tacar O, Sriamornsak P, Dass CR. Doxorubicin: an update on anticancer molecular action, toxicity and novel drug delivery systems. Journal of Pharmacy and Pharmacology 2013; 65: 157–170.

[100] Pedchenko V, Zent R, Hudson BG. αvβ3 and αvβ5 integrins bind both the proximal RGD site and non-RGD motifs within noncollagenous (NC1) domain of the α3 chain of type IV collagen: implication for the mechanism of endothelial cell adhesion. J Biol Chem 2004; 279: 2772–2780.

[101] Zhang C, Jugold M, Kiessling F, et al. Specific targeting of tumor angiogenesis by RGD-conjugated ultrasmall superparamagnetic iron oxide particles using a

doi:10.6342/NTU201902917

clinical 1.5-T magnetic resonance scanner. Cancer Res 2007;67: 1555-1562.

[102] Murphy EA, Majeti BK, Cheresh DA, et al. Nanoparticle-mediated drug delivery to tumor vasculature suppresses metastasis. Proc Natl Acad Sci USA 2008; 105: 9343-9348.

[103] Tsai MH, Peng CL, Shieh MJ, et al. Photothermal, Targeting, Theranostic Near-Infrared Nanoagent with SN38 against Colorectal Cancer for Chemothermal Therapy. Mol Pharm. 2017 Aug 7;14(8):2766-2780.

[104] Sugahara KN, Teesalu T, Ruoslahti E, et al. Tissue-penetrating delivery of compounds and nanoparticles into tumors. Cancer Cell 2009; 16: 510-520.

[105] Stevens KR, Miller JS, Bhatia SN, et al. Degradable hydrogels derived from PEG-diacrylamide for hepatic tissue engineering. J Biomed Mater Res A 2005; 103: 3331–3338.

[106] Petcharoen K, Sirivat A. Synthesis and characterization of magnetite nanoparticles via the chemical co-precipitation method. Materials Science and Engineering: B 2012; 177: 421-427.

[107] Koning GA, Eggermont AM, Lindner LH, et al. Hyperthermia and thermosensitive liposomes for improved delivery of chemotherapeutic drugs to solid tumors. Pharm Res 2010; 27: 1750–1754.

[108] Chen YC, Min CN, Hsieh WY, et al. In vitro evaluation of the L-peptide modified magnetic lipid nanoparticles as targeted magnetic resonance imaging contrast agent for the nasopharyngeal cancer. Journal of Biomaterials Applications 2012; 28: 580–594.

[109] Tian Y, Bromberg L, Tam KC, et al. Complexation and release of Doxorubicin from its complexes with pluronic P85-b-poly (acrylic acid) block copolymers. Journal of Controlled Release 2007; 121: 137-145.

doi:10.6342/NTU201902917

[110] Chiang WH, Ho VT, Chern CS, et al. Dual stimuli-responsive polymeric hollow nanogels designed as carriers for intracellular triggered drug release. Langmuir 2012; 28: 15056-15064.

[111] Nie X, Zhang J, Wu Yan, et al. Targeting peptide iRGD-conjugated amphiphilic chitosan-co-PLA/DPPE drug delivery system for enhanced tumor therapy. J Mater Chem B 2014; 2: 3232-3242.

[112] Allen TM. Ligand-Targeted Therapeutics in Anticancer Therapy. Nat Rev Cancer 2002; 2: 750–763

doi:10.6342/NTU201902917